UNIVERSITY OF OKLAHOMA

GRADUATE COLLEGE

SEISMIC WAVE CHARACTERISTICS IN ANISOTROPIC ATTENUATING

MEDIA

A DISSERTATION

SUBMITTED TO THE GRADUATE FACULTY

in partial fulfillment of the requirements for the

degree of

Doctor of Philosophy

By

SATISH SINHA

Norman, Oklahoma

2006

UMI Number: 3242285

UMI®

SEISMIC WAVE CHARACTERISTICS IN ANISOTROPIC ATTENUATING
MEDIA

A DISSERTATION APPROVED FOR THE
SCHOOL GEOLOGY AND GEOPHYSICS

By

_____
Dr. Evgeni Chesnokov, Chair

_____
Dr. Raymon Brown

_____
Dr. James Forgotson
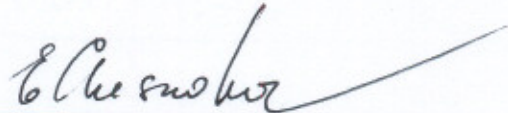

_____
Dr. Jean-Claude Roegiers

_____
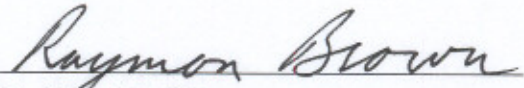Dr. Partha Routh

_____
Dr. Roger Young

SEISMIC WAVE CHARACTERISTICS IN ANISOTROPIC ATTENUATING MEDIA

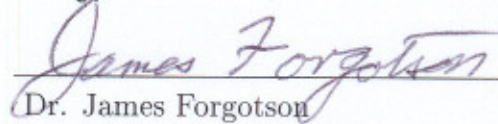## A DISSERTATION APPROVED FOR THE
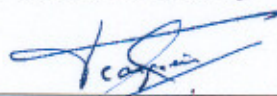## SCHOOL GEOLOGY AND GEOPHYSICS
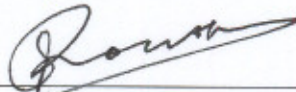
By

_____

Dr. Evgeni Chesnokov, Chair

_____

Dr. Raymon Brown

_____

Dr. James Forgotson

_____

Dr. Jean-Claude Roegiers

_____

Dr. Partha Routh

_____
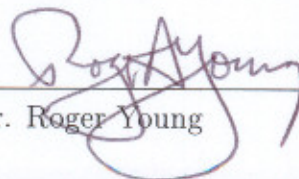
Dr. Roger Young

Acknowledgements

I am thankful to Prof. Evgeni Chesnokov, my research advisor and committee chair, for his guidance, advice and encouragement throughout this research work. His scientific curiosity and insightful comments were essential for a more complete solution to the problem. I am also grateful to him for providing me a great working environment and all facilities needed to carry out this research.

I wish to thank Dr. Sergey Abaseev, who has been instrumental in developing my concepts on seismic wave propagation. Thank you for your time and patience in helping me to understand key mathematical and physical concepts. I am also grateful to Dr. Irina Bayuk who provided me theoretical shale models for my research.

I am grateful to Dr. Ray Brown for being an active member of my advisory committee. His careful review and constructive criticism helped to improve parts of this document.

Thanks also to Dr. Roger Young, a member of the committee, for his constructive criticism on seismic modeling. Thanks to Dr. James Forgotson and Dr. Jean-Claude Roegiers for their time, suggestions, and for being a part of the committee. I would like to thank Dr. Partha Routh for his expert suggestions on parts of this research, and for a being part of the committee.

I am grateful to the Institute for Theoretical Geophysics and Devon Energy for supporting my research. I am also grateful to the School of Geology and Geophysics

iv

Contents

List Of Tables

List Of Figures

xiii

Abstract

A synthetic seismogram is a tool to investigate seismic wave characteristics in aniso-
tropic attenuating media. A numerical technique for the computation of synthetic
seismograms in a homogeneous, as well as in a multilayered anisotropic medium was
developed. Full waveform theory is used to compute the synthetic seismograms. The
medium can be elastic or viscoelastic. In the latter case, attenuation is introduced by
giving materials complex elastic constants. To ensure that there are no false arrivals
in the synthetic seismogram, it is important to carefully control the integration kernel
singularity points, especially those due to repeated roots of the associated Green-
Christoffel equation. A novel approach is developed to safely track the continuity of
the integration kernel and, hence, the polarization vectors in critical and supercritical
zones.

The reflectivity approach is followed to consider wave propagation in a multilay-
ered medium. A simple and concise implementation of this method is developed.
This approach also enables one to investigate frequency dependent reflection co-
efficients varying with incidence angle and azimuth. The modeling of reflection
coefficients in fractured media suggests that amplitude versus offset and azimuth
(AVOAz) can be helpful in detecting fractured reservoirs.

In a new development, the effect of attenuation on P- and S-wave radiation
patterns in viscoelastic anisotropic media is investigated. The understanding of

radiation patterns in homogeneous media is applied to interpret various wave types in attenuating multilayered media. Both the amplitude and the frequency content of the synthetic seismograms are affected by attenuation properties of the media. The spectral decomposition technique is found to be useful in our understanding of the attenuation effects.

Seismic anisotropy in shales is a complex phenomenon. A number of theoretical shale models are investigated to study the effects of clay orientation, aspect ratio of cracks, porosity and fluid types on the synthetic seismograms.

Chapter 1

Introduction

The focus of this research is to develop a numerical technique for full waveform synthetic seismograms in order to investigate the effects of attenuation on various wave types generated by different point sources in homogeneous and multilayered anisotropic media. There are three distinct achievements resulting from this research.

1. A novel technique is devised to safely track the longitudinal and shear waves polarizations in a general anisotropic medium.

2. Full waveform synthetic seismogram software for vertically transverse isotropic media is developed to include attenuation in a multilayered anisotropic media.

3. Spectral decomposition technique based on continuous wavelet transform (Sinha et al., 2005) is applied to investigate frequency dependent radiation of sources via anisotropic attenuating media.

These achievements can be applied to understand important aspects of the structure of the earth. Whether it is the core mantle boundary, or the continental crust,

or the oceanic crust or hydrocarbon or non-hydrocarbon reservoirs, the realistic earth is anisotropic and attenuating. From the hydrocarbon exploration point of view, let us consider one example of unconventional shaly reservoirs where shales are hydraulically fractured to produce hydrocarbon. Shales are anisotropic and fractures induced by injecting fluids in the shaly reservoirs make them viscoelastic or attenuating media. This dissertation approaches the problem by forward modeling of fractured, anisotropic and attenuating reservoirs.

Literature Reviews

A large number of published papers are devoted either to elastic anisotropic media or to viscoelastic isotropic media. However, there has been growing interest in the wave propagation in viscoelastic and anisotropic media. Recently, Cerveny and Psencik (2005) investigated unbounded viscoelastic anisotropic media and Zhu and Tsvankin (2006) analyzed attenuation anisotropy in transversely isotropic (TI) media.

Although seismic anisotropy has been the subject of active research among seismologists for more than three decades, it is only now that anisotropy is being actively pursued in exploration geophysics, since multi-component seismic data are becoming available and our computational ability has been improved. Anisotropy in a medium essentially represents some type of order therein. Various mechanisms can cause anisotropy in a medium, for example, crystal alignments, aligned cracks, stress etc. The reasons for anisotropy and their classification can be found in Crampin et al. (1984). The most common type of seismic anisotropy under study is vertically

transverse isotropy (VTI), which is characterized by five independent elastic constants. Shales are extensively studied rocks in anisotropy investigations (Hornby et al. (1994) and references therein) and represent a key interest of this dissertation.

Plane wave propagation in homogeneous anisotropic media is solved by the Green-Christoffel equation. Matrix solution of this equation yields polarization and slowness vectors for each wave type (Synge, 1957). These solutions are also obtained with an alternative method called Stroh formalism (Stroh, 1958; Ting, 1996). The Stroh formalism is a more stable compared to the matrix solution of the Green-Christoffel equation. A novel technique has been devised to ensure smoothness in the polarization vector for all integration slownesses.

The reason to consider viscoelastic media is to study the effects of attenuation on wave propagation. There are two main types of attenuation: (1) scattering attenuation; and, (2) intrinsic attenuation. Scattering attenuation is caused by heterogeneity in the rocks. The physical mechanism of intrinsic attenuation is not clearly understood. Irrespective of its mechanism, attenuation is commonly measured by a dimensionless quantity Q, called the quality factor (Johnston and Toksoz, 1981). Most attenuation studies in the literature have been limited to the case of isotropic media.

Energy distribution of propagating plane waves in elastic media are studied by using radiation pattern (Tsvankin and Chesnokov, 1990; Gajewski, 1993). The radiation patterns for P- and S-waves in viscoelastic homogeneous unbounded VTI media are investigated in this dissertation.

Seismic wave propagation through a stack of welded layers has been considered by many researchers. The earliest method called the "transfer matrix method"

3

was developed by Thomson (1950) and Haskell (1953), and is also known as the Thomson-Haskell method. However, this method is inherently unstable for thick layers at high frequencies. This problem was also known as large "fd" problem (f stands for frequency and d for layer thickness) (Lowe, 1995). Dunkin (1965) was the first to solve this instability in the transfer matrix method. Nayfeh (1991) extended the transfer matrix method to include general anisotropy in the layers. Another approach to solve the boundary value problem was developed by Kennett (1974) and Kennett and Kerry (1979). This method is also called the "reflection matrix method". In this method, the wave reverberation operator is expanded into a series of individual reflection-refraction terms. Truncated series of the reverberation operator have been used to study multiple reflections and scattering attenuation (Kennett, 1975). Fryer and Frazer (1984) developed wave propagators in the form of scatterers. Another matrix method was proposed by Rokhlin and Wang (2002) called the "stiffness matrix method". All these matrix methods are after different approaches to the same problem. Here the reflectivity matrix formalism (Fuchs and Muller, 1971) is derived in a concise form which is easy to understand and presents an unconditionally stable approach.

Synthetic seismogram methods in anisotropic media can be divided into two groups: (1) ray theoretical approach; and, (2) full waveform approach. In the ray theoretical approach, the wave equation is basically written as a series expansion of individual rays. Depending on the number of terms used in the series, there are several methods in the ray theory (Cerveny and Ravindra, 1971; Helmberger and Harkrider, 1978). However, in the full waveform approach, there is no series approximation (Cormier and Richards, 1977). Although, the full waveform synthetic

is a time-consuming procedure, yet has the significant advantage of accurate computation of wave motion near critical points resulting in head waves in layers with velocity contrast. In addition, guided waves and leaky modes can be studied for the different sources considered.

Dissertation Outline

This dissertation is organized as follows:

Chapter 2 provides the mathematical treatment of the static Green's tensor of a general anisotropic medium and is applied to the isotropic case to give the analytical solution. This forms the basis for *Chapter 3* where the dynamic Green's tensor is developed. The dynamic Green's tensor in frequency-wavenumber space assumes a simple algebraical form, namely, the solution to Green-Christoffel's equation, which is fundamental to all the computations.

In *Chapter 4*, the layer matrix is formed which facilitates the task of solving the boundary value problem, thereby ensuring the continuity of displacements and tractions throughout a stack of welded anisotropic layers. A numerically stable technique is developed to form the layer matrix. Also, a novel approach is developed to trace the continuity of polarization vectors in critical and supercritical zones.

Chapter 5 gives a concise view of wave propagation through a multilayered media. It forms a reflection-transmission coefficient matrix and is utilized to investigate frequency and thickness - dependent reflection coefficients in multilayered media.

Chapter 6 investigates the reflection coefficients and velocity anisotropy due to the presence of preferentially oriented fractures. A simple model consisting of two half-spaces is considered. In the lower half-space, vertical fracture sets with various

orientations are created and, subsequently, the reflection coefficients are computed for the waves incident from above. The Schoenberg and Sayers (1995) method is used to account for multiple fracture sets in the medium.

Chapter 7 provides a mathematical background and numerical techniques used to generate a full waveform synthetic seismogram. A series of Bessel's functions is used to reduce the overall CPU time of the integration procedure.

In *Chapter 8*, various models, such as homogeneous and multilayered VTI media, are studied. Radiation patterns in homogeneous and attenuating anisotropic media are investigated and the results obtained are utilized to interpret synthetic seismograms in multilayered attenuating VTI media. Frequency and amplitude characteristics of the synthetic seismogram are studied using spectral decomposition.

Chapter 9 is about shale anisotropy. Theoretical shale models of various types are investigated from the standpoint of synthetic seismograms, with the following controlling parameters: preferred orientation of clay particles, aspect ratio of cracks, porosity, and fluid type.

Chapter 10 draws together the main conclusions of this dissertation and outlines the avenue of future investigations.

Chapter 2

Static Green Tensor

2.1 Introduction

This chapter is about a static point force in an elastic anisotropic medium. Green's function approach will be utilized to solve this problem. The theory developed in this chapter is used in the subsequent part of this dissertation. This chapter represents a concise view of a static point force solution.

The theoretical development of the static Green's tensor for anisotropic media has a long history, dating from about 60 years. An example is the publication of the classic paper by Lifshitz and Rozenzweig (1947). The estimation of Green's function for an unbounded space, a half-space and the composite space of anisotropic elastic media has been attempted by various researchers (Eshelby et al., 1953; Head, 1953; Stroh, 1958; Willis, 1970; Chung and Ting, 1995b,a). Chadwick and Smith (1977) presented real form solutions for the displacement and stress. Ting and Lee (1997) obtained the elastostatic Green's function for a general anisotropic medium in three-dimensional space. Pan (2003) derived the complete set of three-dimensional Green's functions or the generalized Mindlin solutions in an anisotropic half-space. Budreck

(1993) expressed Green's function as a bilinear expansion in the eigenfunctions of the linear elastic Hookean operator.

In the first section, the static point force solution to an anisotropic elastic medium is derived. The static Green's tensor is formulated analytically for the isotropic case in the next section and derivatives of that formulation are developed for purposes of practical applications.

2.2   Green Tensor of the Equilibrium Equation

In the static case, the displacements ($\mathbf{u}$) in an anisotropic medium due to the action of body forces ($\mathbf{f}$) are given by the equation:

$$L_{im}u_m = -f_i \tag{2.1}$$

where the operator $L_{im} = \partial_j C_{ijmn} \partial_n$ and f_i is the body force density function. C_{ijmn} is a fourth-rank symmetric elastic tensor; ∂_i represents partial derivatives in the cartesian co-ordinate system; and (i, j, m, n) varies from 1 to 3.

The solution of equation (2.1) can be presented as the convolution of the appropriate Green's tensor, $\mathbf{G}$, with the body force density function, i.e. $\mathbf{U} = \mathbf{G} * \mathbf{f}$. Here, Green's function is essentially a transfer function between the source (e.g. force) and the displacement at the observation point (receiver) which, under proper conditions, represents the effective elastic properties of a general inhomogeneous and anisotropic medium. Green's function for the wave equation is also known as the dyadic Green's

function and is a second rank tensor called Green's Tensor. It can be written in the integral form as:

$$u_m(\mathbf{r}) = \int G_{ml}(\mathbf{r} - \mathbf{r_1}) f_l(\mathbf{r_1}) d\mathbf{r}_1, \qquad (2.2)$$

This integral formula tells us that the force (f_l) acting along $\mathbf{x}_l$ axis at point $\mathbf{r}_1$ causes the displacement components $u_m, m = 1, 2, 3$ at an observation point $\mathbf{r}$. Substituting (2.2) into the equation (2.1), one gets:

$$L_{im} \int G_{ml}(\mathbf{r} - \mathbf{r_1}) f_l(\mathbf{r_1}) d\mathbf{r}_1 = -\delta_{il} f_l(\mathbf{r})$$

$$= -\delta_{il} \int \delta(\mathbf{r} - \mathbf{r_1}) f_l(\mathbf{r_1}) d\mathbf{r}_1$$

or, $$\qquad\qquad L_{im} G_{ml} = -\delta_{il} \delta(\mathbf{r}) \qquad (2.3)$$

Here δ_{il} is the Kronecker delta tensor and $\delta(r)$ is the Dirac-delta function. Green's tensor can be transformed from $\mathbf{r}$-space (spatial domain) to $\mathbf{k}$-space (wavenumber domain) and vice-versa, using the Fourier transform as:

$$G_{ml}(\mathbf{k}) = \int G_{ml}(\mathbf{r}) e^{-i\mathbf{kr}} d\mathbf{r} \qquad (2.4)$$

$$G_{ml}(\mathbf{r}) = \frac{1}{(2\pi)^3} \int G_{ml}(\mathbf{k}) e^{i\mathbf{kr}} d\mathbf{k} \qquad (2.5)$$

Here $G_{ml}(\mathbf{r})$ and $G_{ml}(\mathbf{k})$ are Green's tensors in the spatial domain and wavenumber domain, respectively. Using the definition of the operator L_{im} equation (2.3) can be written as:

$$\partial_j C_{ijmn} \partial_n \int G_{ml}(\mathbf{r})\mathbf{e}^{-\mathbf{ikr}}\mathbf{dr} = -\delta_{il}\int \delta(\mathbf{r})\mathbf{e}^{-\mathbf{ikr}}\mathbf{dr}$$

or, $$C_{ijmn}k_j k_n G_{ml}(\mathbf{k}) = \delta_{il} \qquad (2.6)$$

or, $$\Gamma_{im}G_{ml}(\mathbf{k}) = \delta_{il} \qquad (2.7)$$

where Γ_{im} is the static Green-Christoffel tensor:

$$\Gamma_{im} = C_{ijmn}k_j k_n. \qquad (2.8)$$

Thus, the Green tensor in $\mathbf{k}$-space can be found by taking the inverse of the Green-Christoffel tensor. Thus,

$$G_{ml}(\mathbf{k}) = (\mathbf{\Gamma^{-1}})_{\mathbf{ml}} = \frac{\mathbf{\Gamma}_{\mathbf{ml}}^{\mathbf{adj}}}{\mid \mathbf{\Gamma} \mid} \qquad (2.9)$$

where $\mid \Gamma \mid$ is the determinant of a third order matrix formed by the Green-Christoffel tensor and Γ^{adj} is the adjoint matrix.

2.3 Green Tensor in Isotropic case

The simplest case is the case of isotropic elastic medium where elastic constants C_{ijmn} are dependent only on two parameters. In the case of the two independent parameters being Lamé's parameters, the elastic tensor components C_{ijmn} can be written as:

$$C_{ijmn} = \lambda \delta_{ij} \delta_{mn} + \mu(\delta_{im}\delta_{jn} + \delta_{in}\delta_{jm}) \qquad (2.10)$$

In isotropic media, the Green-Christoffel tensor (2.8) is expanded in the form:

$$\Gamma_{im} = \mu k^2 \delta_{im} + (\lambda + \mu)k_i k_m \qquad (2.11)$$

By taking the inverse of equation (2.11), the Green tensor in **k**-space simplifies to:

$$G_{im}(\mathbf{k}) = \Gamma_{im}^{-1} = \frac{1}{\mu k^2}(\delta_{im} - \chi \nu_{im}) \qquad (2.12)$$

where $\chi = \frac{\lambda+\mu}{\lambda+2\mu}$; $\quad \nu_i = \frac{k_i}{|\mathbf{k}|}$; and $\nu_{im} = \nu_i \nu_m$.

The static Green's tensor in **r**-space is derived by substituting (2.12) into equation (2.5). Thus,

$$\begin{aligned}
G_{im}(\mathbf{r}) &= \frac{1}{(2\pi)^3} \int \frac{1}{\mu k^2}(\delta_{im} - \chi\nu_{im})e^{i\mathbf{kr}}d\mathbf{k} \\
&= \frac{1}{8\pi\mu}\left[\delta_{im}\frac{1}{\pi^2}\int \frac{1}{k^2}e^{i\mathbf{kr}}d\mathbf{k} - \chi\frac{1}{\pi^2}\int \frac{k_i k_m}{k^4}e^{i\mathbf{kr}}d\mathbf{k}\right] \\
&= \frac{1}{8\pi\mu}[\delta_{im}r_{,pp} - \chi r_{,im}] \qquad (2.13)
\end{aligned}$$

The following identity is utilized in the above equation (Shermergor, 1977).

$$r = \frac{-1}{\pi^2}\int \frac{e^{i\mathbf{kr}}}{k^4}d\mathbf{k}$$

11

In order to compute the effective elastic constants of a heterogeneous medium under appropriate conditions, the first and second partial derivatives of the Green tensor in the equation (2.13) is required (Chesnokov et al., 1995).

$$G_{im,l} = \frac{1}{8\pi\mu}[\delta_{im}r_{,ppl} - \chi r_{,iml}]$$

$$G_{im,lq} = \frac{1}{8\pi\mu}[\delta_{im}r_{,pplq} - \chi r_{,imlq}] \qquad (2.14)$$

where $r = \sqrt{\sum x_i^2}$.

The partial derivatives of the **r**-function in the cartesian co-ordinate are given below:

$$r_{,i} = n_i \equiv \frac{x_i}{r}; \qquad r_{,im} = n_{i,m} = \frac{1}{r}(\delta_{im} - n_{im}); \qquad r_{,pp} = \frac{2}{r}$$

$$r_{,iml} = n_{i,ml} = \frac{1}{r^2}(3n_{iml} - n_i\delta_{ml} - n_m\delta_{il} - n_l\delta_{im}); \qquad r_{,ppl} = -\frac{2}{r^2}n_i;$$

$$r_{,imlq} = r^s_{,imlq} + r^f_{,imlq};$$

$$r^s_{,imlq} = -\frac{8\pi}{15}\delta(r)\delta_{imlq}; \qquad r^s_{,pplq} = -\frac{8\pi}{3}\delta(r)\delta_{lq}; \qquad r^s_{,pphh} = -8\pi\delta(r)$$

$$r^f_{,imlq} = n_{i,mlq} \equiv \frac{1}{r^3}[3(n_{im}\delta_{lq} + n_{il}\delta_{mq} + n_{iq}\delta_{ml} + n_{lq}\delta_{im} + n_{ml}\delta_{iq}) - \delta_{imlq} - 15n_{imlq}];$$

$$r^f_{,pplq} = \frac{2}{r^3}(3n_{lq} - \delta_{lq}); \qquad r^f_{,pphh} = 0 \qquad (2.15)$$

Here, $r^s_{,imlq}$ and $r^f_{,imlq}$ are singular (with superscript s) and formal (with superscript f) components of $r_{,imlq}$, respectively. Using expressions (2.15), Green's tensor and its first and second partial derivatives in 2.13 and 2.14 can be written as follows:

$$G_{im}(\mathbf{r}) = \frac{1}{8\pi\mu r}[(2-\chi)\delta_{im} + \chi n_{im}] \tag{2.16}$$

$$G_{im,l}(\mathbf{r}) = \frac{1}{8\pi\mu r}[3\chi n_{iml} + (2-\chi)n_l\delta_{im} - \chi(n_i\delta_{ml} + n_m\delta_{il}] \tag{2.17}$$

$$G_{im,lq}^s(\mathbf{r}) = -\frac{1}{3}\delta(r)[\delta_{im}\delta_{lq} - \frac{1}{5}\chi\delta_{imlq}] \tag{2.18}$$

$$G_{im,lq}^f(\mathbf{r}) = \frac{1}{8\pi\mu r^3}\Big\{(2-\chi)\delta_{im}(3n_{lq} - \delta_{lq}) - \chi\Big[3\big(n_{im}\delta_{lq} + n_{il}\delta_{mq} + n_{iq}\delta_{ml}$$

$$+ n_{mq}\delta_{il} + n_{ml}\delta_{iq}\big) - 2\delta_{imlq} - 15n_{imlq}\Big]\Big\} \tag{2.19}$$

2.4 Summary

The static point force solution in a general anisotropic medium is developed and is expanded to give an analytical solution for the isotropic case. In a more complex case of anisotropy a numerical method is required. The theoretical development in this chapter forms the basis for some techniques used in the subsequent text of the dissertation. Note that the solutions obtained can be extended into the complex domain to solve viscoelastic problems.

Chapter 3

Dynamic Green Tensor

3.1 Introduction

Now consider the problem where the elastic or viscoelastic Green's function is time dependent. This time dependent Green's function is referred to as the dynamic Green's function. In this case, one has to deal with both space and time. The results of this chapter will be used to evaluate point forces in anisotropic attenuating media. The study of more complicated sources will be conducted using multiple point forces.

As a point of interest, Ivanenko and Sokolov (1951) derived the relation between static and dynamic Green's tensor. The dynamic Green's function can be written as an integral over the slowness surface (Duff, 1960). Burrdige (1967) examined the conical points on the slowness surface of media with cubic symmetry. Wang and Achenbach (1993) developed a method based on the Radon transform to obtain 3-dimensional space-time domain elastodynamic solutions for anisotropic solids. Norris (1994) described a procedure to obtain Green's functions for time harmonic source functions. Vshivtsev et al. (1995) proposed a special-purpose decomposition of Green's function which allows one to find the contributions from each wave type

for the wave propagation in anisotropic medium. In the aforementioned method, the Fourier transform is used to calculate the dynamic Green's function.

The second order partial differential equations for Green's function in the space-time domain and frequency-wavenumber domain are both developed in the first section. In the next section, the solutions for the Green's functions in a general anisotropic medium is derived. These results are then applied to obtain Green's functions in analytical form for the special case of an isotropic medium, later in the dissertation. The numerical application of these results of this chapter will be addressed.

3.2 Equation for Generalized Green Function

Elastic wave particle motion is governed by the equation (wave equation):

$$\rho \ddot{U}_i = f_i + \partial_j \sigma_{ij} \tag{3.1}$$

where U_i, $\ddot{U}_i$, f_i, ρ, $\partial_j \sigma_{ij}$ are the i-th components of the displacement, the acceleration, the body force, mass density, and the traction force, respectively.

Stress in its general form is written as:

$$\sigma_{ij}(\epsilon_{mn}) = \sigma_{ij}(0) + \frac{\partial \sigma_{ij}}{\partial \epsilon_{mn}} \epsilon_{mn} + \frac{\partial^2 \sigma_{ij}}{\partial \epsilon_{mn} \partial \epsilon_{pq}} \epsilon_{mn} \epsilon_{pq} + ...$$

$$\sigma_{ij}(\epsilon_{nm}) = \sigma_{ij}(0) + C_{ijmn} \epsilon_{mn} + C_{ijmnpq} \epsilon_{mn} \epsilon_{pq} + ... \tag{3.2}$$

where C_{ijmn} is a fully symmetric fourth rank tensor of elastic constants. C_{ijmnpq} is a sixth rank tensor and it represents the physical nonlinearity. In the expression

15

for strain tensor $\epsilon_{mn} = \frac{1}{2}(\partial_m U_n + \partial_n U_m + \partial_m U_p \partial_n U_p)$, the third term reflects the geometrical nonlinearity. For a medium without initial stress, i.e. $\sigma_{ij}(0) = 0$, one can rewrite expression (3.2) as:

$$\sigma_{ij}(\epsilon_{nm}) = C_{ijmn}\epsilon_{mn} + C_{ijmnpq}\epsilon_{mn}\epsilon_{pq} + \dots \quad (3.3)$$

The linear Hooke's law for an elastic anisotropic medium without initial stress is written in the form:

$$\sigma_{ij} = C_{ijmn}\epsilon_{mn} \quad (3.4)$$

Substituting equation 3.4 into 3.1, one obtains:

$$\rho \ddot{U}_i - \partial_j C_{ijmn} \partial_n U_m = f_i \quad (3.5)$$

Let us represent a solution of equation 3.5 as (similar to equation 2.2):

$$U_m(t, \mathbf{r}) = \int dt' \int d\mathbf{r_1} \quad G_{ml}(t - t'; \mathbf{r} - \mathbf{r_1}) f_l(\mathbf{r_1}), \quad (3.6)$$

where $G_{ml}(t; \mathbf{r})$ is the dynamic Green's function. Substituting equation 3.6 into 3.5, we obtain a linear differential wave operator for Green's function.

$$(\delta_{im}\rho\partial_t^2 - \partial_j C_{ijmn}\partial_n)G_{ml}(t; \mathbf{r}) = \delta_{il}\delta(\mathbf{r})\delta(t) \quad (3.7)$$

16

The above equation can be written in the $(\omega - \mathbf{k})$ domain as (see Appendix A for derivation details):

$$(-\delta_{im}\rho\omega^2 + C_{ijmn}k_jk_n)G_{ml}(\omega;\mathbf{k}) = \delta_{il} \tag{3.8}$$

The above equations 3.7 and 3.8 are partial differential equations of second order. Analytical solutions to these equations are obtained using the Fourier transform in the following section.

3.3   Solution of Green Function

By introducing a differential operator A_{im}, equation 3.7 can be further simplified and written as:

$$(\delta_{im}\partial_t^2 + A_{im})G_{ml}(t;\mathbf{r_1},\mathbf{r_2}) = \delta(t)B_{il}(\mathbf{r_1},\mathbf{r_2}) \tag{3.9}$$

where $A_{im} = -\rho^{-1}\partial_j C_{ijmn}\partial_n$ and $B_{il}(\mathbf{r_1},\mathbf{r_2}) = \delta_{il}\delta(\mathbf{r_1} - \mathbf{r_2})/\sqrt{\rho(\mathbf{r_1})\rho(\mathbf{r_2})}$. Furthermore, equation 3.9 can be written in the matrix form as:

$$(\partial_t^2 + A)G(t;\mathbf{r_1},\mathbf{r_2}) = \delta(t)B(\mathbf{r_1},\mathbf{r_2}) \tag{3.10}$$

Let us find the solution of a second order differential equation 3.10 in a similar way to the equation 3.9 treating A as a numerical parameter.

$$(\partial_t^2 + \alpha)G(t,\alpha) = \delta(t) \tag{3.11}$$

17

The usual method of solving this problem is to take the Fourier transform with respect to the time variable t.

$$G(t, \alpha) = \frac{1}{2\pi} \int G(\omega, \alpha) e^{-i\omega t} d\omega$$

$$\delta(t) = \frac{1}{2\pi} \int e^{-i\omega t} d\omega$$

Substituting the above Fourier representations in equation 3.11, the algebraic expression for the Fourier image $G(\omega, \alpha)$ is written as:

$$(-\omega^2 + \alpha)G(\omega, \alpha) = 1 \qquad \Rightarrow \qquad G(\omega, \alpha) = (\alpha - \omega^2)^{-1}$$

Taking the inverse Fourier transform with respect to ω, one obtains:

$$G(t, \alpha) = \frac{1}{2\pi} \int \frac{1}{(\alpha - \omega^2)} e^{-i\omega t} d\omega = H(t) \frac{\sin(t\sqrt{\alpha})}{\sqrt{\alpha}}.$$

Here $H(t)$ is the Heaviside function with conditions:

$$H(t) = \begin{cases} 1, & t \geq 0 \\ 0, & t < 0 \end{cases}$$

Using the series expansion of a *sine* function, the solution of $G(t, \alpha)$ to equation 3.11 is obtained as an analytical function of parameter α.

$$G(t, \alpha) = H(t) \frac{\sin(t\sqrt{\alpha})}{\sqrt{\alpha}} = H(t) \sum_{n=0}^{\infty} \frac{(-1)^n t^{(2n+1)}}{(2n+1)!} \alpha^n$$

Now let the parameter α be the initial matrix differential operator A and the solution of the equation 3.10 can be presented in the series form as:

$$G(t; \mathbf{r_1}, \mathbf{r_2}) = H(t) \sum_{n=0}^{\infty} \frac{(-1)^n t^{(2n+1)}}{(2n+1)!} A^n B(\mathbf{r_1}, \mathbf{r_2}) \tag{3.12}$$

What follows is the proof that the solution of the form 3.12 satisfies the equation 3.10. Let us find the first and second partial derivatives of $G(t; \mathbf{r_1}, \mathbf{r_2})$ with respect to the time variable t:

$$\frac{\partial}{\partial t} G(t; \mathbf{r_1}, \mathbf{r_2}) = \delta(t) \sum_{n=0}^{\infty} \frac{(-1)^n t^{(2n+1)}}{(2n+1)!} A^n B(\mathbf{r_1}, \mathbf{r_2}) + H(t) \sum_{n=0}^{\infty} \frac{(-1)^n t^{(2n)}}{(2n)!} A^n B(\mathbf{r_1}, \mathbf{r_2})$$

The delta function in the first term comes from the fact that it is the 1st derivative of Heaviside function. Furthermore,

$$\lim_{t \to 0} \sum_{n=0}^{\infty} \frac{(-1)^n t^{(2n+1)}}{(2n+1)!} A^n = 0$$

Therefore,

$$\partial_t G(t; \mathbf{r_1}, \mathbf{r_2}) = H(t) \sum_{n=0}^{\infty} \frac{(-1)^n t^{(2n)}}{(2n)!} A^n B(\mathbf{r_1}, \mathbf{r_2})$$

Second differentiation gives:

$$\partial_t^2 G(t; \mathbf{r_1}, \mathbf{r_2}) = \delta(t) \sum_{n=0}^{\infty} \frac{(-1)^n t^{(2n)}}{(2n)!} A^n B(\mathbf{r_1}, \mathbf{r_2}) + H(t) \sum_{n=1}^{\infty} \frac{(-1)^n t^{(2n-1)}}{(2n-1)!} A^n B(\mathbf{r_1}, \mathbf{r_2})$$

In this case, the coefficient at the delta function is not zero.

$$\lim_{t \to 0} \sum_{n=0}^{\infty} \frac{(-1)^n t^{2n}}{(2n)!} A^n = 1$$

Replacing the sum index $n \to n + 1$, in the second term, one obtains:

$$\partial_t^2 G(t; \mathbf{r_1}, \mathbf{r_2}) = \delta(t) B(\mathbf{r_1}, \mathbf{r_2}) - H(t) \sum_{n=1}^{\infty} \frac{(-1)^n t^{(2n+1)}}{(2n+1)!} A^{n+1} B(\mathbf{r_1}, \mathbf{r_2}) \qquad (3.13)$$

By substituting equations 3.12 and 3.13 in equation 3.10, one can write:

$$(\partial_t^2 + A) G(t; \mathbf{r_1}, \mathbf{r_2}) = \delta(t) B(\mathbf{r_1}, \mathbf{r_2}) - H(t) \sum_{n=1}^{\infty} \frac{(-1)^n t^{(2n+1)}}{(2n+1)!} A^{n+1} B(\mathbf{r_1}, \mathbf{r_2})$$

$$+ A H(t) \sum_{n=1}^{\infty} \frac{(-1)^n t^{(2n+1)}}{(2n+1)!} A^n B(\mathbf{r_1}, \mathbf{r_2})$$

$$= \delta(t) B(\mathbf{r_1}, \mathbf{r_2})$$

Thus, equation 3.12 represents the solution of equation 3.10. Now, let us represent the unit element $B(\mathbf{r_1}, \mathbf{r_2})$ using the eigenfunctions of the operator A. The eigensolutions of the matrix operator A is given by this homogeneous equation:

$$A \mathbf{U}^{\alpha}(\mathbf{k}; \mathbf{r}) = \omega_{\alpha}^2(\mathbf{k}) \mathbf{U}^{\alpha}(\mathbf{k}; \mathbf{r}) \qquad (3.14)$$

Here, α indicates different modes of elastic waves. The eigenfunctions being orthogonal, one can write the unit element $B(\mathbf{r_1}, \mathbf{r_2})$ with weight $\rho(\mathbf{r})$ as:

$$\int d^3 \mathbf{k} \sum_{\alpha=1}^{3} U_i^{\alpha}(\mathbf{k}; \mathbf{r_1}) \overline{U}_l^{\alpha}(\mathbf{k}; \mathbf{r_2}) = \delta_{il} \frac{\delta(\mathbf{r_1} - \mathbf{r_2})}{\sqrt{\rho(\mathbf{r_1}) \rho(\mathbf{r_2})}} \equiv B_{il}(\mathbf{r_1}, \mathbf{r_2}) \qquad (3.15)$$

20

When the operator A acts on the unit element $B(\mathbf{r_1}, \mathbf{r_2})$, equations 3.15 and 3.14 yield the following:

$$A_{mi}B_{il}(\mathbf{r_1}, \mathbf{r_2}) = \int d^3\mathbf{k} \sum_{\alpha=1}^{3} \omega_\alpha^2(\mathbf{k})U_m^\alpha(\mathbf{k};\mathbf{r_1})\overline{U}_l^\alpha(\mathbf{k};\mathbf{r_2}) \qquad (3.16)$$

where the repetitive index i indicates summation from 1 to 3. Any integer power of A results in the eigenvalues with the same integer power. Thus,

$$(A^n)_{mi}B_{il}(\mathbf{r_1}, \mathbf{r_2}) = \int d^3\mathbf{k} \sum_{\alpha=1}^{3} \omega_\alpha^{2n}(\mathbf{k})U_m^\alpha(\mathbf{k};\mathbf{r_1})\overline{U}_l^\alpha(\mathbf{k};\mathbf{r_2}) \qquad (3.17)$$

Any integer power of A is determined by the matrix multiplication:

$$(A^n)_{mi} = A_{mi_1}A_{i_1 i_2}A_{i_2 i_3}....A_{i_{n-1} i}$$

By substituting equation 3.17 into series 3.12, one obtains:

$$G_{ml}(t;\mathbf{r_1}, \mathbf{r_2}) = H(t)\int d^3\mathbf{k} \sum_{\alpha=1}^{3} \frac{1}{\omega_\alpha(\mathbf{k})}\left\{\sum_{n=0}^{\infty}\frac{(-1)^n(t\omega_\alpha(\mathbf{k}))^{(2n+1)}}{(2n+1)!}\right\}U_m^\alpha(\mathbf{k};\mathbf{r_1})\overline{U}_l^\alpha(\mathbf{k};\mathbf{r_2})$$

Using the series expansion of the *sine* function, the above equation is simplified as:

$$G_{ml}(t;\mathbf{r_1}, \mathbf{r_2}) = H(t)\int d^3\mathbf{k} \sum_{\alpha=1}^{3} \frac{\sin(\omega_\alpha(\mathbf{k})t)}{\omega_\alpha(\mathbf{k})}U_m^\alpha(\mathbf{k};\mathbf{r_1})\overline{U}_l^\alpha(\mathbf{k};\mathbf{r_2}) \qquad (3.18)$$

Thus, if the spectrum of eigenvalues $\omega_\alpha^2(\mathbf{k})$ and the eigenfunction $U_i^\alpha(\mathbf{k};\mathbf{r})$ of the operator A determined by the homogeneous equation:

$$A_{im}U_m^\alpha(\mathbf{k};\mathbf{r}) = \omega_\alpha^2(\mathbf{k})U_i^\alpha(\mathbf{k};\mathbf{r}) \qquad (3.19)$$

21

is known, then any integer power of A can be obtained using equation 3.17 . Once A^n is found, any analytical function of the operator can be calculated. Thus, if the spectrum of the operator A is known, the Green function is determined according to equation 3.18. By substituting the differential form of operator A_{im} from equation 3.9 into equation 3.19, one obtains:

$$-\partial_j \left(C_{ijmn}\partial_n U_m^\alpha(\mathbf{k};\mathbf{r})\right) = \rho(\mathbf{r})\omega_\alpha^2(\mathbf{k})U_i^\alpha(\mathbf{k};\mathbf{r}) \tag{3.20}$$

Let us consider the simplest case of homogeneous infinite media, where eigenfunctions of the operator A are harmonic waves:

$$U_i^\alpha(\mathbf{k};\mathbf{r}) = \frac{1}{\sqrt{(2\pi)^3\rho}}u_i^\alpha(\mathbf{k})e^{i\mathbf{k}.\mathbf{r}} \tag{3.21}$$

By substituting equation 3.21 into 3.20, one obtains:

$$C_{ijmn}k_j k_n u_m^\alpha(\mathbf{k}) = \rho\omega^2 u_i^\alpha(\mathbf{k}) \tag{3.22}$$

where $u_i^\alpha(\mathbf{k})$ is the eigenvectors of the Green-Christoffel tensor $\Gamma_{im} = C_{ijmn}k_j k_n$. The normalization factor of $\sqrt{(2\pi)^3\rho}$ in equation 3.21 is derived from the general condition of orthogonality for eigenfunctions having weight $\rho(\mathbf{r})$:

$$\int d^3\mathbf{r}\rho(\mathbf{r}) \sum_{i=1}^{3} U_i^\alpha(\mathbf{k_1};\mathbf{r})\overline{U}_i^\beta(\mathbf{k_2};\mathbf{r}) = \delta^{\alpha\beta}\delta(\mathbf{k_1} - \mathbf{k_2})$$

The eigenvalue solution of equation 3.22 is found from the following determinant:

$$|C_{ijmn}k_jk_n - \delta_{im}\rho\omega^2| = 0$$

or, $$|C_{ijmn}\nu_j\nu_n - \delta_{im}\rho V_\alpha^2(\nu)| = 0 \qquad (3.23)$$

where $\nu_i = \frac{k_i}{|\mathbf{k}|}$ and $\mathbf{k} = \frac{\omega(\nu)}{V_\alpha(\nu)}$. The solutions of this equation correspond to the three characteristic wave velocities $V_\alpha, \alpha = 1, 2, 3$.

Let us replace the integration variable $\mathbf{k}$ in equation 3.18 with frequency ω and spherical coordinate angles (azimuthal angle θ, and polar angle ϕ).

$$\mathbf{k} = \frac{1}{V_\alpha(\mathbf{k})} \begin{pmatrix} \omega \sin(\phi)\cos(\theta) \\ \omega \sin(\phi)\sin(\theta) \\ \omega \cos(\phi) \end{pmatrix} \quad \text{and} \quad \int d\nu = \int_0^{2\pi} d\theta \int_0^\pi \sin\phi d\phi \qquad (3.24)$$

The Jacobian transformation of 3.24 is:

$$\left| \frac{\partial(k_1, k_2, k_3)}{\partial(\omega, \phi, \theta)} \right| = \frac{\omega^2 \sin\phi}{V_\alpha^3(\phi, \theta)} \implies d^3\mathbf{k} = \omega^2 \sin\phi V_\alpha^3(\nu) d\omega d\phi d\theta \qquad (3.25)$$

Substituting 3.24 with Jacobian 3.25 and eigenfunction 3.21 into the Green function in 3.18, one obtains:

$$G_{ml}(t; \mathbf{r_1}, \mathbf{r_2}) = H(t) \int_{-\infty}^\infty d\omega \sin(\omega t) \omega \int_{|\mathbf{n}=1|} d\mathbf{n} \frac{u_m^\alpha(\mathbf{n}) u_l^\alpha(\mathbf{n})}{2\rho(2\pi V_\alpha(\mathbf{n}))^3} e^{\left(\frac{i\omega}{V_\alpha(\mathbf{n})}(\mathbf{n}.(\mathbf{r_1} - \mathbf{r_2}))\right)}$$

In the general case of anisotropy, numerical techniques are required to solve the above equation and are going to be computationally intensive. However, in a special case of an isotropic medium, the above equations simplify.

3.4   Dynamic Green Tensor in Isotropic case

The elasticity tensor in the isotropic case is dependent only on two parameters. In the case that the two parameters are λ, μ (Lamé parameters), the elasticity tensor is given as:

$$C_{ijmn} = \lambda \delta_{ij} \delta_{mn} + \mu(\delta_{im}\delta_{jn} + \delta_{in}\delta_{jm}) \tag{3.26}$$

Substituting equation 3.26 in 3.8, one gets:

$$(-\delta_{im}\rho\omega^2 + (\lambda + \mu)k_i k_m + \mu k^2 \delta_{im})G_{ml}(\omega; \mathbf{k}) = \delta_{il} \tag{3.27}$$

The solution for $G_{ml}(\omega; \mathbf{k})$ is given by:

$$G_{ml}(\omega; \mathbf{k}) = \frac{1}{\mu k^2 - \rho\omega^2}\left[\delta_{ml} - \frac{(\lambda + \mu)k_m k_l}{(\lambda + 2\mu)k^2 - \rho\omega^2}\right]$$

$$\text{or,} \quad G_{ml}(\omega; \mathbf{k}) = \frac{1}{\rho(V_S^2 k^2 - \omega^2)}\left[\delta_{ml} - \frac{(V_P^2 - V_S^2)k_m k_l}{V_P^2 k^2 - \omega^2}\right] \tag{3.28}$$

where $V_P = \sqrt{(\lambda + 2\mu)/\rho}$ and $V_S = \sqrt{\mu/\rho}$.

24

Taking the Fourier image of the above equation, it can be shown that the Green function in space-time is:

$$
\begin{aligned}
G_{ml}(t; \mathbf{r}) = {} & \frac{1}{4\pi\rho V_P^2 r} \delta(t - t_P) n_m n_l \\
& + \frac{1}{4\pi\rho V_S^2 r} \delta(t - t_S) \left[\delta_{ml} - n_m n_l \right] \\
& + \frac{1}{4\pi\rho r^3} \left[3 n_m n_l - \delta_{ml} \right] t H(t - t_P) H(t_S - t) \qquad (3.29)
\end{aligned}
$$

where $t_P = r/V_P$, $t_S = r/V_S$ and $n_i = r_i/|\mathbf{r}|$

3.5 Summary

Analytical expressions for the dynamic Green tensor are developed using the Fourier transform method. These expressions are expanded in the case of isotropic media which are simple and easy to compute. However, in the general case of anisotropy, computations based on these analytical expressions are fairly time consuming. Therefore, numerical techniques are required to compute Green's functions, which are developed in the subsequent chapters.

Chapter 4

Layer Matrix

4.1 Introduction

A layer matrix is of sextic (6x6) form in which columns represent upgoing and downgoing waves for each wave types and rows represent cartesian components of polarization and traction vectors. The layer matrix formalism facilitates the task of solving the boundary value problem of wave propagation throughout a stack of welded layers. Therefore, the layer matrix is also referred to as the propagator matrix.

There are two types of approaches and algorithms used to form the layer matrix for a homogeneous region of general anisotropic medium. The first approach is based on the solution of a sixth order polynomial and finding eigensolutions of the Green-Christoffel tensor (e.g. Fedorov (1968), Rokhlin et al. (1986)). The second approach involves calculations of displacement and stress vectors simultaneously and is often referred to as Sextic formalism, or Stroh formalism (Stroh, 1958, 1962; Crampin, 1981; Mandal and Toksoz, 1990; Ting, 1996). Synge (1957) suggested to take into

account the sign of the imaginary part of the eigensolutions to distinguish between upgoing and downgoing waves.

Finding the eigensolutions in the Stroh formalism is found to be computationally more stable. However, in order to take partial derivatives of Green's tensor, it is desired to form polynomial with respect to slowness and this is accurately achieved with the Green-Christoffel equation. In this dissertation, a combination of both approaches is followed to give a more robust technique for building a layer matrix and excitation vector due to source. The next two sections are devoted to the first type of approach, showing the derivation and a programmable solution of the Green-Christoffel equation leading to the layer matrix. The second approach is in the fourth section giving the details of the Stroh formalism. In the fifth section, a technique is discussed to combine these two methods and a novel technique is also devised to safely track polarization of two shear waves across singularity points (or acoustic axes).

4.2   Green-Christoffel Equation

Newton's second law of motion and the definition of resultant force density from continuum mechanics i.e. $f_i = \partial_j \sigma_{ij}$ are combined to give

$$\partial_j \sigma_{ij} = \rho \partial_t^2 u_i \tag{4.1}$$

where $\sigma_{ij} = C_{ijkl}\epsilon_{kl}$, ρ-mass density and $\mathbf{u}$ is displacement vector. Using equation 3.4, equation (4.1) can be expanded as:

$$\partial_j C_{ijkl}\epsilon_{kl} + C_{ijkl}\partial_j\epsilon_{kl} = \rho\partial_t^2 u_i$$

$$\Rightarrow \quad C_{ijkl}\partial_j\epsilon_{kl} = \rho\partial_t^2 u_i \tag{4.2}$$

because $\partial_j C_{ijkl} = 0$ in any homogeneous medium.

Furthermore, since $\epsilon_{kl} = \frac{1}{2}(\partial_l u_k + \partial_k u_l)$, one can write equation (4.2) as:

$$C_{ijkl}\partial_j\partial_l u_k = \rho\partial_t^2 u_i \tag{4.3}$$

Let us seek a solution to the equation (4.3) in the form of a plane wave.

$$u_i = A_i e^{-ik(n_m x_m - vt)} \tag{4.4}$$

Substituting u_i from (4.4) into equation (4.3), one obtains:

$$\rho v^2 u_i = C_{ijkl} n_j n_l u_k$$

or, $$\rho v^2 \delta_{ik} u_k = C_{ijkl} n_j n_l u_k$$

or, $$(\Gamma_{ik} - \rho v^2 \delta_{ik})u_k = 0 \tag{4.5}$$

where $\Gamma_{ik} = C_{ijkl} n_j n_l$. Equation (4.5) is called the Green-Christoffel equation.

4.3 Solution of the Green-Christoffel Equation

Let us rewrite the Green-Christoffel equation (4.5) in terms of slowness $p_i = \frac{n_i}{v}$ (n_i and v are direction cosines and the phase velocity, respectively) and density normalized elasticity tensor a_{ijkl}.

$$(a_{ijkl}p_j p_l - \delta_{ik})u_k = 0 \qquad (4.6)$$

The above system of homogeneous linear equations has a non-trivial solution for the polarization vector $\mathbf{u}$ if and only if the matrix $(\mathbf{G})$ of the system has a vanishing determinant:

$$\det(G_{ik}) = |a_{ijkl}p_j p_l - \delta_{ik}| = 0 \qquad (4.7)$$

Expansion of the $(\mathbf{G})$ matrix entries:

$$G_{11} = a_{55}p_3^2 + 2(a_{15}p_1 + a_{56}p_2)p_3 + a_{11}p_1^2 + 2a_{16}p_1 p_2 + a_{66}p_2^2 - 1$$

$$G_{22} = a_{44}p_3^2 + 2(a_{46}p_1 + a_{24}p_2)p_3 + a_{66}p_1^2 + 2a_{26}p_1 p_2 + a_{22}p_2^2 - 1$$

$$G_{33} = a_{33}p_3^2 + 2(a_{35}p_1 + a_{34}p_2)p_3 + a_{55}p_1^2 + 2a_{45}p_1 p_2 + a_{44}p_2^2 - 1$$

$$G_{12} = a_{45}p_3^2 + [(a_{14} + a_{56})p_1 + (a_{46} + a_{25})p_2]p_3 + a_{16}p_1^2 + (a_{12} + a_{66})p_1 p_2 + a_{26}p_2^2$$

$$G_{13} = a_{35}p_3^2 + [(a_{13} + a_{55})p_1 + (a_{36} + a_{45})p_2]p_3 + a_{15}p_1^2 + (a_{14} + a_{56})p_1 p_2 + a_{46}p_2^2$$

$$G_{23} = a_{34}p_3^2 + [(a_{36} + a_{45})p_1 + (a_{23} + a_{44})p_2]p_3 + a_{56}p_1^2 + (a_{46} + a_{25})p_1 p_2 + a_{24}p_2^2$$

Voigt notation is utilized to present the fourth-rank elasticity tensor as a second-rank tensor. The determinant of $(\mathbf{G})$ is a sixth order polynomial in p_3 (i.e. z-component of slowness vector $\mathbf{p}$) for any given values of horizontal slownesses. Thus,

there will be six solutions for p_3 which fall into two equinumerous groups of upgoing and downgoing waves, respectively. The p_3 root can be purely real or complex. In the case of a medium with a horizontal plane of symmetry, one can separate upgoing waves from downgoing waves based on the sign of vertical slowness (p_3) real and imaginary parts (i.e. +ve for upgoing and -ve for downgoing). However, if xy-plane is not a symmetry plane, the distinction between upgoing and downgoing waves becomes problematic. In section 4.5, a combination of various approaches is discussed to make the distinction between upgoing waves and downgoing waves and types of waves (i.e. P, S_1, S_2).

Having calculated the roots of the sixth-order polynomial which gives phase slowness (and hence phase velocity), the next step is to calculate polarization vectors for each value of p_3. In order to do this, we construct $\mathbf{W}$ – the adjoint matrix of $\mathbf{G}$, and compute the polarization vector components (u_i) as follows:

$$W_{11} = G_{22}G_{33} - G_{23}G_{23}, \quad W_{22} = G_{33}G_{11} - G_{13}G_{13}, \quad W_{33} = G_{11}G_{22} - G_{12}G_{12}$$

$$W_{12} = G_{13}G_{23} - G_{12}G_{13}, \quad W_{13} = G_{12}G_{23} - G_{13}G_{22}, \quad W_{23} = G_{13}G_{12} - G_{23}G_{11}$$

$$\Delta = W_{11} + W_{22} + W_{33}$$

and

$$u_i^2 = W_{ii}/\Delta \tag{4.8}$$

Equation (4.8) gives all three components of the polarization vector. However, the aforementioned formula cannot warrant the polarization vector to be continuous as the horizontal slowness increases in a given direction. In this case, it is advised to

select one of the displacements which has the maximum absolute value and correct the relative sign of the other displacement vector using the following equation:

$$u_i u_j = W_{ij}/\Delta \tag{4.9}$$

Thus, the phase slownesses and the associated polarizations are obtained subject to the requisite conditions. However, in some propagation directions, the S1 and S2 wave velocities may coincide rendering the adjugate tensor zero. Propagation directions with this property are called acoustic axes. The higher the symmetry in the media, the higher the number of acoustic axes. This creates numerical instability. However, it can be avoided using the perturbation approach. Another method discussed in the next section appears to be numerically more stable to compute phase slownesses and polarizations in general anisotropic media.

Once the polarization vectors for a given slowness are calculated, the traction vector in the Z-direction is computed using the following formula:

$$\sigma_{i3} = C_{i3kl} p_k u_l \tag{4.10}$$

Thus, the layer matrix with displacement-stress vector $[u_i, \sigma_{i3}]$ is formed.

4.4 Stroh Formalism

The advantage of this approach is that it gives displacement-stress vectors directly without going into the complexity of solving the Green-Christoffel equation. For wave propagation in a layered media, the displacements and tractions are assumed

31

to be continuous throughout the multilayered medium, including its interfaces. The traction vector at a unit plane area parallel to a layer interface is σ_{i3} and can be written as:

$$\sigma_{i3} = C_{i3kl}\partial_l u_k \tag{4.11}$$

$$\text{or,} \quad \sigma_{i3} = \begin{pmatrix} E_x^{ik}\partial_x & E_y^{ik}\partial_y & E_z^{ik}\partial_z \end{pmatrix} \begin{pmatrix} u_x \\ u_y \\ u_z \end{pmatrix} \tag{4.12}$$

where

$$\mathbf{E}_x = E_x^{ik} = C_{i3k1}, \quad \mathbf{E}_y = E_y^{ik} = C_{i3k2}, \quad \text{and} \quad \mathbf{E}_z = E_z^{ik} = C_{i3k3} \tag{4.13}$$

The displacement and traction vector in the form of a plane wave can be expressed as:

$$\sigma_{i3} = T_i \exp[-i\omega(p_x x + p_y y - t)] \tag{4.14}$$

$$u_i = U_i \exp[-i\omega(p_x x + p_y y - t)] \tag{4.15}$$

Substituting equations (4.14) and (4.15) into equation (4.12), one obtains:

$$
\begin{pmatrix} T_x \\ T_y \\ T_z \end{pmatrix} = -i\omega(p_x\mathbf{E}_x + p_y\mathbf{E}_y)\begin{pmatrix} U_x \\ U_y \\ U_z \end{pmatrix} + \mathbf{E}_z\partial_z\begin{pmatrix} U_x \\ U_y \\ U_z \end{pmatrix} \tag{4.16}
$$

$$
\text{or,} \quad \partial_z\begin{pmatrix} U_x \\ U_y \\ U_z \end{pmatrix} = i\omega\mathbf{E}_z^{-1}[(p_x\mathbf{E}_x + p_y\mathbf{E}_y)]\begin{pmatrix} U_x \\ U_y \\ U_z \end{pmatrix} + \mathbf{E}_z^{-1}\begin{pmatrix} T_x \\ T_y \\ T_z \end{pmatrix} \tag{4.17}
$$

$$
\text{or,} \quad \mathbf{U},z = i\omega\mathbf{E}_z^{-1}[(p_x\mathbf{E}_x + p_y\mathbf{E}_y)]\mathbf{U} + \mathbf{E}_z^{-1}\mathbf{T} \tag{4.18}
$$

$$
\text{or,} \quad \mathbf{U},z = i\omega\mathbf{M}\,\mathbf{U} + \mathbf{N}\,\mathbf{T} \tag{4.19}
$$

where $\mathbf{M} = \mathbf{E}_z^{-1}[(p_x\mathbf{E}_x + p_y\mathbf{E}_y)]$ and $\mathbf{N} = \mathbf{E}_z^{-1}$.

Now let us look at equation (4.2). Substituting equation (4.15) into (4.2), one obtains:

$$
\omega^2\rho\mathbf{U} = \omega^2(p_x^2 F_{xx}^{ik} + p_y^2 F_{yy}^{ik} + 2p_xp_y F_{xy}^{ik})\mathbf{U} - F_{zz}^{ik}\mathbf{U},zz + 2i\omega(p_x F_{zx}^{ik} + p_y F_{yz}^{ik})\mathbf{U},z \tag{4.20}
$$

where

$$\mathbf{F}_{xx} = F_{xx}^{ik} = C_{i1k1},$$

$$\mathbf{F}_{yy} = F_{yy}^{ik} = C_{i2k2},$$

$$\mathbf{F}_{zz} = F_{zz}^{ik} = C_{i3k3},$$

$$2\mathbf{F}_{xy} = 2F_{xy}^{ik} = C_{i1k2} + C_{i2k1},$$

$$2\mathbf{F}_{yz} = 2F_{yz}^{ik} = C_{i2k3} + C_{i3k2},$$

$$2\mathbf{F}_{zx} = 2F_{zx}^{ik} = C_{i3k1} + C_{i1k3}, \tag{4.21}$$

From equalities in (4.13) and (4.21), we get $2\mathbf{F}_{zx} = (\mathbf{E}_x + \mathbf{E}_x^T)$, $2\mathbf{F}_{yz} = (\mathbf{E}_y + \mathbf{E}_y^T)$, and $\mathbf{F}_{zz} = \mathbf{E}_z$. Furthermore, differentiating equation (4.19) with respect to z leads to:

$$\begin{aligned}
\mathbf{U}_{,zz} &= i\omega\mathbf{M}\,\mathbf{U}_{,z} + \mathbf{N}\,\mathbf{T}_{,z} \\
&= i\omega\mathbf{M}(i\omega\mathbf{M}\,\mathbf{U} + \mathbf{N}\,\mathbf{T}) + \mathbf{N}\,\mathbf{T}_{,z} \\
&= -\omega^2\mathbf{M}\,\mathbf{M}\,\mathbf{U} + i\omega\mathbf{M}\,\mathbf{N}\,\mathbf{T} + \mathbf{N}\,\mathbf{T}_{,z}
\end{aligned} \tag{4.22}$$

Substituting values of $\mathbf{U}_{,zz}$ and $\mathbf{U}_{,z}$ in equation (4.20), one obtains:

$$\begin{aligned}
\omega^2\rho\mathbf{U} = {}& \omega^2(p_x^2\mathbf{F}_{xx} + p_y^2\mathbf{F}_{yy} + 2p_xp_y\mathbf{F}_{xy})\mathbf{U} \\
& - \mathbf{F}_{zz}[-\omega^2\mathbf{M}\,\mathbf{M}\,\mathbf{U} + i\omega\mathbf{M}\,\mathbf{N}\,\mathbf{T} + \mathbf{N}\,\mathbf{T}_{,z}] \\
& + 2i\omega(p_x\mathbf{F}_{zx} + p_y\mathbf{F}_{yz})(i\omega\mathbf{M}\,\mathbf{U} + \mathbf{N}\,\mathbf{T})
\end{aligned} \tag{4.23}$$

34

or,

$$0 = \omega^2[p_x^2\mathbf{F}_{xx} + p_y^2\mathbf{F}_{yy} + 2p_xp_y\mathbf{F}_{xy} + \mathbf{F}_{zz}\mathbf{M}\,\mathbf{M} - 2(p_x\mathbf{F}_{zx} + p_y\mathbf{F}_{yz})\mathbf{M} - \rho\mathbf{I}]\mathbf{U}$$

$$- i\omega[\mathbf{F}_{zz}\mathbf{M}\,\mathbf{N} - 2(p_x\mathbf{F}_{zx} + p_y\mathbf{F}_{yz})\mathbf{N}]\mathbf{T} - \mathbf{F}_{zz}\mathbf{N}\,\mathbf{T}_{,z} \tag{4.24}$$

Some of the terms in the above equation can be expanded as follows:

$$\mathbf{F}_{zz}\mathbf{N} = \mathbf{E}_z\,\mathbf{E}_z^{-1} = \mathbf{I} \tag{4.25}$$

$$\mathbf{F}_{zz}\mathbf{M}\,\mathbf{M} = \mathbf{E}_z\mathbf{E}_z^{-1}(p_x\mathbf{E}_x + p_y\mathbf{E}_y)\mathbf{E}_z^{-1}(p_x\mathbf{E}_x + p_y\mathbf{E}_y)$$

$$= (p_x\mathbf{E}_x + p_y\mathbf{E}_y)\mathbf{E}_z^{-1}(p_x\mathbf{E}_x + p_y\mathbf{E}_y) \tag{4.26}$$

$$2(p_x\mathbf{F}_{zx} + p_y\mathbf{F}_{yz})\mathbf{M} = (p_x(\mathbf{E}_x + \mathbf{E}_x^T) + p_y(\mathbf{E}_y + \mathbf{E}_y^T))\mathbf{E}_z^{-1}(p_x\mathbf{E}_x + p_y\mathbf{E}_y)$$

$$= \mathbf{F}_{zz}\mathbf{M}\,\mathbf{M} + (p_x\mathbf{E}_x^T + p_y\mathbf{E}_y^T)\mathbf{E}_z^{-1}(p_x\mathbf{E}_x + p_y\mathbf{E}_y) \tag{4.27}$$

$$\mathbf{F}_{zz}\mathbf{M}\,\mathbf{N} = \mathbf{E}_z\mathbf{E}_z^{-1}(p_x\mathbf{E}_x + p_y\mathbf{E}_y)\mathbf{E}_z^{-1} = (p_x\mathbf{E}_x + p_y\mathbf{E}_y)\mathbf{E}_z^{-1} \tag{4.28}$$

$$2(p_x\mathbf{F}_{zx} + p_y\mathbf{F}_{yz})\mathbf{N} = (p_x(\mathbf{E}_x + \mathbf{E}_x^T) + p_y(\mathbf{E}_y + \mathbf{E}_y^T))\mathbf{E}_z^{-1}$$

$$= \mathbf{F}_{zz}\mathbf{M}\,\mathbf{N} + (p_x\mathbf{E}_x^T + p_y\mathbf{E}_y^T)\mathbf{E}_z^{-1} \tag{4.29}$$

Substituting equations from (4.25) to (4.29) into equation (4.24), one obtains:

$$\mathbf{T}_{,z} = \omega^2[p_x^2(\mathbf{F}_{xx} - \mathbf{E}_x^T\mathbf{E}_z^{-1}\mathbf{E}_x) + p_y^2(\mathbf{F}_{yy} - \mathbf{E}_y^T\mathbf{E}_z^{-1}\mathbf{E}_y)$$

$$+ p_xp_y(2\mathbf{F}_{xy} - \mathbf{E}_x^T\mathbf{E}_z^{-1}\mathbf{E}_y - \mathbf{E}_y^T\mathbf{E}_z^{-1}\mathbf{E}_x) - \rho\mathbf{I}]\,\mathbf{U}$$

$$+ i\omega[(p_x\mathbf{E}_x^T + p_y\mathbf{E}_y^T)\mathbf{E}_z^{-1}]\,\mathbf{T} \tag{4.30}$$

or, $$\mathbf{T}_{,z} = \omega^2\mathbf{Q}\,\mathbf{U} + i\omega\mathbf{R}\,\mathbf{T} \tag{4.31}$$

where

$$\mathbf{Q} = p_x^2 \mathbf{Q_1} + p_y^2 \mathbf{Q_2} + p_x p_y \mathbf{Q_3} - \rho \mathbf{I}$$

$$\mathbf{Q_1} = \mathbf{F}_{xx} - \mathbf{E}_x^T \mathbf{E}_z^{-1} \mathbf{E}_x$$

$$\mathbf{Q_2} = \mathbf{F}_{yy} - \mathbf{E}_y^T \mathbf{E}_z^{-1} \mathbf{E}_y$$

$$\mathbf{Q_3} = 2\mathbf{F}_{xy} - \mathbf{E}_x^T \mathbf{E}_z^{-1} \mathbf{E}_y - \mathbf{E}_y^T \mathbf{E}_z^{-1} \mathbf{E}_x$$

and, $\qquad \mathbf{R} = (p_x \mathbf{E}_x^T + p_y \mathbf{E}_y^T) \mathbf{E}_z^{-1}$ \hfill (4.32)

Combining (4.19) and (4.31), one can write:

$$\partial_z \begin{pmatrix} \mathbf{U} \\ \boldsymbol{\tau} \end{pmatrix} = i\omega \begin{pmatrix} \mathbf{M} & \mathbf{N} \\ -\mathbf{Q} & \mathbf{R} \end{pmatrix} \begin{pmatrix} \mathbf{U} \\ \boldsymbol{\tau} \end{pmatrix} = i\omega \begin{pmatrix} \mathbf{M} & \mathbf{N} \\ -\mathbf{Q} & \mathbf{M}^T \end{pmatrix} \begin{pmatrix} \mathbf{U} \\ \boldsymbol{\tau} \end{pmatrix} \qquad (4.33)$$

where $\boldsymbol{\tau} = \mathbf{T}/i\omega$ and $\mathbf{R} = \mathbf{M}^T$. Equation (4.33) is a set of linear differential equations which has the form:

$$\partial_z \mathbf{b}(z) = i\omega \mathbf{A}(z) \, \mathbf{b}(z) \qquad (4.34)$$

where $\mathbf{b}$ is a displacement-traction vector and $\mathbf{A}$ is called the system matrix of sextic (6x6) form parameterized by elastic constants C_{ijkl}, density and horizontal slownesses.

4.5 Computational Aspects of Layer Matrix

A combination of two approaches is proposed to give a more robust technique to form a layer matrix and source excitation vector in the following steps:

1. For a given horizontal slowness, the eigenvalues of the sextic matrix A (see equation 4.34) represent vertical phase slownesses.

2. Using these horizontal and vertical slownesses, Green-Christoffel matrix $\mathbf{G}$ is computed. Each entry of this matrix is a polynomial of the second order in p_3 and can be written as:

$$G_{ik} = C_{ik}p_3^2 + D_{ik}p_3 + E_{ik} \tag{4.35}$$

where

$$C_{ik} = a_{i3k3}$$

$$D_{ik} = (a_{i1k3} + a_{i3k1})p_1 + (a_{i2k3} + a_{i3k2})p_2$$

$$E_{ik} = (a_{i1k2} + a_{i2k1})p_1p_2 + a_{i1k1}p_1^2 + a_{i2k2}p_2^2 - \delta_{ik} \tag{4.36}$$

Furthermore, a subroutine is implemented which outputs all the polynomial coefficients of a 6th order polynomial in p_3. This is to facilitate calculation of partial derivatives of G_{ik} with respect to p_3. This is needed to compute the excitation vector for a point force in an anisotropic layer.

3. The adjoint matrix of G is formed using the set of equation 4.8 and normalized to give the polarization vectors.

4. In order to distinguish between upgoing and downgoing waves, two criteria are used depending on whether the phase slowness is real or complex.

   - If the phase slowness is real then the vertical component of group velocity is used: +ve for upgoing and -ve for downgoing waves.

   - If the phase slowness is complex then the sign of the imaginary part of phase slowness is used: -ve for upgoing and +ve for downgoing waves.

5. The traction vector is formed using equation 4.10.

   The above criteria assume that the Z-axis is oriented upwards.

It is observed that the S1 and S2 waves change their polarization dramatically when their phase slowness surfaces cross each other. Furthermore, P, S1, and S2 polarization vectors change considerably in the critical and supercritical zones. Therefore, it is desirable to have a sign convention for P, S1, and S2 polarizations and a method to trace the continuity of polarization vectors. This is important in order to get a smooth behavior of the reflection coefficients and the associated phases (discussed in the next chapter). A novel method is devised to track the continuity and put the polarization in a right hand co-ordinate system as follows:

- S1 and S2 waves are polarized perpendicular to each other. With adequate sampling of horizontal slowness, one can safely assume that, if polarization vector of S1 and S2 rotate from their previous orientation, they do so by a small angle. Thus, the continuity of S1 and S2 can be tracked by computing the rotation angle of S1 and S2 at the current point with respect to the previous point.

- The signs of polarization vectors are governed so as to have the P-wave polarization make an acute angle with the P-wave propagation direction, with S1 and S2 polarization vectors and P-wave polarization vectors forming a right-hand frame.

4.6   Summary

The Stroh formalism is preferred over the polynomial solution of the Green-Christoffel equation to compute vertical slowness. However, in order to have better accuracy, it is desired to compute the partial derivatives of Green's tensor using polynomial formation of the Green-Christoffel equation. Therefore, a combined method gives a more numerically robust technique to form a layer matrix along with an excitation vector. A new technique is developed to make polarization vectors continuous and follow a sign convention in order to have consistent reflection coefficients. The layer matrix formulated in this chapter will be used in the subsequent chapters to compute reflection coefficients in a multilayered anisotropic media as well as the synthetic seismograms.

Chapter 5

Wavefield and Reflection Coefficients

5.1 Introduction

Here a modified reflectivity method is used to consider wave propagation in a multi-layered anisotropic medium. The continuity principle requires that the displacement and stress vectors be continuous throughout the medium, including the interfaces. Thus, there are two aspects of wave propagation in a multilayered medium: First, wave propagation in a homogeneous medium (i.e. within a layer) and second, wave propagation across an interface which gives rise to the reflection coefficients. The reflection coefficients are often utilized to evaluate amplitude versus offset and azimuth (AVOAz) effects.

Most published papers treat reflection-refraction coefficients as an intermediate step in the course of computation of synthetic seismograms. A comprehensive review of various methods of this intermediary step can be found in the papers by Lowe (1995) and Rokhlin and Wang (2002). For wave propagation through a multilayered medium, the transfer matrix method was developed by Thomson (1950) and Haskell (1953). However, it was found to be computationally unstable for thick layers at high

frequencies (Lowe, 1995). Though this method was developed for isotropic media, it was extended for general anisotropic media by Nayfeh (1991). The computational instability of the transfer matrix method for isotropic media was resolved by Dunkin (1965) and was generalized for anisotropic media by Castaings and Hosten (1994). Knopoff (1964) proposed a global matrix method. Kennett (1974) and Kennett and Kerry (1979) developed a reflection matrix method using the wave reverberations in isotropic layers. Booth and Crampin (1983) extended the reflection matrix method to orthotropic symmetry, and Fryer and Frazer (1984) further extended it to include generally anisotropic layers. Rokhlin and Wang (2002) developed a recursive stiffness matrix method in a manner similar to the reflection matrix method.

This chapter is devoted to the implementation of the layer matrix formulation in a multilayered general anisotropic medium. In the following section, a recursive method is developed to obtain the wavefield at any point in the multilayered medium. The wavefield due to a point force is considered in section 5.3. In section 5.4, a method is developed to eliminate repeat computation in the case of a multi-channel receiver system. Apart from the wavefield determination, another outcome of this implementation of the layer matrix is a special purpose matrix representation of plane wave reflection and refraction coefficients associated with an interface. In section 5.5, the effects of anisotropy on reflection coefficients are analyzed. Furthermore, reflection coefficients are computed at an interface of a multilayered medium to study the effects of frequency content of propagating waves and the thickness of a layer.
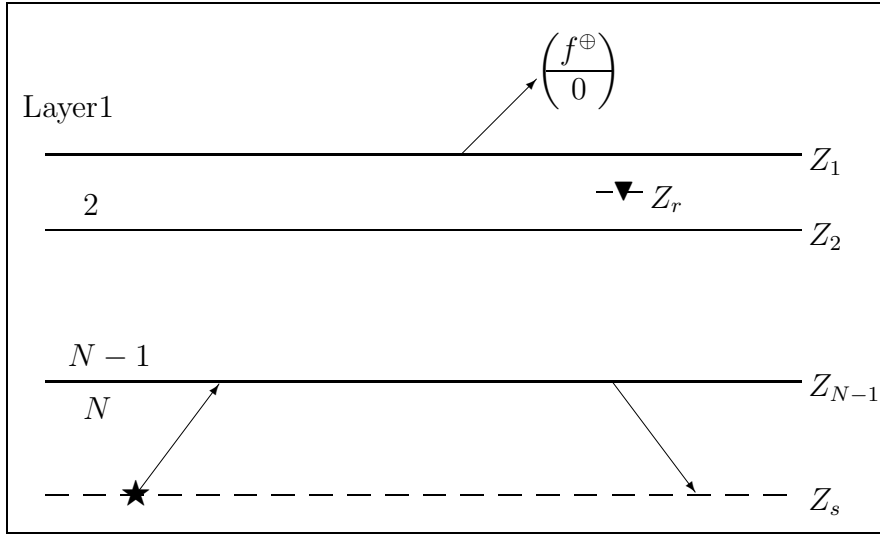
Figure 5.1: A schematic of the wavefield in a multilayered media above the source level Z_s. Note that there is only upgoing wavefield in the upper half-space.

5.2 Formulation of Reflection Coefficients

Suppose that the layer matrices for the layer 1 and 2 (Figure 5.1) are Lm_1 and Lm_2, respectively. Here, the layer 1 is a half-space and in the absence of any sources in the half-space, one can safely assume that there are no downgoing waves in this layer. Let us represent the vectors of reflection-transmission coefficients (here and in the sequel to be referred as "R-T coefficients") in the upper-half space and the layer below as $(f^\oplus \mid 0)^T$ and $(f'^\oplus \mid f'^\ominus)^T$. The superscripts $\oplus$ and $\ominus$ are for upgoing and downgoing waves, respectively. f is a vector of excitation coefficients. f and f' are excitation vectors in the layer 1 and layer 2, respectively. Since there is

no downgoing wave in the upper half space, $f^{\ominus} = 0$. Application of the continuity principle across the interface Z_1 gives:

$$Lm_1 \begin{pmatrix} f^{\oplus} \\ 0 \end{pmatrix} = Lm_2 \begin{pmatrix} f'^{\oplus} \\ f'^{\ominus} \end{pmatrix} \implies Lm_2^{-1}Lm_1 \begin{pmatrix} f^{\oplus} \\ 0 \end{pmatrix} = \begin{pmatrix} f'^{\oplus} \\ f'^{\ominus} \end{pmatrix} \qquad (5.1)$$

By denoting $K = Lm_2^{-1}Lm_1$ in a block form, the above equation can be represented as:

$$\begin{pmatrix} f'^{\oplus} \\ f'^{\ominus} \end{pmatrix} = \left(\begin{array}{c|c} K_{11} & K_{12} \\ \hline K_{21} & K_{22} \end{array} \right) \begin{pmatrix} f^{\oplus} \\ 0 \end{pmatrix} \quad \text{or,} \quad \begin{pmatrix} f'^{\oplus} \\ f'^{\ominus} \end{pmatrix} = \left(\begin{array}{c} \underbrace{K_{11}f^{\oplus}} \\ \hline \underbrace{K_{21}K_{11}^{-1}}\,\underbrace{K_{11}f^{\oplus}} \end{array} \right) \qquad (5.2)$$

Equation (5.2) has the form $(F^{\oplus} \ | \ K_r F^{\oplus})^T$ where $K_r = K_{21}K_{11}^{-1}$ and $F^{\oplus} = K_{11}f^{\oplus}$. Equation (5.2) essentially translates the wavefield across an interface.

In the next step, let us consider the wavefield propagation in a homogeneous anisotropic layer. In this case, block matrix K has the following form (see Appendix B for details):

$$\begin{pmatrix} f'^{\oplus} \\ f'^{\ominus} \end{pmatrix} = \left(\begin{array}{c|c} (E^{\oplus})^{-1} & 0 \\ \hline 0 & (E^{\ominus})^{-1} \end{array} \right) \begin{pmatrix} F^{\oplus} \\ K_r F^{\oplus} \end{pmatrix}$$

$$\text{or,} \quad \begin{pmatrix} f'^{\oplus} \\ f'^{\ominus} \end{pmatrix} = \left(\begin{array}{c} \underbrace{(E^{\oplus})^{-1}F^{\oplus}} \\ \hline \underbrace{(E^{\ominus})^{-1}K_r E^{\oplus}}\,\underbrace{(E^{\oplus})^{-1}F^{\oplus}} \end{array} \right) \qquad (5.3)$$

Once again, equation 5.3 has the form $(F^{\oplus} \mid K_r F^{\oplus})^T$ where $K_r = (E^{\ominus})^{-1} K_r E^{\oplus}$ and $F^{\oplus} = (E^{\oplus})^{-1} F^{\oplus}$.

Now let us look at the form of the wavefield in terms of R-T coefficients when it propagates through the next interface. In this case the downgoing wavefield is non-zero. Therefore,

$$
\begin{pmatrix} f'^{\oplus} \\ f'^{\ominus} \end{pmatrix} = \left(\begin{array}{c|c} K_{11} & K_{12} \\ \hline K_{21} & K_{22} \end{array} \right) \begin{pmatrix} F^{\oplus} \\ K_r F^{\oplus} \end{pmatrix}
$$

or,
$$
\begin{pmatrix} f'^{\oplus} \\ f'^{\ominus} \end{pmatrix} = \left(\begin{array}{c} \underbrace{(K_{11} + K_{12} K_r) F^{\oplus}} \\ \hline \underbrace{(K_{21} + K_{22} K_r)(K_{11} + K_{12} K_r)^{-1}} \underbrace{(K_{11} + K_{12} K_r) F^{\oplus}} \end{array} \right) \tag{5.4}
$$

This is a general form of R-T coefficients across an interface. Note that this equation is equivalent to (5.2) with $K_r = 0$. By using this equation over a loop, the wavefield across a stack of vertically inhomogeneous anisotropic layers is obtained. The form of K_r is equivalent to the frequency dependent reflection coefficients described by Kennett and Kerry (1979) and Fryer and Frazer (1984). Thus, a recursive formulation can be written for the frequency dependent reflection coefficients as:

$$
K_r^{New} = (E^{\ominus})^{-1} (K_{21} + K_{22} K_r^{old})(K_{11} + K_{12} K_r^{old})^{-1} E^{\oplus} \tag{5.5}
$$

and for the upgoing wavefield as:

$$
f_{New}^{\oplus} = (E^{\oplus})^{-1} (K_{11} + K_{12} K_r) f_{old}^{\oplus} \tag{5.6}
$$
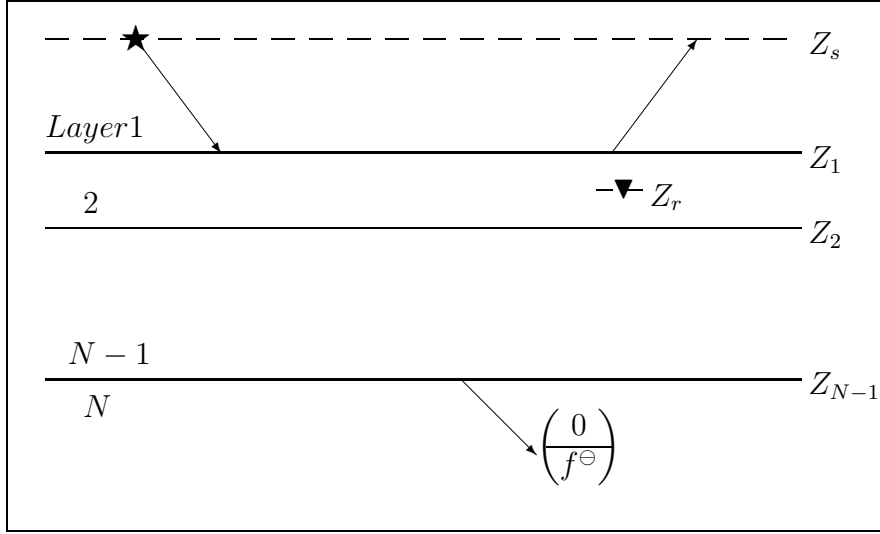
Figure 5.2: A schematic of the wavefield in a multilayered media below the source level Z_s. Note that there is only a downgoing wavefield in the lower half-space.

So far, the formulation was obtained for wave propagation in a multilayered stack above the source level. Now, let us look at the multilayered anisotropic media below the source level as shown in Figure 5.2. An equation similar to 5.1 can be written for the lower set of layers. The Nth layer is a half-space and there is no upgoing wavefield in this layer. Therefore,

$$\begin{pmatrix} f'^{\oplus} \\ \hline f'^{\ominus} \end{pmatrix} = \begin{pmatrix} K_{11} & K_{12} \\ \hline K_{21} & K_{22} \end{pmatrix} \begin{pmatrix} 0 \\ f^{\ominus} \end{pmatrix} \quad \text{or,} \quad \begin{pmatrix} f'^{\oplus} \\ \hline f'^{\ominus} \end{pmatrix} = \begin{pmatrix} \underbrace{K_{12}K_{22}^{-1}}\underbrace{K_{22}f^{\ominus}} \\ \hline \underbrace{K_{22}f^{\ominus}} \end{pmatrix} \quad (5.7)$$

where the block matrix $K = Lm_{N-1}^{-1}Lm_N$. Equation (5.7) has the form $(K_t f^{\ominus} \mid f^{\ominus})^T$ where $K_t = K_{12}K_{22}^{-1}$ and $f'^{\ominus} = K_{22}f^{\ominus}$.

For the wavefield propagation in a homogeneous anisotropic layer, the block matrix K has the following form:

$$\left(\frac{f'^{\oplus}}{f'^{\ominus}} \right) = \left(\begin{array}{c|c} (E^{\oplus}) & 0 \\ \hline 0 & (E^{\ominus}) \end{array} \right) \left(\frac{K_t F^{\ominus}}{F^{\ominus}} \right)$$

$$\text{or,} \quad \left(\frac{f'^{\oplus}}{f'^{\ominus}} \right) = \left(\frac{\underbrace{(E^{\oplus})K_t E^{\ominus})^{-1}}\,\underbrace{E^{\ominus}F^{\ominus}}}{\underbrace{(E^{\ominus})F^{\ominus}}} \right) \tag{5.8}$$

Once again, the above equation 5.8 has the form $(K_t f'^{\ominus} \quad | \quad f'^{\ominus})^T$ where $K_t = (E^{\oplus})K_t(E^{\ominus})^{-1}$ and $f'^{\ominus} = (E^{\ominus})f^{\oplus}$.

$$\left(\frac{f'^{\oplus}}{f'^{\ominus}} \right) = \left(\begin{array}{c|c} K_{11} & K_{12} \\ \hline K_{21} & K_{22} \end{array} \right) \left(\frac{K_t F^{\ominus}}{F^{\ominus}} \right)$$

$$\text{or,} \quad \left(\frac{f'^{\oplus}}{f'^{\ominus}} \right) = \left(\frac{\underbrace{(K_{11}K_t + K_{12})(K_{21}K_t + K_{22})^{-1}}\,\underbrace{(K_{21}K_t + K_{22})F^{\ominus}}}{\underbrace{(K_{21}K_t + K_{22})F^{\ominus}}} \right) \tag{5.9}$$

Thus, a recursive formulation can be written for the transmission matrices K_t as:

$$K_t^{New} = E^{\oplus}(K_{11}K_t^{old} + K_{12})(K_{21}K_t^{old} + K_{22})^{-1}(E^{\ominus})^{-1} \tag{5.10}$$

and for the downgoing wavefield as:

$$f_{New}^{\ominus} = E^{\ominus}(K_{21}K_t + K_{22})f_{old}^{\ominus} \tag{5.11}$$

46

Thus, in this section a method is developed to propagate the wavefields from one layer to another recursively. This formulation also avoids any growing exponentials due to the large thickness of a layer.

5.3   Introduction of Source Field

Let us assume that $(g^{\oplus} \mid 0)^T$ and $(0 \mid g^{\ominus})^T$ are the vectors of excitation coefficients due to the source in a homogeneous layer, evaluated just above and just under the source depth level, respectively. Furthermore, let us assume that the lower set and upper set of layered media contribute to $f^{\oplus}$ and $f^{\ominus}$, respectively, in the upgoing and downgoing fields at the source depth level. Thus,

$$f^{\ominus} = K_r(g^{\oplus} + f^{\oplus})$$

$$f^{\oplus} = K_t(g^{\ominus} + f^{\ominus}) \tag{5.12}$$

The above set of equations (5.12) can be solved to obtain the upgoing and downgoing wavefield in terms of the source excitation vector as follows:

$$f^{\oplus} = K_t g^{\ominus} + K_t(K_r g^{\oplus} + K_r f^{\oplus})$$

$$\text{or,} \qquad (I - K_t K_r)f^{\oplus} = K_t g^{\ominus} + K_t K_r g^{\oplus}$$

$$\text{or,} \qquad f^{\oplus} = (I - K_t K_r)^{-1}(K_t K_r g^{\oplus} + K_t g^{\ominus})$$

$$\text{or,} \qquad f^{\oplus} = A_1 g^{\oplus} + B_1 g^{\ominus} \tag{5.13}$$

where

$$A_1 = (I - K_t K_r)^{-1} K_t K_r \text{ and } B_1 = (I - K_t K_r)^{-1} K_t$$

47

Similarly,

$$f^\ominus = K_r g^\oplus + K_r(K_t g^\ominus + K_t f^\ominus)$$

or, $$(I - K_r K_t)f^\ominus = K_r g^\oplus + K_r K_t g^\ominus$$

or, $$f^\ominus = (I - K_r K_t)^{-1}(K_r g^\oplus + K_r K_t g^\ominus)$$

or, $$f^\ominus = A_2 g^\oplus + B_2 g^\ominus \qquad (5.14)$$

where

$$A_2 = (I - K_r K_t)^{-1} K_r \text{ and } B_2 = (I - K_t K_r)^{-1} K_r K_t$$

Thus, the total wavefield R-T coefficients at the source level can be written as:

$$\begin{pmatrix} g^\oplus \\ 0 \end{pmatrix} + \begin{pmatrix} f^\oplus \\ f^\ominus \end{pmatrix} = \begin{pmatrix} (\mathbf{I} + A_1)g^\oplus + B_1 g^\ominus \\ A_2 g^\oplus + B_2 g^\ominus \end{pmatrix} \qquad (5.15)$$

just above the source level, and,

$$\begin{pmatrix} 0 \\ g^\ominus \end{pmatrix} + \begin{pmatrix} f^\oplus \\ f^\ominus \end{pmatrix} = \begin{pmatrix} A_1 g^\oplus + B_1 g^\ominus \\ A_2 g^\oplus + (\mathbf{I} + B_2)g^\ominus \end{pmatrix} \qquad (5.16)$$

just below the source level.

5.4 Wavefield at Receivers

Equations (5.6) and (5.11) can be utilized to find the wavefields at the receivers. The R-T coefficients just above the source level is related to the R-T coefficients above the surface as:

$$g^{\oplus} + f^{\oplus} = G^{\oplus} = P_s P_{N-1} \cdots \cdots P_3 P_2 P_r P_1 f^{\oplus} \tag{5.17}$$

where $P = (E^{\oplus})^{-1}(K_{11} + K_{12}K_r)$ and $G^{\oplus} = (\mathbf{I} + A_1)g^{\oplus} + B_1 g^{\ominus}$. The subscripts of P denote interfaces (1,2,..), receiver(r) and source(s) levels. In equation (5.17) $f^{\oplus}$ is unknown. Therefore,

$$f^{\oplus} = P_1^{-1} P_r^{-1} P_2^{-1} P_3^{-1} \cdots \cdots P_{N-1}^{-1} P_s^{-1} G^{\oplus} \tag{5.18}$$

Using the above equation (5.18), the wavefields at the receivers above the source level can be written in the following form:

$$f_r^{\oplus} = P_r^{-1} \cdots \cdots P_{N-1}^{-1} P_s^{-1} G^{\oplus} \tag{5.19}$$

Similarly, for the receivers below the source, one can rewrite equation (5.19) as:

$$f_r^{\ominus} = Q_r^{-1} \cdots \cdots Q_{N-1}^{-1} Q_s^{-1} G^{\ominus} \tag{5.20}$$

where $Q = (E^{\ominus})(K_{21}K_t + K_{22})$ and $G^{\ominus} = (\mathbf{I} + A_2)g^{\oplus} + B_2 g^{\ominus}$.

5.5 Examples: Reflection Coefficient and Phase

In this dissertation, the reflection coefficient is considered as the amplitude of a reflected wave relative to an incident wave. The variation of the reflection coefficient with angle (or offset) and azimuth is the basis of the AVOAz analysis. In this section, the reflection coefficients for various models are examined to show the effects of:

1. *type of anisotropy* – The reflection coefficients are computed at the interface of two half-spaces - both of them are either isotropic or vertical transversely isotropic (VTI) or orthorhombic.

2. *rotation of symmetry axis in a transversely isotropic (TI) medium* – In this case, the reflection coefficients are computed at the interface of two TI half-spaces. In the upper half-space, the symmetry is kept vertical while the symmetry axis in the lower half-space is gradually rotated from 0 to 90 degrees (i.e. from vertical to horizontal).

3. *frequency of the incident wave and thickness of the layers*– A model consisting of a VTI layer sandwiched between two VTI half-spaces is considered. Frequency and thickness dependent reflection coefficients are examined.

5.5.1 Isotropic, VTI and Orthorhombic half spaces

An isotropic medium is characterized by two independent elastic constants and has constant P and S wave velocities throughout the medium. In isotropic media, both vertically and horizontally polarized shear waves (SV and SH, respectively) have the same velocities. In the case of a horizontal interface between two isotropic media, the

SV-wave is polarized in the plane perpendicular to the interface and the SH-wave is polarized parallel to the interface. Figure 5.3a shows the reflection coefficients (solid line) and phase change (dashed line) for the reflected P- (blue color) and SV- (black color) waves for an incident P-wave. Incident waves are represented by a down-arrow (e.g $P^{\downarrow}$) and reflected waves are represented by an up-arrow (e.g $P^{\uparrow}$). The elastic constants for the upper and the lower isotropic half-spaces are given in Table 5.1. Since the P- and SV-waves are decoupled from the SH wave in an isotropic medium, there are only P- and SV-waves reflected from the incident P-wave. Similarly, for an incident SV-wave, there are only P- and SV-waves reflected. However, for an incident SH-wave, only the SH-wave will be reflected (see Figure C.1 in Appendix C). The point of discontinuities on the curves of reflection coefficient versus angle of incidence can be due to two reasons: (1) Critical angle of incidence for the incident and reflected wave type; and, (2) change of phase of the reflected wave. The angle of incidence is measured from the normal to the interface.

A transversely isotropic (TI) medium has five independent elastic constants. When the axis of symmetry is vertical, the transversely isotropic medium is called a vertically transverse isotropic (VTI) medium. For a horizontal interface between two VTI media, the reflection coefficient for a given angle of incidence does not vary with azimuth. The angular dependence of reflection coefficients for the incident P-wave at a horizontal interface between two VTI half-spaces are shown in Figure 5.3b. The elastic coefficients for the two VTI half-spaces are given in Table 5.1. Note that because of the symmetry, the SH-wave is decoupled from the P-SV waves and therefore, there are only P- and SV-waves reflected from an incident P-wave. The

reflection coefficients for incident shear waves and reflected longitudinal and shear waves are given in Appendix C (see Figure C.2).

Cs	Upper Half-space			Lower Half-space		
	Orthorhombic	VTI	Isotropic	Orthorhombic	VTI	Isotropic
C_{11}	19.49	20.35	19.38	47.49	52.77	49.04
C_{22}	21.22	20.35	19.38	58.05	52.77	49.04
C_{33}	17.44	17.44	19.38	41.57	41.57	49.04
C_{44}	5.32	4.73	5.18	15.27	11.86	11.13
C_{55}	4.14	4.73	5.18	8.46	11.86	11.13
C_{66}	6.07	6.07	5.18	9.66	9.66	11.13
C_{12}	3.01	8.21	9.02	16.0	33.45	26.78
C_{13}	6.39	6.63	9.02	12.65	13.7	26.78
C_{23}	6.88	6.63	9.02	14.75	13.7	26.78
ρ	2.34	2.34	2.34	2.37	2.37	2.37

Table 5.1: Elastic coefficients and densities for the upper and lower half-spaces in isotropic, VTI and orthorhombic media. There are nine independent elastic constants in the orthorhombic media, five in VTI and two in the isotropic media. The elastic constants for the VTI and isotropic media are calculated by averaging the elastic constants of the orthorhombic media. All the elastic coefficients are in GPa unit and the densities are in gm/cc.

There are nine independent elastic constants for an orthorhombic medium. In this case, the three wave types are coupled and there are no pure vertically or horizontally polarized shear waves. Therefore, the two shear waves are denoted as S1 and S2. Unlike the reflection coefficients as discussed above for the isotropic and VTI media, the reflection coefficients at the interface between two orthorhombic media vary azimuthally. Figures 5.4a, b and c show azimuthal variation of the reflection coefficients of the reflected P, S1 and S2 waves, respectively, from an incident P-wave. The solid and dashed curves are colored according to their azimuths shown at the top of each graph in Figure 5.4. Note that for an incident P wave, all three wave types are reflected. Similarly, for incident S1 and S2 waves, all three wave types are

reflected (see Figures C.3 and C.4 in Appendix C). The elastic constants for the
orthorhombic upper and lower half-spaces are given in Table 5.1.
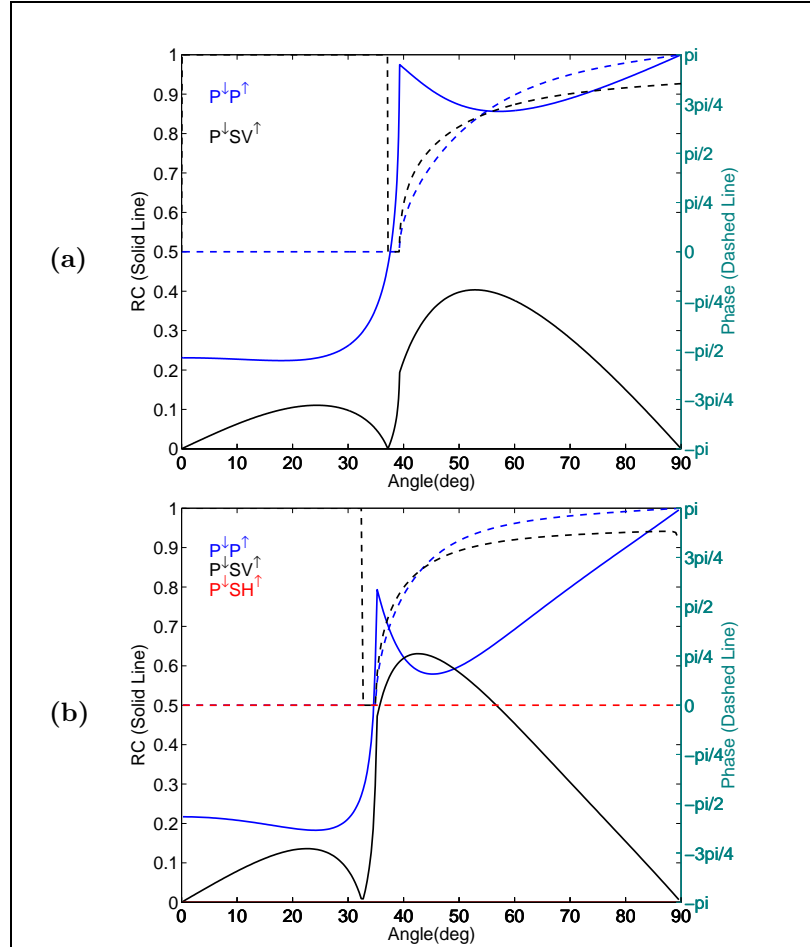
Figure 5.3: Reflection coefficients (solid line) and phase change (dashed line) for
the reflected P- and S-waves from an incident P-wave at the boundary between two
half spaces: (a) isotropic media (b) VTI media. The elastic coefficients used for the
computation are given in Table 5.1.
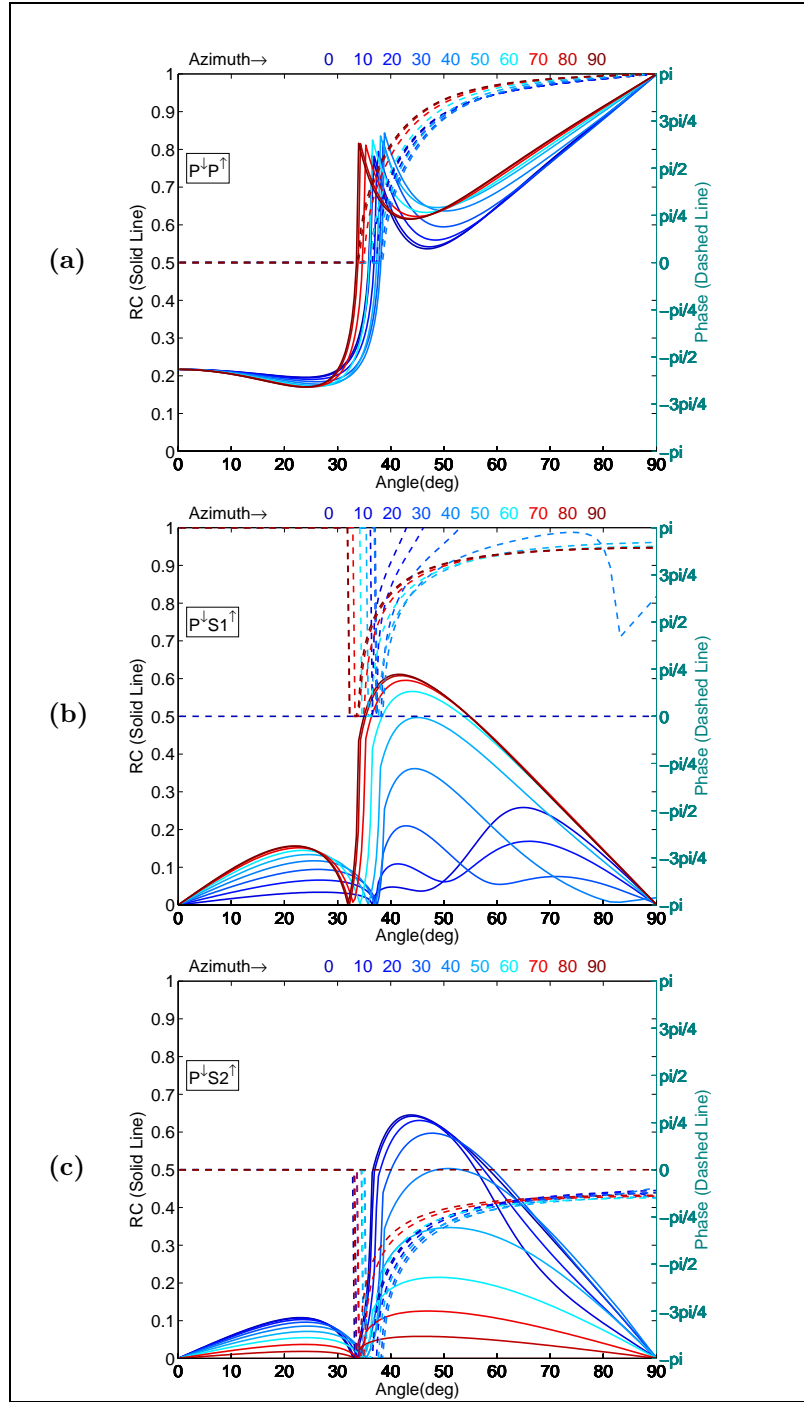
Figure 5.4: Reflection coefficients and phase change at the boundary between two orthorhombic half-spaces. The elastic constants for the two half-spaces are given in Table 5.1. The reflection coefficients are computed for an incident P-wave and the reflected (a) P (b) S1 and (c) S2 wave types. The curves are colored according to the azimuthal variation of the reflection coefficients.

5.5.2 Rotation of Symmetry axis in a TI medium

In the previous section, a model with two VTI half-spaces was considered. In other words, both half-spaces had a vertical axis of symmetry. However, in a geologically realistic situation two transversely isotropic media (e.g. shales) across an interface may not have a vertical axis of symmetry, for example, across an unconformity plane. Modeling in this section, therefore, is carried out to study the effects of tilt in the symmetry axis on the reflection coefficients. As shown in Figure 5.5 the two half-spaces are transversely isotropic. The upper half-space has a vertical axis of symmetry while the symmetry axis in the lower half-space is gradually rotated from the vertical to the horizontal (i.e. from VTI to HTI). The set of five independent elastic constants and density for each half-space are given in Table 5.2.
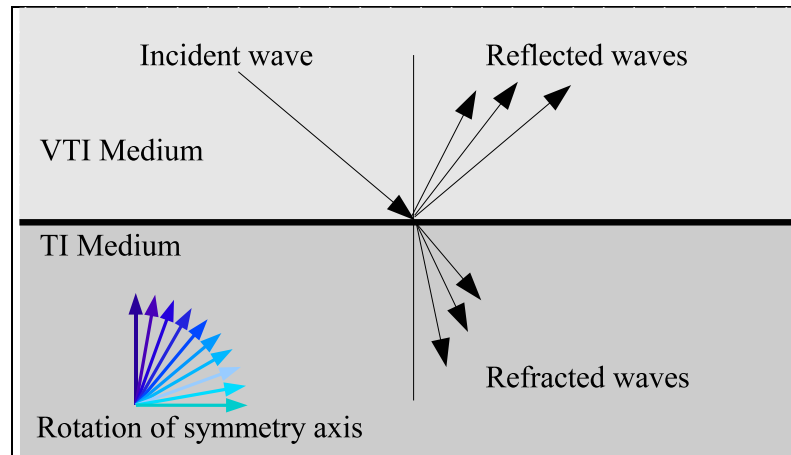
Figure 5.5: A schematic diagram showing two VTI half-spaces. In the lower half-space, the vertical axis of symmetry is rotated from 0 to 90 degrees.

The reflection coefficients are computed in the vertical plane containing the symmetry axes of both half-spaces. Figure 5.6 shows the reflection coefficients of the reflected P and S2 wave types from an incident P-wave. The reflection coefficients

and phase change are colored according to the rotation (or tilt) angle of the symmetry axis from the vertical. The PP reflection coefficients for normal incidence vary considerably due to tilt and also AVO behavior for PP reflection changes at the interface. The reflection coefficients of P, S1 and S2 wave types from the incident S1 and S2 waves are included in Appendix C(Figure C.5). Here S1 and S2 are shear waves polarized in the horizontal and the vertical plane, respectively (or, SH and SV waves, respectively) at least in the vertical plane containing the symmetry axes of both half-spaces. Note that in this vertical plane, S1 and S2 waves are decoupled and therefore, there is no S1-wave reflected from the incident P-wave in this plane.

Cs	Up. Half Space	Lr. Half Space
C_{11}	21.26	59.4
C_{33}	17.63	42.42
C_{44}	5.32	15.27
C_{66}	8.99	19.7
C_{13}	6.97	15.82
ρ	2.34	2.37

Table 5.2: VTI elastic coefficients (in GPa) and density (gm/cc) used in the model Figure 5.5

Figure 5.6: Reflection coefficients and phase change for the reflected (a)P-wave (b) S2 (SV)-wave from an incident P-wave in the plane containing the symmetry axes of both half-spaces. The color index for each graph is shown at the top.

5.5.3 Frequency dependent reflection coefficients: A VTI layer between two VTI half spaces
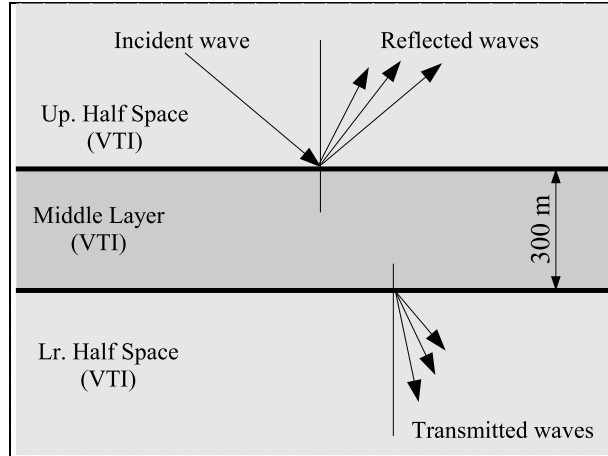
Figure 5.7: A schematic diagram showing a VTI layer sandwiched between two VTI half-spaces. The reflection coefficients are computed at the upper interface.

Cs	Up. Half Space	Middle Layer	Lr. Half Space
C_{11}	59.4	21.26	59.4
C_{33}	42.42	17.63	42.42
C_{44}	15.27	15.32	15.27
C_{66}	19.7	8.99	19.7
C_{13}	15.82	6.97	15.82
ρ	2.37	2.34	2.37

Table 5.3: VTI elastic coefficients (in GPa) and density (in gm/cc) used to compute the reflection coefficients in the model Figure 5.7.

A layer of finite thickness in a multilayer medium acts as a scatterer, thus, making the reflection coefficients frequency dependent. The frequencies ω which parameterize the reflection coefficients from a multilayered stack as the whole, are from the formula of monochromatic plane wave. The model shown in Figure 5.7 has a VTI layer sandwiched between two VTI half-spaces of same elastic constants. The elastic

constants and densities of the layers are given in Table 5.3. This model is investigated with the frequency ranging from 10 to 50 Hz and the reflection coefficients for the reflected P and S2 (SV) waves an incident P wave are plotted in Figure 5.8. Since both the half-spaces are VTI with their symmetry axes perpendicular to the interface, there is no reflected S1 (SH) wave from the incident P-wave. The reflection coefficients and phase are colored by frequencies. Notice the change in PP reflection coefficients with the change in frequency. If the dominant frequency of investigation changes, the behavior of reflection coefficients with angle will change. Thus, it is important to include frequency effect in AVO interpretations. The reflection coefficients for incident shear waves and the reflected P, S1 and S2 waves for this model are included in Appendix C (Figure C.6).
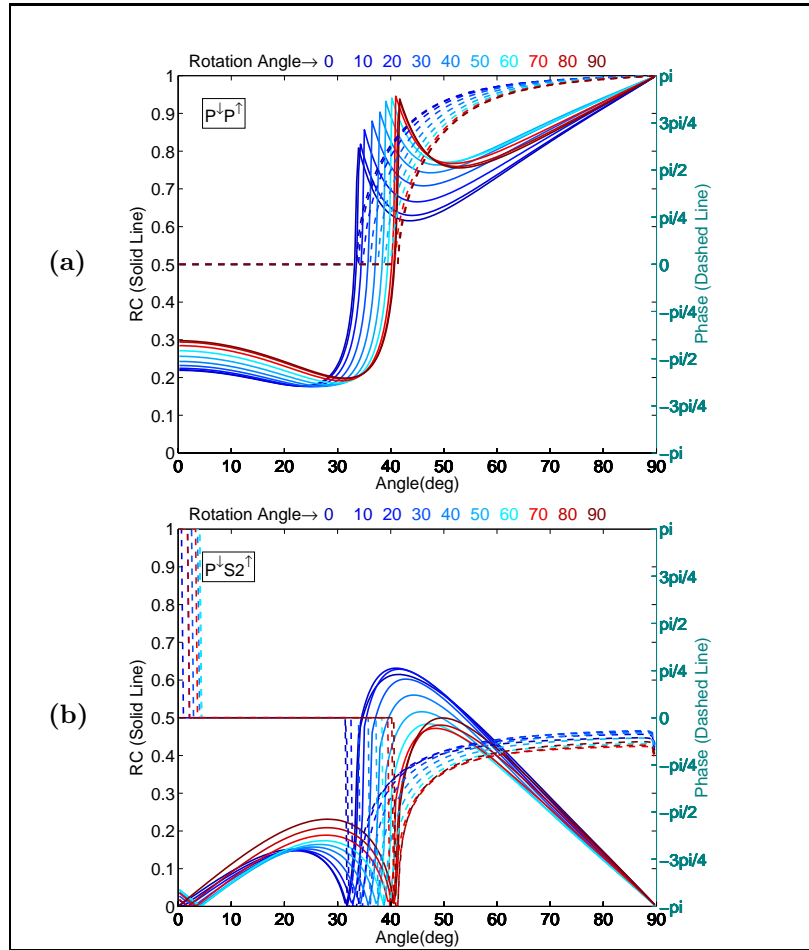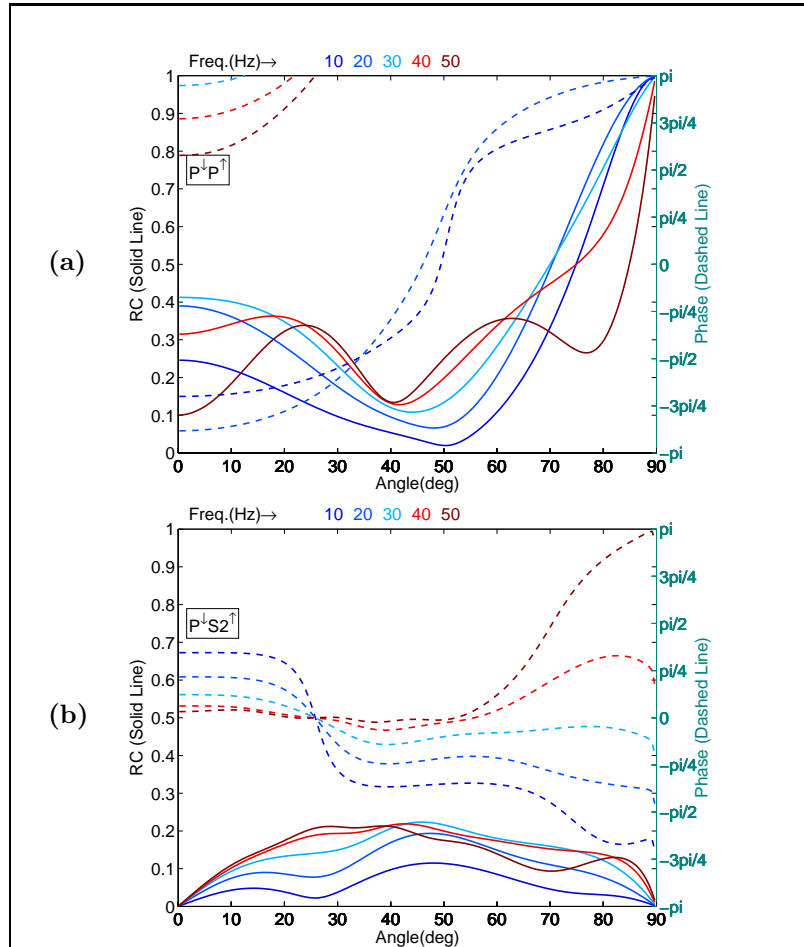
Figure 5.8: Reflection coefficient and phase for the reflected (a)P-wave and (b) S2-wave from an incident P-wave in the frequency range of 10 to 50Hz. The elastic coefficients for this calculation is given in Table 5.3.

5.5.4 Effect of thickness on reflection coefficients

In this section, effects of the thickness variation on the reflection coefficients are analyzed. The model used for computation is similar to the model (Figure 5.7) used in the previous section, i.e. a VTI layer sandwiched between two VTI half spaces. The thickness of the sandwiched layer is varied from 210 to 300 m. The elastic coefficients and densities for the model are given in Table 5.3. The reflection coefficients are computed at 10Hz frequency for the reflected P and S2 (SV) waves from an incident P-wave as shown in Figure 5.9. Note that there is no S1 (SH) wave reflected for the incident P-wave in this model. It is evident from the plots that the thickness of a layer affects the reflection coefficients. Thus, AVO interpretation can be affected. Therefore, it is important to consider thickness variation in our models and compute reflection coefficients using exact formulations. In the case of incident shear waves, the reflection coefficients for P, S1 and S2 waves are included in Appendix C (Figure C.7).

5.6 Summary

The seismic wave propagation in a multilayered medium is explained in a simplistic manner, thus avoiding too involved analytical derivations. The reflection coefficients and associated phase are readily computed at an interface in a multilayered medium. Various models are investigated for reflection coefficient variation with incidence angle. It is evident from these models that AVO interpretation may not yield desired results without due regard for the anisotropy of the study medium and frequency characteristics of the incident wavefield.
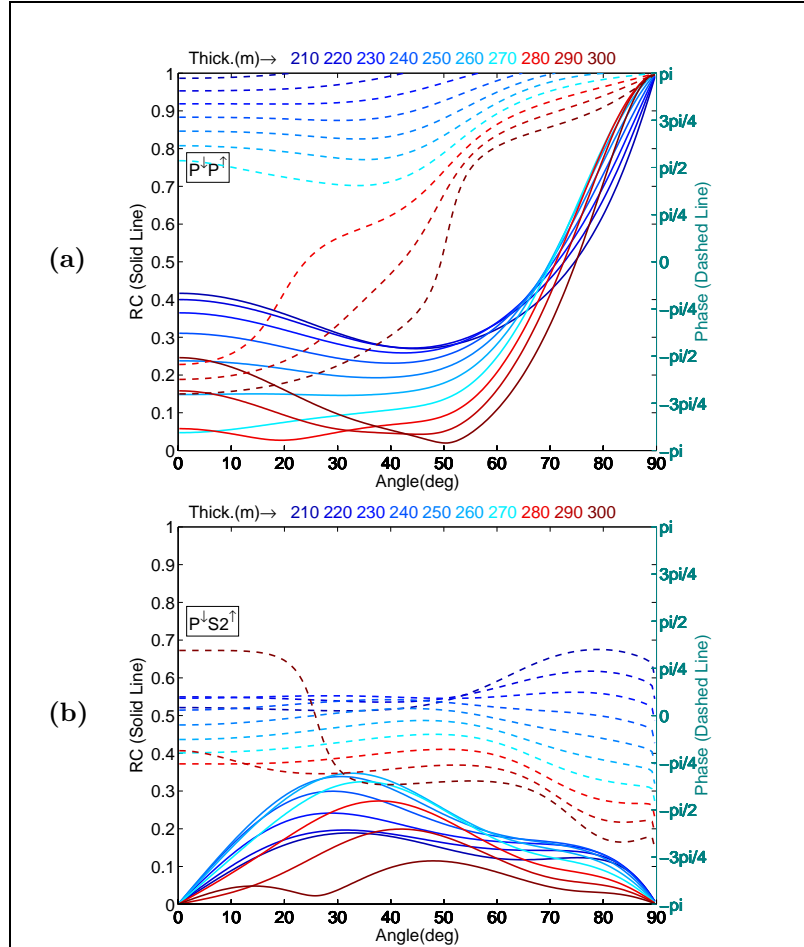
Figure 5.9: Reflection coefficient and phase for an incident P-wave and the reflected (a) P-wave (b) S2-wave. Thickness of the sandwiched layer varies from 210 to 300 m. The reflection coefficient and phase curves are colored according to the thickness of the sandwiched layer. The elastic coefficients and densities for this model are given in Table 5.3.

Chapter 6

Fractured Media

6.1 Introduction

This chapter investigates the effects of multiple sets of fractures on reflection coefficients and velocity anisotropy. Natural fractures or hydraulic fracturing of shales changes the anisotropy pattern in shales. Whether there is a single set or multiple sets of preferentially oriented fractures, the fracturing of shales changes its initial anisotropy behavior. In the simplest case, a single set of vertical fractures in a VTI shale turns the medium into an orthorhombic medium where azimuthal velocity anisotropy is also observed. Therefore, in order to understand the response of multiple stages of fracturing in shales, it is important to model velocity anisotropy and reflection coefficients for various wave types, especially when multi-component surface seismic data is becoming available.

Hydraulically induced fractures in shales from micro-seismic and surface seismic point of views are now extensively being investigated (Lynn, 2004; Searcy et al., 2005; Browning, 2006). Chen (2000) looked at amplitude versus offset (AVO) aspects of fractured models (2 sets of vertical fractures) and limits his analysis in terms of angles

up to 45 degrees. Being simple in its essence, Schoenberg and Sayers' (1995) method is often used within the framework of its limitations to model multiple fractures in exploration seismic.

In the first section of this chapter, a detailed mathematical formulation is shown in order to compute effective elastic constants in a medium with multiple sets of fractures. Then, in the next section, a few models are considered to show velocity variation of each type in the fractured media. These models are generated by adding identical vertical fracture sets at various angles assuming that these fractures are non-interacting. Furthermore, effects of fractures on reflection coefficient variations with angles and azimuth (and hence AVOAz) are investigated at the interface between two anisotropic half-spaces. In the models, it is assumed that induced fractures in a VTI medium are contained within the lower half-space and are not propagating in the VTI layer above the interface.

6.2   Effective Elastic Constants in Fractured Media

The assumptions in the formulation of effective elastic constants for fractured media are as follows:

- Interaction between fractures is negligible and therefore, excess compliance due to fractures is additive.

- Density of the resultant medium does not change due to fractures.

- Fractures are parallel to each other in a fracture set.

- Fractures are in the long wavelength limit, i.e. fracture spacing is much smaller compared to the wavelength of investigation.

The resultant strain ϵ_{ij} due to applied stress σ_{ij} over a representative volume V containing fractures can be written as:

$$
\begin{aligned}
\epsilon_{ij} &= \epsilon_{ij}^M + \epsilon_{ij}^C \\
&= S_{ijkl}^M \sigma_{kl} + \frac{1}{V} \int \frac{1}{2} \left(\frac{\delta_i}{x_j} + \frac{\delta_j}{x_i} \right) dV \\
&= S_{ijkl}^M \sigma_{kl} + \frac{1}{2V} \int (\delta_i n_j + \delta_j n_i) \frac{dV}{A}
\end{aligned}
\tag{6.1}
$$

where superscripts M and C denote background media and cracks, respectively. The compliance tensor is denoted by S_{ijkl}, and $A = x_i \cdot n_i$ represents the aperture of the fractures.

Excess strain due to N penny shaped cracks with diameter D_k and aperture A_k can be expressed as:

$$
\epsilon_{ij}^C = \frac{1}{2V} \sum_{m=1}^{N} (\delta_i n_j^m + \delta_j n_i^m) \left(\frac{\pi D_m^2}{4} \right)
\tag{6.2}
$$

Oda et al. (1984) assumed that the displacement discontinuity is proportional to the traction applied. i.e.

$$
\delta_i = K_0 D \sigma_{ij} n_j
\tag{6.3}
$$

where the constant of proportionality is assumed to be proportional to the diameter D of the cracks, and the proportionality constant K_0 can be dependent on pressure (stress).

By substituting 6.3 into 6.2, one obtains:

$$
\begin{aligned}
\epsilon_{ij}^C &= \frac{1}{2V} \sum_{m=1}^{N} \left(K_0^m D_m \sigma_{il} n_l^m n_j^m + K_0^m D_m \sigma_{jl} n_l^m n_i^m \right) \left(\frac{\pi D_m^2}{4} \right) \\
&= \frac{1}{2} \sum_{m=1}^{N} \frac{K_0^m \pi D_m^3}{4V} \left(n_l^m n_j^m \sigma_{il} + n_l^m n_i^m \sigma_{jl} \right) \\
&= \frac{1}{4} \sum_{m=1}^{N} \frac{K_0^m \pi D_m^3}{4V} \left(\delta_{ik} n_l^m n_j^m + \delta_{jk} n_l^m n_i^m + \delta_{il} n_k^m n_j^m + \delta_{jl} n_k^m n_i^m \right) \sigma_{kl} \\
&= \frac{1}{4} \sum_{m=1}^{N} K_0^m \xi_m \left(\delta_{ik} n_l^m n_j^m + \delta_{jk} n_l^m n_i^m + \delta_{il} n_k^m n_j^m + \delta_{jl} n_k^m n_i^m \right) \sigma_{kl} \quad (6.4)
\end{aligned}
$$

where $\xi_m = \pi D_m^3 / 4V$ is called fracture density. Equation 6.4 describes scalar cracks as K_0 is the same in all directions.

By introducing a stress-dependent proportionality tensor K_{ij} instead of constant K_0, one can rewrite equation 6.3 as:

$$
\delta_i = K_{ij} D \sigma_{jk} n_k \quad (6.5)
$$

Thus, equation 6.2 can be expanded as:

$$
\epsilon_{ij}^C = \frac{1}{4} \sum_{m=1}^{N} \xi_m \left(K_{ik}^m n_l^m n_j^m + K_{jk}^m n_l^m n_i^m + K_{il}^m n_k^m n_j^m + K_{jl}^m n_k^m n_i^m \right) \sigma_{kl} \quad (6.6)
$$

Schoenberg and Sayers (1995) used the product $Z_{ij} = K_{ij}\xi$ as a fracture system compliance tensor, which is similar to the crack compliance tensor used by Kachanov (1992). If the crack compliance is denoted by S_{ijkl}^C, the extra strain as a result of a fracture can be written as:

$$
\epsilon_{ij}^C = S_{ijkl}^C \sigma_{kl} \quad (6.7)
$$

Comparing equations 6.7 and 6.6, one can write the crack compliance tensor in the following form:

$$S^C_{ijkl} = \frac{1}{4}\xi\left(K_{ik}n_l n_j + K_{jk}n_l n_i + K_{il}n_k n_j + K_{jl}n_k n_i\right) \qquad (6.8)$$

6.3   Models: Multiple sets of vertical fractures
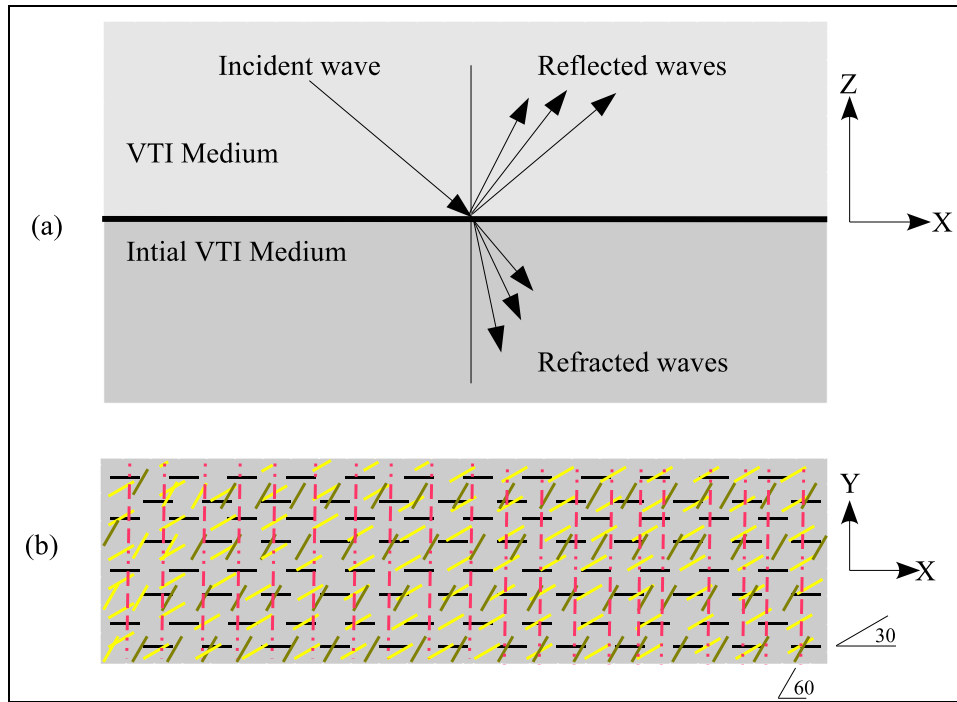
Figure 6.1: (a) A schematic diagram showing two VTI half spaces. Vertical fractures are introduced in the lower half space at 0, 30, 60 and 90 degrees as shown schematically in (b).

Elastic coefficients for the VTI half spaces used in the model Figure 6.1 are given in Table 5.1. Initially VTI medium in the lower half space is fractured vertically by gradually increasing the fracture sets at angles of 0, 30, 60 and 90 degrees with the

X-axis direction. The modeling here does not mean that a rock fractures at these angles in succession. These fracture sets are considered entirely from a numerical point of view to understand the anisotropic effects of multiple fracture sets. In another model only two fracture sets are considered: one at a 0 degree angle and another at a 90 degree angle. All fractures have an identical compliance tensor Z_{ij}, and its diagonal elements are $[0.01, 0.125, 0.125]$ and non-diagonal elements are zero.

Five fracture models are generated for anisotropy analysis and are tabulated below.

Model	No. of fracture sets	Orientations	Associated figures
1	1	0^0	(a) in 6.2 - 6.6 and D.1 - D.6
2	2	0^0 and 30^0	(b) in 6.2 - 6.6 and D.1 - D.6
3	3	0^0, 30^0 and 60^0	(c) in 6.2 - 6.6 and D.1 - D.6
4	4	0^0, 30^0, 60^0 and 90^0	(d) in 6.2 - 6.6 and D.1 - D.6
5	2	0^0 and 90^0	(e) in 6.2 - 6.6 and D.1 - D.6

Table 6.1: Table of fracture models and associated figures

When there is azimuthal variation in velocity behavior, it is difficult to quantify the amount of anisotropy and compare various models. However, one can visually compare the range of velocity variation and pattern of azimuthal variation. Although there is not much change in the range of velocity variation, there is noticeable difference in the azimuthal pattern of P and S velocity curves (Figures 6.2 and 6.3). The curves are colored according to the azimuths, and the color index is given at the top of each figure. Maximum azimuthal anisotropy is observed in the horizontal plane (i.e. along 90 degree angle in the plots). Azimuthal velocity behavior becomes more symmetrical as the number of fracture sets increases. Note that some azimuthal

velocity curves overlap each other. When two curves overlap each other, the over-lapping curve is plotted by a dotted dash line so that one can see the underlying curve as well. Thus, by comparing P and S waves velocity behavior, it is clear that anisotropy decreases as the number of fracture sets increases.

Change in reflection coefficients with angle and azimuth is often referred to as AVOAz (Amplitude Variation with Offset and Azimuth). The reflection coefficients for an incident P-wave and the reflected P, S1 and S2 are shown in Figures 6.4, 6.5, and 6.6, respectively. Comparison of the reflection coefficients and phase from all models shows that the critical angle for PP reflection increases as the reservoir becomes increasingly fractured (Figure 6.4). This suggests that the AVOAz study has the potential to discriminate between highly fractured reservoir and less frac-tured reservoir. It is cautioned here that this result may not be true for all models. Furthermore, reflection coefficients are frequency and thickness dependent, as dis-cussed in the previous chapter. Therefore, detailed modeling should be performed for the case at hand. Also note that the converted S-waves change more rapidly with offset (i.e. angle) and azimuth (Figures 6.5 and 6.6). For incident shear waves, the reflection coefficients for P, S1 and S2 waves are included in Appendix D. Thus, use of shear waves and converted waves also has potential in fracture detection.
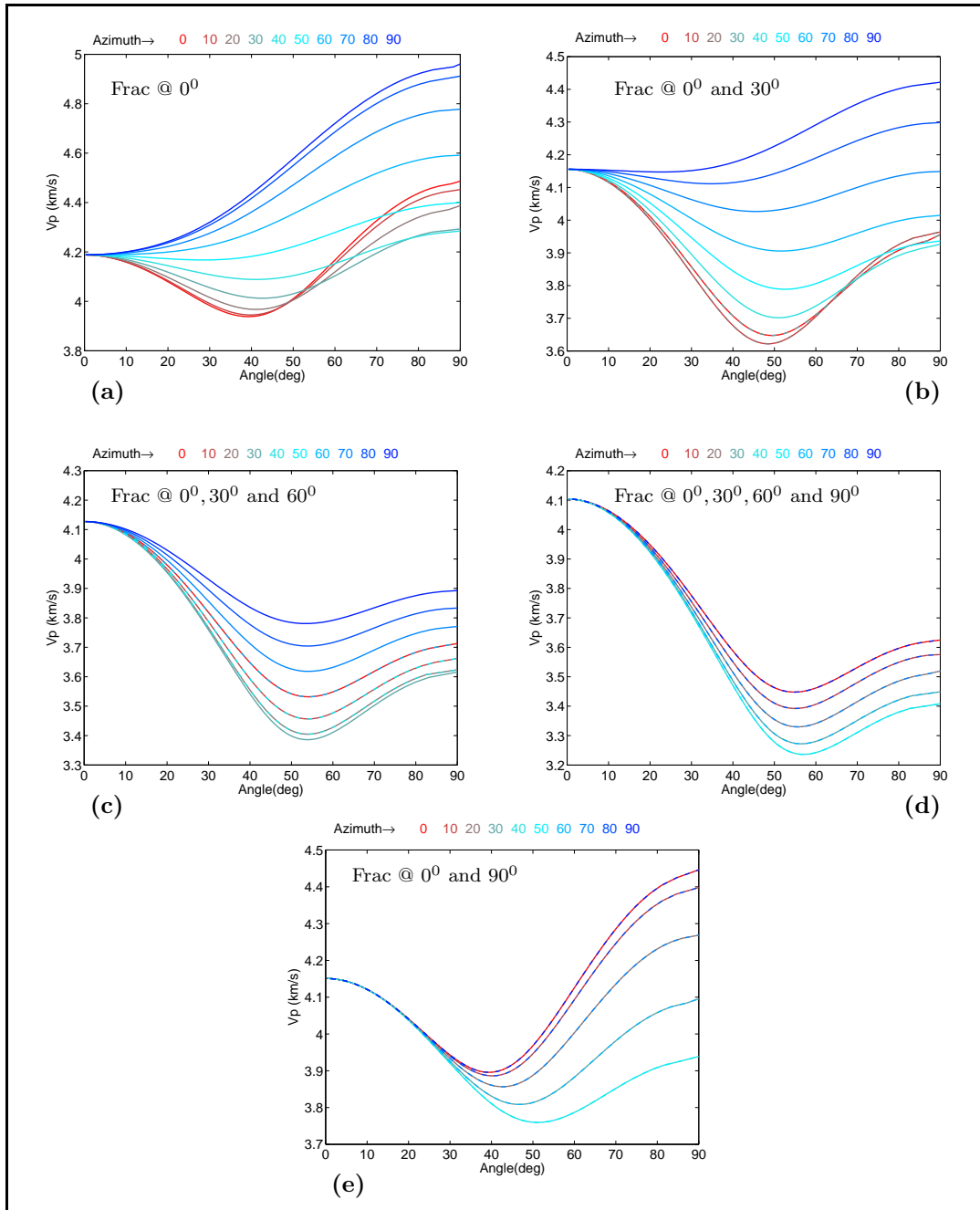
Figure 6.2: P-wave velocity anisotropy for the five fracture models. The curves are colored according to the azimuths from 0 to 90 degrees. Only overlapping curves are plotted by dotted dash lines to show the underlying curves.
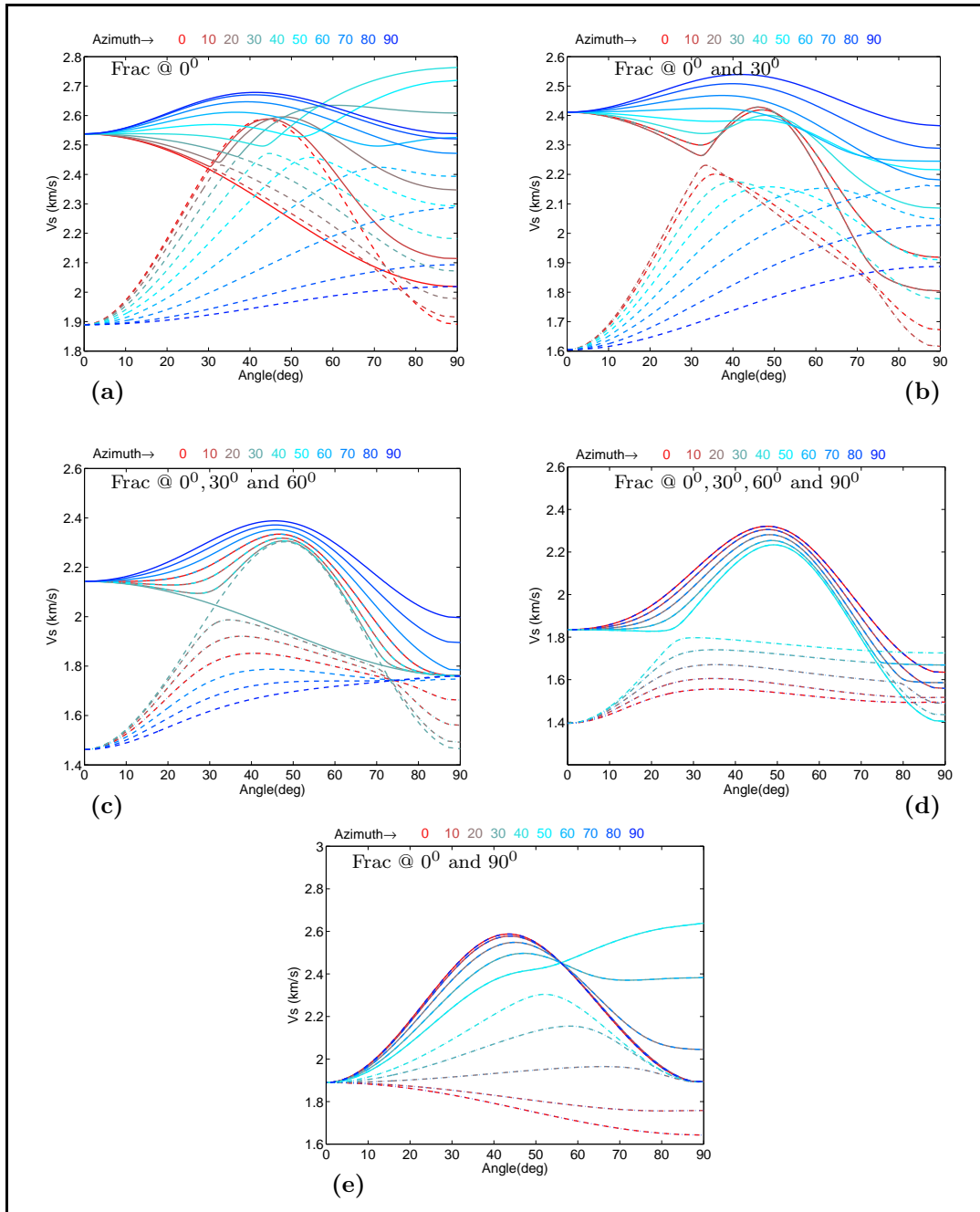
Figure 6.3: Shear wave velocity anisotropy for the five fracture models. S1 is plotted by solid line and S2 is plotted by a dashed line. Only overlapping curves are plotted by dotted dash lines to show the underlying curves.
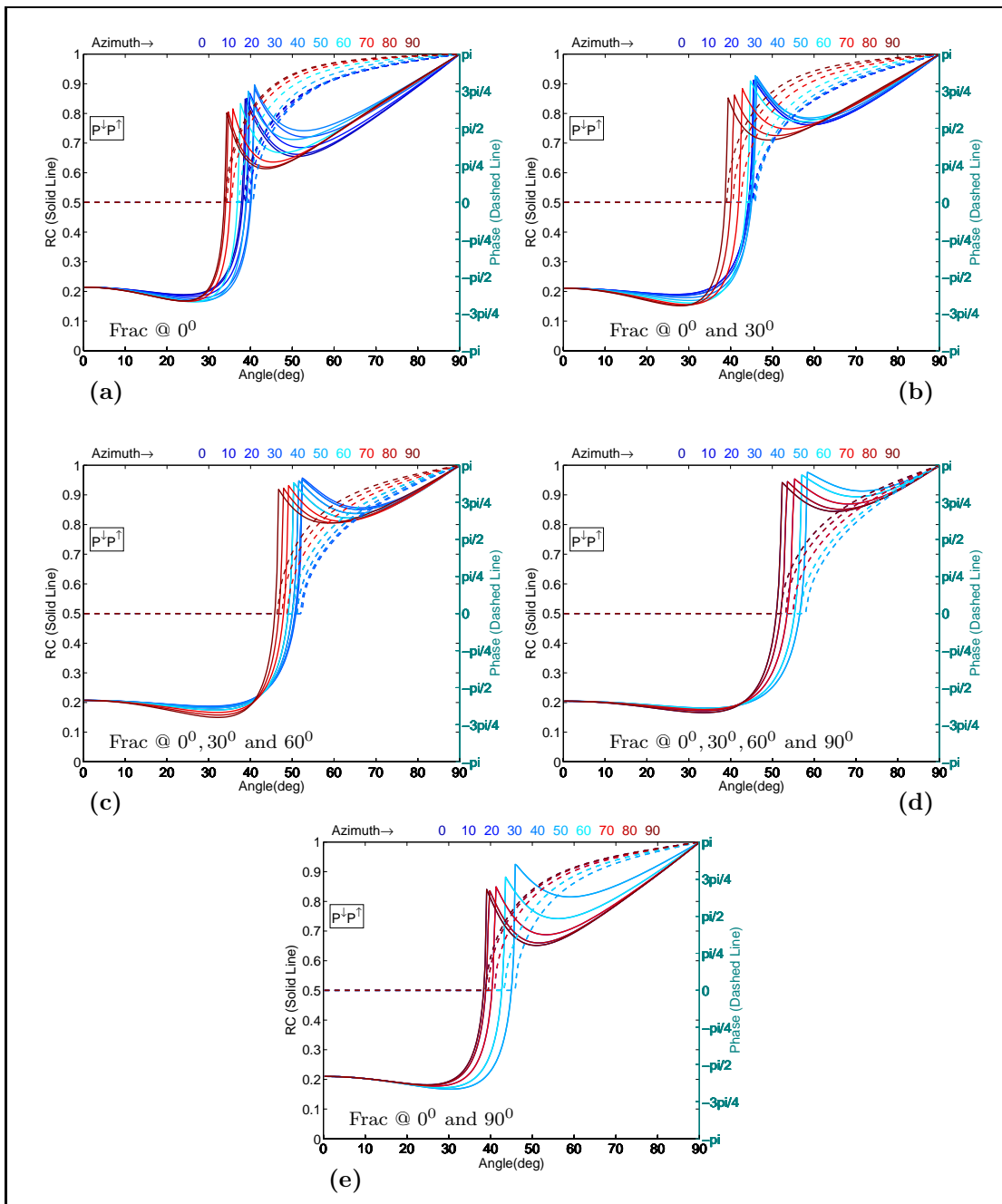
Figure 6.4: PP reflection coefficient and phase variation with angle and azimuth.
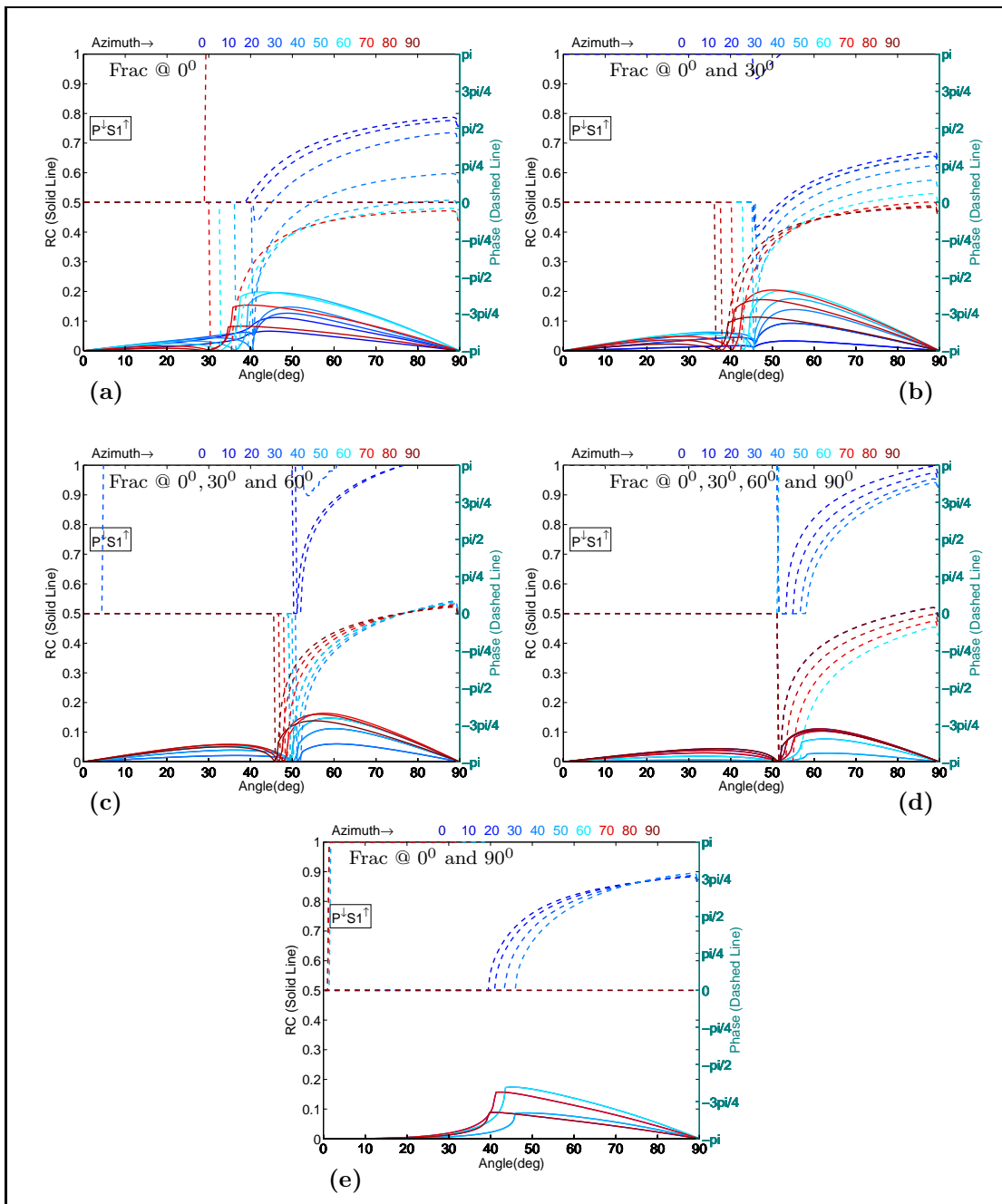
Figure 6.5: PS1 reflection coefficient and phase variation with angle and azimuth.
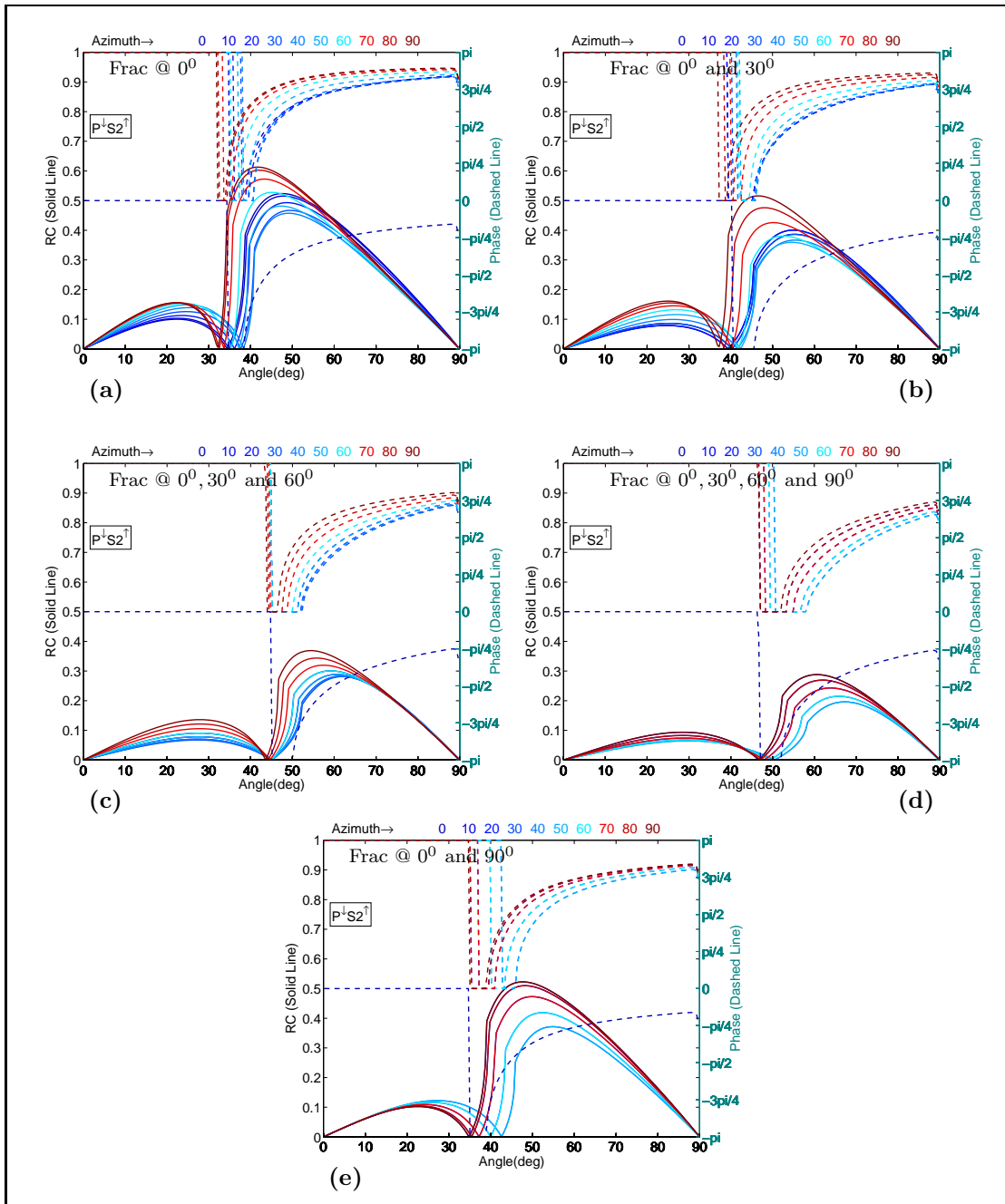
Figure 6.6: PS2 reflection coefficient and phase variation with angle and azimuth.

6.4   Summary

Schoenberg and Sayers' (1995) method was used to include multiple sets of vertical fractures in an initially VTI shale. Modeling of reflection coefficients in a fractured reservoir suggests the following:

1. The anisotropy in the medium decreases as the number of fracture sets increases.

2. PP reflections show the change of the critical angle due to the presence of fracture sets in the reflecting medium.

3. Shear waves are more sensitive to fractures, as compared to the P-waves.

Thus, the reflectivity modeling of a fractured reservoir coupled with AVOAz analysis from surface seismic data can potentially be applied in the fracture characterization.

Chapter 7

Synthetic Seismogram: Mathematical Details for Computation Purposes

7.1 Introduction

In the previous chapters, theoretical and computational aspects of Green-Christoffel's equation and formulation for layer matrices and associated wavefields were discussed. So far, all the mathematical treatments were in the frequency and slowness domains. However, the seismograms are recorded in the time domain and therefore, change from the frequency-slowness domain to the time-space domain is essential. It involves integration over frequency and slowness. This chapter gives mathematical details of the numerical techniques to implement the integration scheme.

Early development of body wave synthetic seismograms in anisotropic media was restricted by the computational power. Less computational intensive methods were developed based on ray theory to compute body waves synthetic seismograms in anisotropic media (Cerveny, 1972; Petrashen and Kashtan, 1984; Gajewski and Psencik, 1987). However, the ray method has a reduced accuracy (Martynov

76

and Mikhailenko, 1984). Though the full waveform method is computationally intensive, it allows accurate computation of synthetic seismograms (Cormier and Richards, 1977; Booth and Crampin, 1983; Gajewski and Psencik, 1987). For layered anisotropy computational procedure are simplified (Taylor, 1987; Fryer and Frazer, 1987). Chesnokov and Abaseev (1986) performed integration over vertical slowness to get the solution of the stationary problem. Tsvankin and Chesnokov (1990) proposed an approach based on an analytical approximation of amplitude and phase terms of the integral kernel.

Here, the spectral approach of computing synthetic seismograms is followed (i.e. slowness integration is performed first and then the inverse Fourier transform is performed). The Bessel function is used to economize computational time.

7.2 Polarization in (ω - p) domain

Having calculated the wavefield at the receivers (section 5.4) and layer matrices (chapter 4), one can obtain polarization in the frequency-slowness (i.e. $\boldsymbol{\omega} - \mathbf{p}$) domain from the matrix-vector product:

$$U = L_m \cdot f, \tag{7.1}$$

where L_m and f are a layer matrix and a vector of excitation coefficients, respectively, at a receiver location. However, seismic records are in the time-space domain. Therefore, it is required to transform the above equation 7.1 into the $(t - \mathbf{x})$ domain, and this is described in the next section.

7.3 Polarization in the $(t - x)$ domain - Synthetic Seismogram

Using the Fourier transformation, one can write,

$$u(x, y, z_r, t) = \frac{1}{8\pi^3} \int \int \int u(k_x, k_y, z_r, \omega) exp[i(\omega t - k_x x - k_y y)] dk_x dk_y d\omega \quad (7.2)$$

where k_x and k_y are wavenumbers in x- and y- directions, respectively. By a change of variable $k = p\omega$, equation (7.1) can be written as:

$$u(x, y, z_r, t) = \frac{1}{8\pi^3} \int \int \int \omega^2 u(p_x, p_y, z_r, \omega) exp[i(\omega t - p_x x - p_y y)] dp_x dp_y d\omega \quad (7.3)$$

Furthermore, one can rotate the medium azimuthally (about the z-axis) such that the x-axis in the current orientation coincides with the radial direction of the receiver from the source. In this case, the Bessel function approach can be utilized to reduce the overall CPU time of the integration procedure.

Let us use the following change of variable:

$$p_x = p \cos \phi, \quad p_y = p \sin \phi$$

where ϕ is the angle of rotation in the x-y plane. Therefore,

$$dp_x = -p\sin\phi\,d\phi + \cos\phi\,dp$$

$$dp_y = p\cos\phi\,d\phi + \sin\phi\,dp$$

$$dp_x dp_y = -p\sin^2\phi\,d\phi\,dp - p\cos^2\phi\,d\phi\,dp$$

$$+ p^2\sin\phi\cos\phi\,(d\phi)^2 + \sin\phi\cos\phi\,(dp)^2$$

$$= -p\sin^2\phi\,d\phi\,dp - p\cos^2\phi\,d\phi\,dp$$

$$= -p\,d\phi\,dp = p\,dp\,d\phi \qquad (7.4)$$

Thus, equation (7.2) can be written as:

$$u(x,y,z_r,t) = \frac{1}{2\pi}\int d\omega\,\omega^2 e^{i\omega t}\int\int u(p,\phi,z_r,\omega)e^{-i\omega pr\cos\phi}p\,dpd\phi \qquad (7.5)$$

Using Bessel's function series expansion, one can write the above equation as:

$$u(x,y,z_r,t) = \frac{1}{2\pi}\int d\omega\,\omega^2 e^{i\omega t}\int dp\,p\int\sum_m u(p,\phi,z_r,\omega)J_m(\omega pr)e^{-im\phi}d\phi \qquad (7.6)$$

where m is the angular order. In the case of a point force in a VTI medium, the summation over angular order m is in fact performed over the range $-2 \leq m \leq 2$ (Fryer and Frazer, 1984). However, if the medium is azimuthally anisotropic, the angular order m retained should be fairly large in order to gain reasonable accuracy.

The following form of the Bessel function is utilized in the VTI subroutine.

$$e^{-ixcos\phi} = J_0(x) + 2\sum_{m=1}^{\infty}(-i)^m J_m(x)\cos(m\phi) \qquad (7.7)$$

The Bessel series expansion in the form 7.7 is derived in Appendix E. For a VTI medium, u is independent of ϕ and m varies up to 2. Therefore, equation 7.6 can be simplified for a VTI medium as:

$$
\begin{aligned}
u(x, y, z_r, t) &= \frac{1}{2\pi} \int d\omega \; \omega^2 e^{i\omega t} \int dp \; p \; u(p, z_r, \omega) \\
&\quad \int J_0(x) + 2 \sum_{m=1}^{2} (-i)^m J_m(x) \cos(m\phi) d\phi \\
&= \frac{1}{2\pi} \int d\omega \; \omega^2 e^{i\omega t} \int dp \; p \; u(p, z_r, \omega) \\
&\quad \left[J_0(x) 2\pi + 2 \sum_{m=1}^{2} (-i)^m J_m(x) \int \cos(m\phi) d\phi \right]
\end{aligned}
\tag{7.8}
$$

7.4 Frequency Filtering

The frequency filtering is introduced here to allow for the amplitude-frequency response of the geophones. In equation (7.6) the innermost integral is over slowness and is computed as discussed in the previous section. The outer integral is over frequency and requires a damping factor to remove the ringing effect in the signal. Let us denote the inner integral by $S(\omega)$ and damping factor by $\varphi(f)$. Thus, equation (7.6) can be expressed as:

$$
u(r, t) = \int \omega^2 \varphi(f) S(\omega) e^{i\omega t} dt
\tag{7.9}
$$

A Gaussian filter $\varphi(f)$ is used, and it has the form:

$$
\varphi(f) = e^{-\alpha(f/f_c)^2}
\tag{7.10}
$$

80

where f_c is a cut-off frequency and is chosen from the frequency response of receivers. α is a filter parameter to remove ringing.

7.5 Sampling Frequency

In order to avoid aliasing in the signal, sampling frequency up to the Nyquist frequency (Yilmaz, 2000) is used and defined as:

$$f_{Nyquist} = \frac{1}{2\Delta t} \qquad (7.11)$$

where Δt is the time sampling interval. Thus, with a view to use the Fast Fourier Transform, the sampling frequency interval is determined by the following formula:

$$\Delta f = \frac{1}{\Delta t \cdot N_t} \qquad (7.12)$$

where N_t is the total number of time samples.

7.6 Constrained Cubic Interpolation

The interpolation just mentioned allows us to gain a higher order of accuracy of the integration procedure. In this section, a method is discussed to find a cubic polynomial passing through two points at x_0 and x_1, where the function values

and their first derivatives are known. Let the function be $F(x)$ with coefficients $C_0, C_1, C_2,$ and C_3 such that

$$F(x) = C_0 + C_1(x - x_0) + C_2(x - x_0)^2 + C_3(x - x_0)^3$$

$$= C_0 + C_1(x_1 - x_0)\left(\frac{x - x_0}{x_1 - x_0}\right) + C_2(x_1 - x_0)^2\left(\frac{x - x_0}{x_1 - x_0}\right)^2$$
$$+ C_3(x_1 - x_0)^3\left(\frac{x - x_0}{x_1 - x_0}\right)^3$$

$$= Cn_0 + Cn_1\left(\frac{x - x_0}{x_1 - x_0}\right) + Cn_2\left(\frac{x - x_0}{x_1 - x_0}\right)^2 + Cn_3\left(\frac{x - x_0}{x_1 - x_0}\right)^3$$

$$(7.13)$$

where $Cn_0 = C_0, Cn_1 = C_1(x_1 - x_0), Cn_2 = C_2(x_1 - x_0)^2$ and $Cn_3 = C_3(x_1 - x_0)^3$.

Differentiating $F(x)$ with respect to x, one obtains:

$$(x_1 - x_0)F'(x) = Cn_1 + 2Cn_2\left(\frac{x - x_0}{x_1 - x_0}\right) + 3Cn_3\left(\frac{x - x_0}{x_1 - x_0}\right)^2$$

or, $$Fn'(x) = Cn_1 + 2Cn_2\left(\frac{x - x_0}{x_1 - x_0}\right) + 3Cn_3\left(\frac{x - x_0}{x_1 - x_0}\right)^2 \qquad (7.14)$$

where $Fn'(x) = (x_1 - x_0)F'(x)$.

The boundary conditions reduce equations 7.13 and 7.14 to:

$$F_0 = Cn_0$$

$$F_1 = Cn_0 + Cn_1 + Cn_2 + Cn_3$$

$$Fn_0' = Cn_1$$

$$Fn_1' = Cn_1 + 2Cn_2 + 3Cn_3$$

$$(7.15)$$

Solving the set of equations in 7.15 for the coefficients Cn, one obtains:

$$Cn_0 = F_0$$

$$Cn_1 = Fn_0'$$

$$Cn_2 = 3F_1 - Fn_1' - 3F_0 - 2Fn_0'$$

$$Cn_3 = 2F_0 - 2F_1 + Fn_0' + Fn_1'$$

$$(7.16)$$

Finally,

$$C_0 = Cn_0$$

$$C_1 = \frac{Cn_1}{x_1 - x_0}$$

$$C_2 = \frac{Cn_2}{(x_1 - x_0)^2}$$

$$C_3 = \frac{Cn_3}{(x_1 - x_0)^3}$$

$$(7.17)$$

7.7 Summary

This chapter is summarized as follows:

1. Integration over azimuthal angle is optimized by the use of the Bessel function series expansion.

2. In the framework of VTI media the Bessel function series reduces down to the second angular order.

3. The frequency filter is introduced to allow for the amplitude-frequency response of the geophones.

4. Constrained cubic interpolation allows us to gain a higher order of accuracy of the integration scheme.

Chapter 8

Synthetic Seismograms in Homogeneous and Multilayered VTI media

8.1   Introduction

In this chapter, full waveform synthetic seismograms in attenuating homogeneous and multilayered VTI media, their radiation patterns and spectral characteristics are investigated. This approach allows us to study seismic wave characteristics in anisotropic attenuating media. This frontier area of research in seismic methods has a potential application in hydraulic fracturing of shaly reservoirs. Shales are commonly VTI and hydraulic fracturing can potentially alter the velocity and attenuation properties.

There are various causes of attenuation; however, they are characterized into two types: scattering and intrinsic attenuation. Irrespective of its mechanism, attenuation is specified by $1/Q$ where Q is the quality factor(Johnston and Toksoz, 1981). A viscoelastic or attenuating medium can be treated numerically by allowing the elastic coefficients to be complex (White, 1965). The full waveform synthetic program

developed as part of this dissertation allows us to compute synthetic seismograms in viscoelastic media by giving separate values of Q for each layer in a multilayered anisotropic media.

Radiation patterns in elastic anisotropic media have been investigated by Gajewski (1993) using the ray theory approach and by Tsvankin and Chesnokov (1990) using the full waveform theory. Zhu and Tsvankin (2006) studied plane wave propagation in attenuating VTI media. However, they have not shown the effect of attenuation on the classical "butterfly" radiation pattern of dislocation source models used for earthquakes.

In the first section, the effects of a point force on synthetic seismograms are explained. In the next section, it is shown that the attenuation can modify the radiation patterns of P- and S-waves for the basic point force solutions. This helps in our understanding of spectral decomposition of a full waveform synthetic in an attenuating multilayered anisotropic medium. The basic idea is to attempt to identify the propagation and source effects of attenuation. Simple modeling in this study suggests that the spectral decomposition has much potential for identifying attenuating media (e.g. hydrocarbon reservoir).

8.2 Point force orientation and synthetic seismograms

Seismograms have signatures of both the source and the media. They are combined results of source radiation and propagation effects through the media. Therefore, it is important to understand the radiation patterns of various wave types. Figure 8.1

shows P- and S-wave radiation patterns in a plane containing the vertical force in
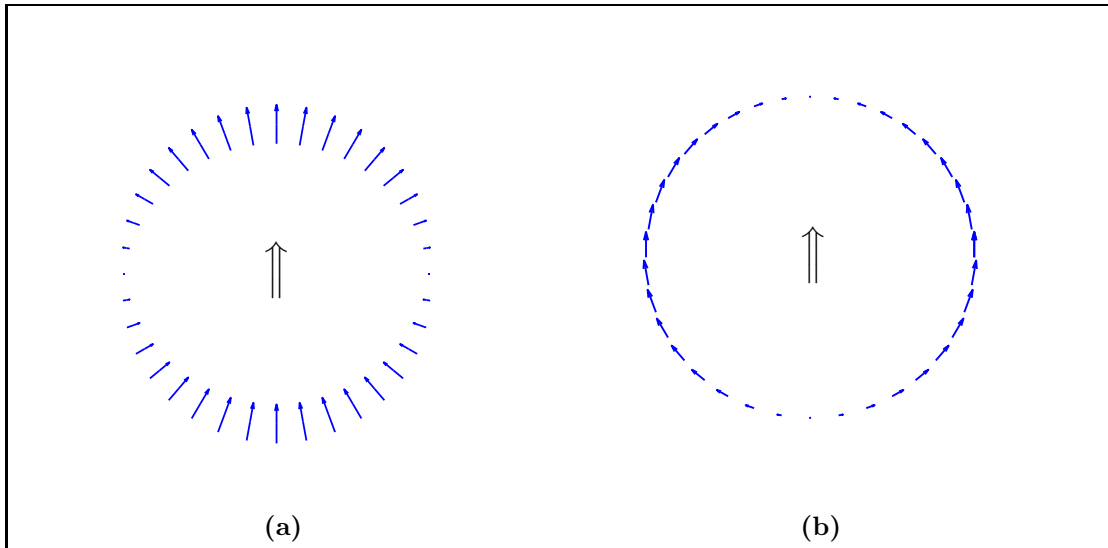an unbounded homogeneous isotropic medium (Aki and Richards, 2002).

Figure 8.1: (a) P-wave radiation pattern (b) S-wave radiation pattern in isotropic
media. Arrows at the centers indicate the direction of force.

Important points to note here are:

- Polarization directions are shown by the arrows. P-waves are polarized in the
  direction of wave propagation, and S-waves are polarized transversely to it.

- P-wave has zero amplitude in the horizontal plane and maximum in the vertical
  direction.

- S-wave has zero amplitude in the vertical direction and maximum in the X-
  direction.

- Vertical components of P-wave polarizations in the upper half space are out-
  ward, whereas they are inward in the lower half space. Horizontal components
  are always away from the source.

- Vertical components of S-wave polarizations are in the direction of the applied force and horizontal components are inward in the upper half-space and outward in the lower half-space.

- Horizontal components of P- and S-waves are polarized in opposite directions, whereas their vertical components are polarized in the same direction.

Now let us investigate the radiation patterns in an unbounded homogeneous VTI medium. The five independent elastic coefficients and density of this medium are: $C_{11} = 21.26$, $C_{33} = 17.63$, $C_{44} = 5.32$, $C_{66} = 8.99$, $C_{13} = 6.97$ GPa and $\rho = 2.34$ g/cc. The phase velocity characteristics of P-, SH- and SV-waves in the medium are shown in Figure 8.2.
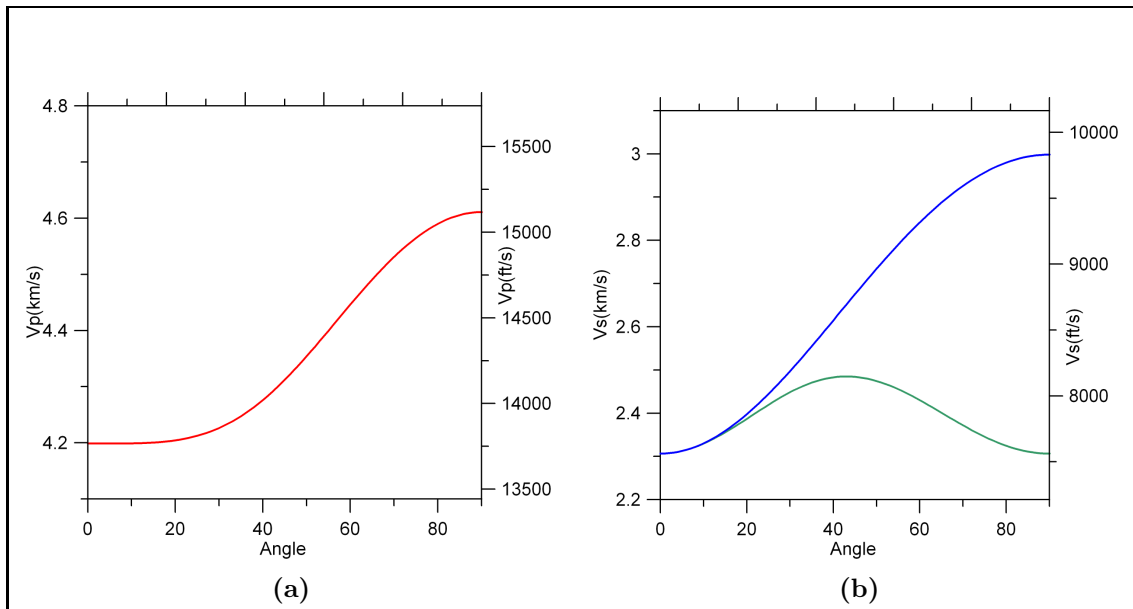

Figure 8.2: Phase velocity variation with angle for P-wave is shown in (a), and SV(Green) and SH(Blue) waves are shown in (b).

Four different orientations of a force vector are considered to show their effects on the radiation pattern. Receivers are placed at 1 km radius from the source in a vertical plane. The frames of 3-component receivers are oriented just as the standard cartesian system is, with radial, transverse and vertical components being along the X-, Y-, and Z-axis, respectively. Arrival times of P- and S-waves are recorded and plotted radially such as Figure 8.3a. Such plots have radii in temporal units and are in the vertical plane (X-Z plane) containing all the receivers. If such a plot were to be made for an isotropic medium, it would have a constant arrival time forming a quarter circle. In anisotropic medium the arrival times of P- and S-waves do not conform to circles. P-wave arrives before S-waves. Deviation of the color from the background indicates polarity of the waves and intensity of the color is indicative of wave amplitude.

1. **Vertical force**: Here, the force vector is along the Z-direction. It produces displacement in vertical and radial directions only, and there is no transverse component of the displacement. This is shown in figure 8.3. Displacement components are shown in the X-Z plane. Figure 8.4 shows a synthetic seismogram plotted in a conventional way. Red, blue and bluish green colors indicate the radial, transverse and vertical component, respectively. Gray color indicates absolute value of the displacement. This color scheme for synthetic seismograms is followed throughout this dissertation. Note that the radial components of P- and SV-wave are polarized in the opposite direction, whereas vertical components are in the same direction. Displacement amplitude is also consistent with the observation made in the isotropic case.

2. **Radial force**: In this case, the force is applied in the radial direction. Here, we do not observe any transverse component either (Figures 8.5 and 8.6). The radial component of P- and SV-waves are now polarized in the same direction, while their horizontal components are in the opposite direction.

3. **Transverse force**: Transverse force could excite SH only. P- and SV-waves are vanishing in the X-Z plane (Figures 8.7 and 8.8).

4. **Diagonal force**: This force has three components equal in magnitude. In this case, all the wave types, namely P, SV and SH, are excited in the X-Z plane (Figures 8.9 and 8.10). It is important to emphasize here that the plane containing the force vector will not have a transverse wave in the VTI media.

In this section, the polarization directions of different wave types are explained. The amplitude of polarizations of P and S waves are investigated in detail in the next section.
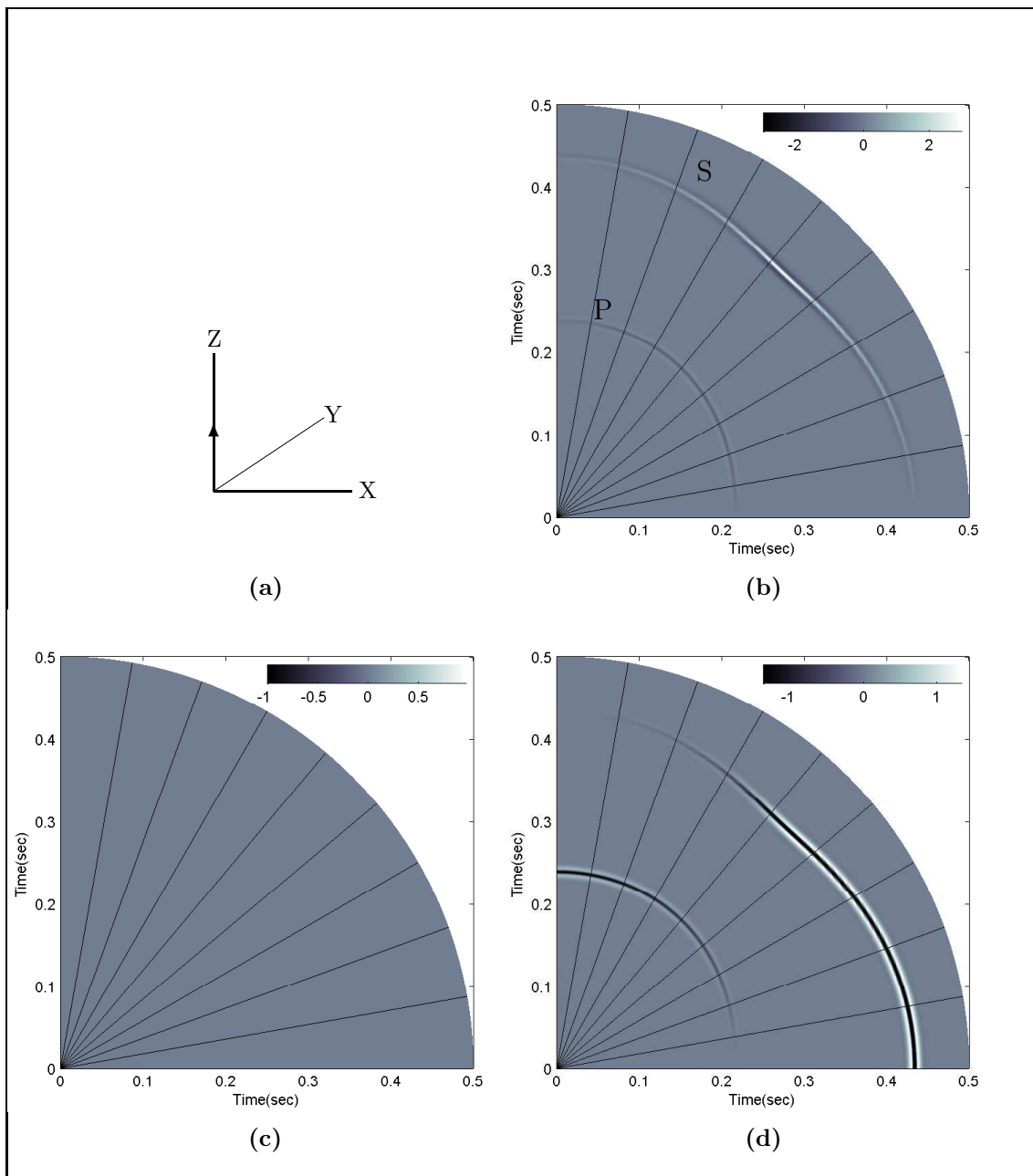
Figure 8.3: Application of force vector in Z-direction as shown in (a) produces displacement components in (b) radial and (d) vertical directions only. Transverse component as shown in (c) is zero. Arrivals of P- and S-waves are plotted radially in a vertical plane for receivers at a distance of 1km from the source. Change in color shades from the background shows the polarization direction (+ve or -ve) and intensity of the color is indicative of amplitude of displacement.
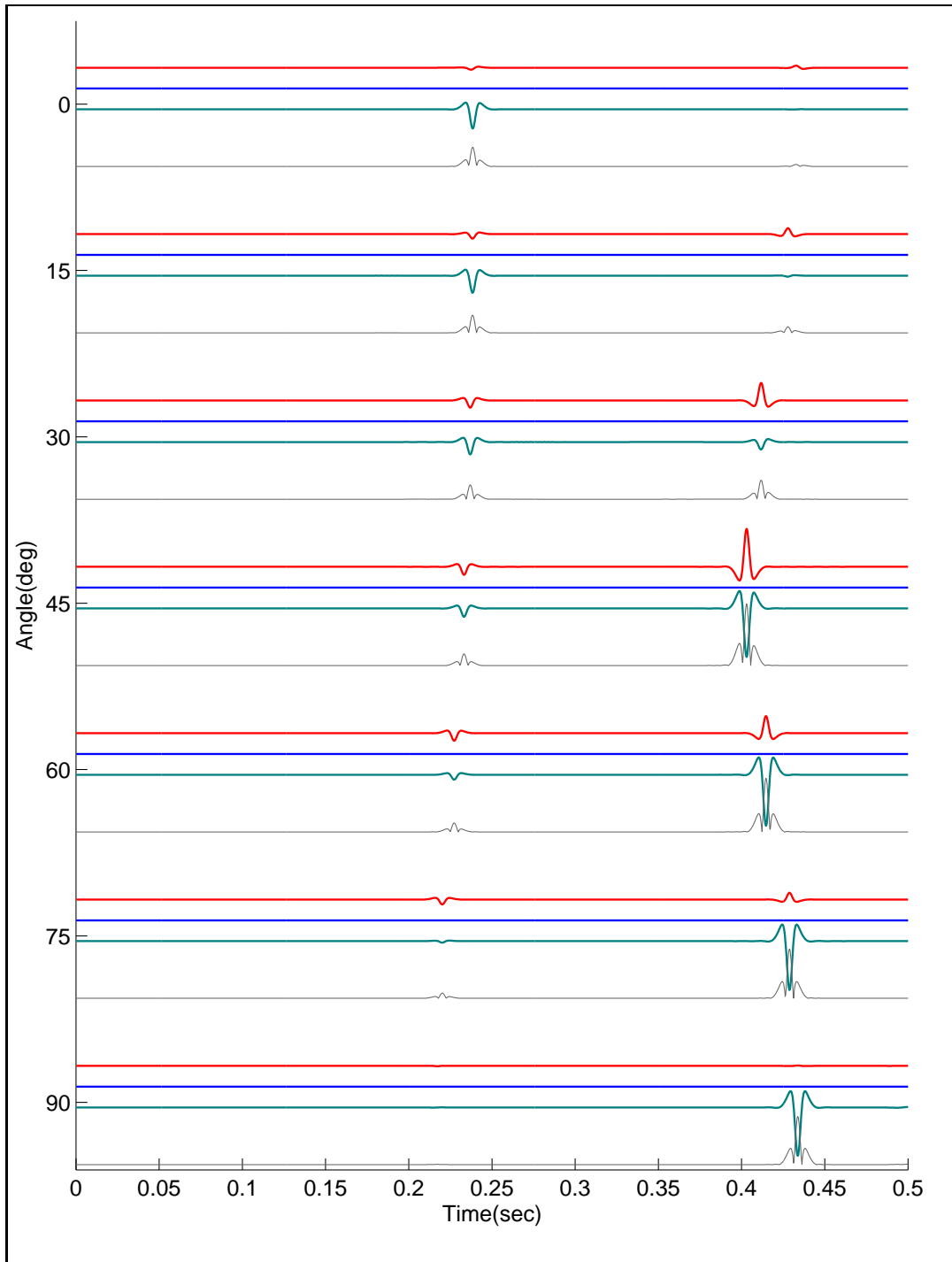
Figure 8.4: Synthetic seismograms: X-component(red), Y-component(blue), Z-component(bluish green), Absolute amplitude value(gray).
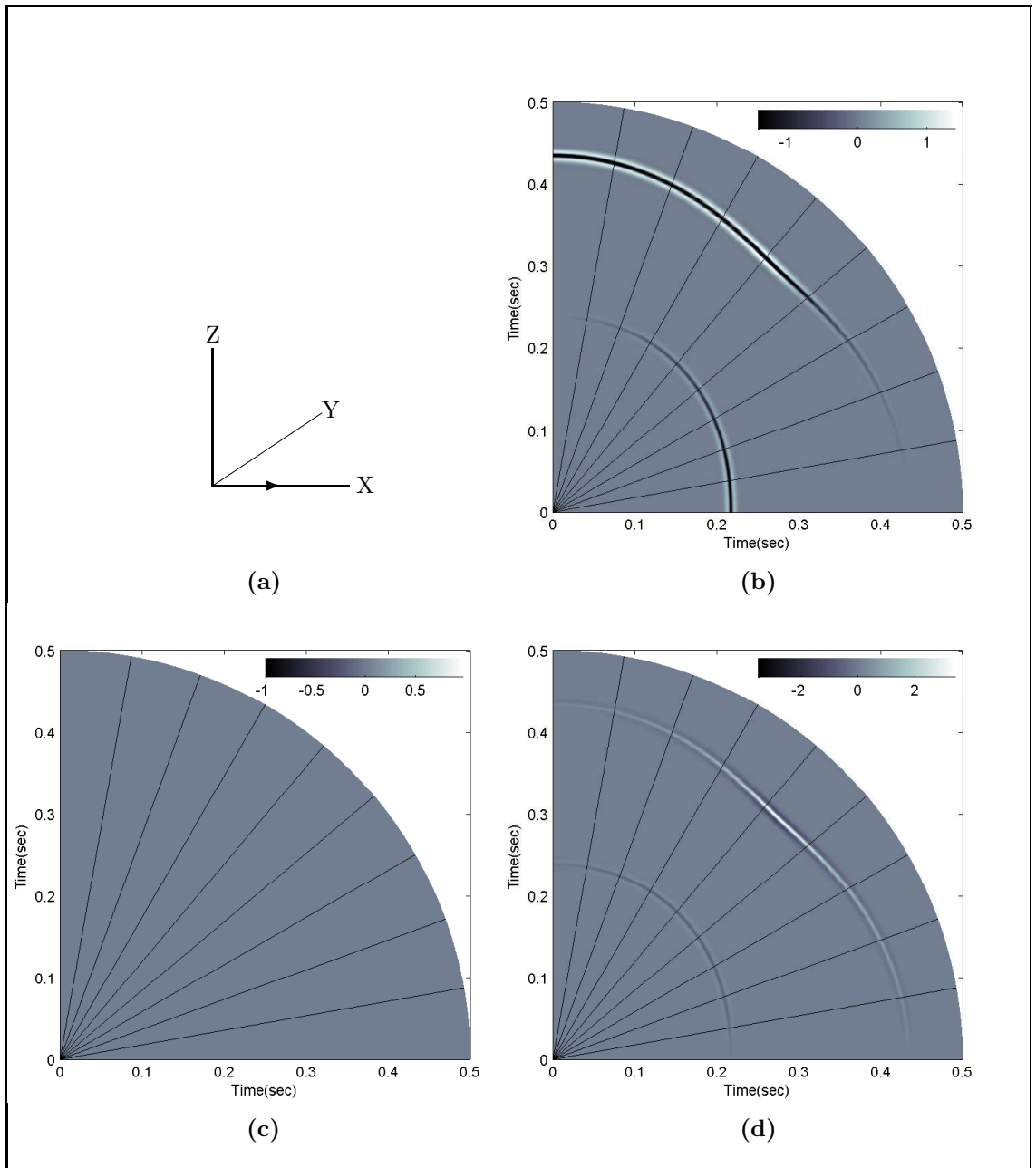
Figure 8.5: Application of force vector in the X-direction as shown in (a) produces displacement components in (b) radial and (d) vertical directions only. Transverse component as shown in (c) is zero.
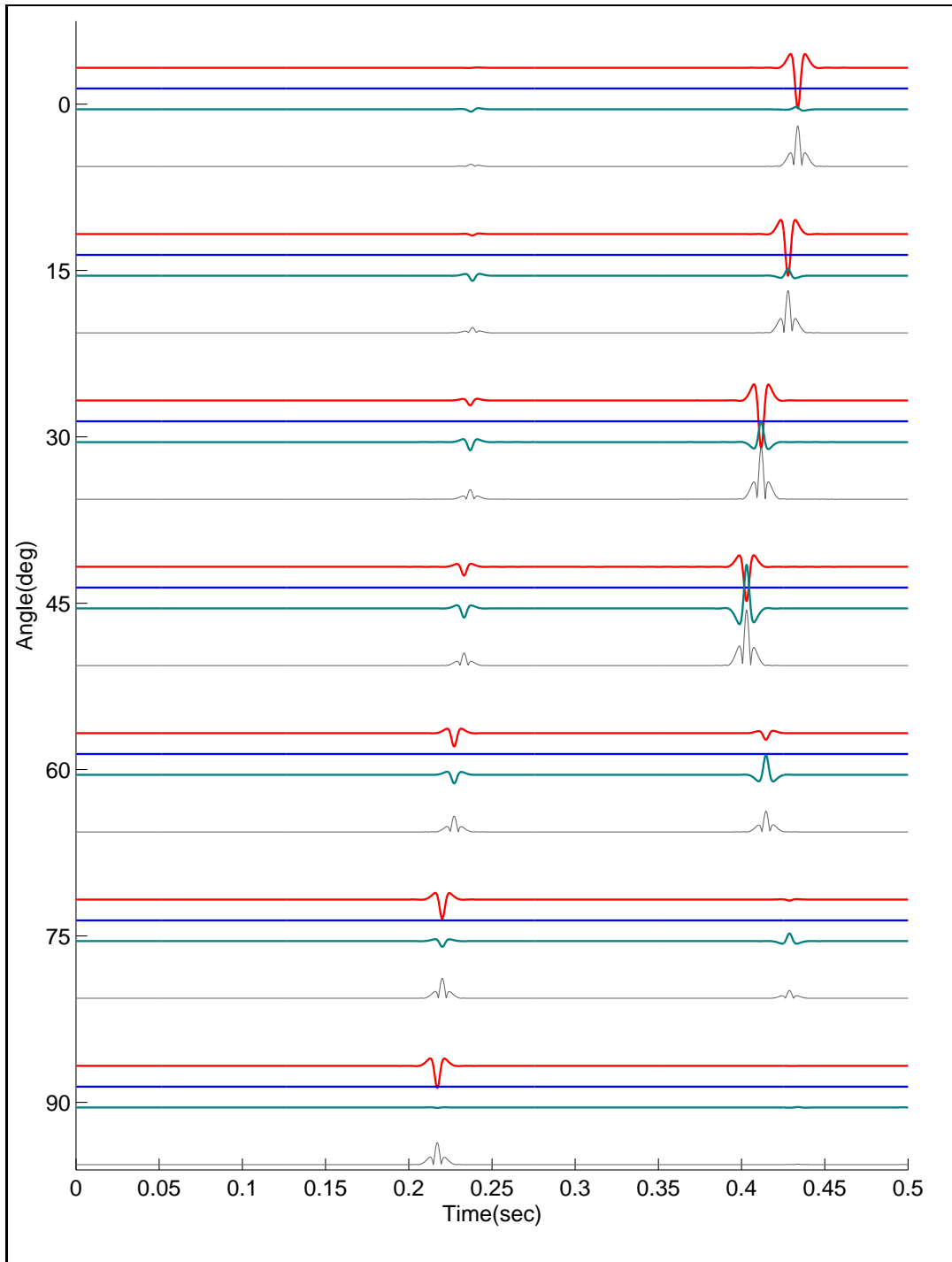
93

Figure 8.6: Synthetic seismograms: X-component(red), Y-component(blue), Z-component(bluish green), Absolute amplitude value(gray).
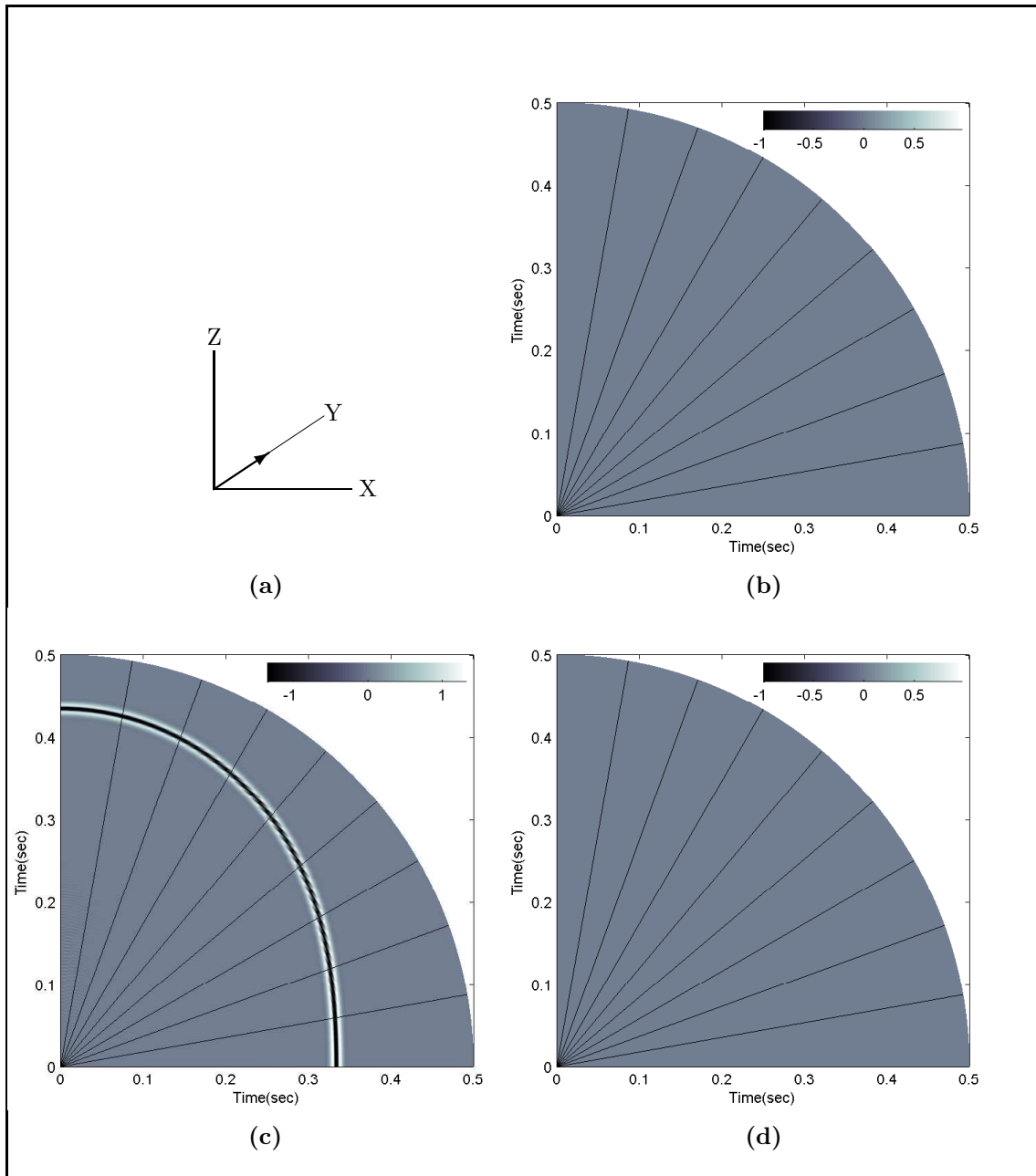
Figure 8.7: Application of force vector in the Y-direction as shown in (a) produces displacement components in transverse direction only as shown in (c). There is no (b) radial and (d) vertical components of the displacements.

Figure 8.8: Synthetic seismograms: X-component(red), Y-component(blue), Z-component(bluish green), Absolute amplitude value(gray).

Figure 8.9: Diagonal force applied as shown in (a) in the VTI medium produces the displacement components in all three directions. (b) radial component (c) transverse component (d) vertical component. The absolute value of the displacement is shown in (e).

97
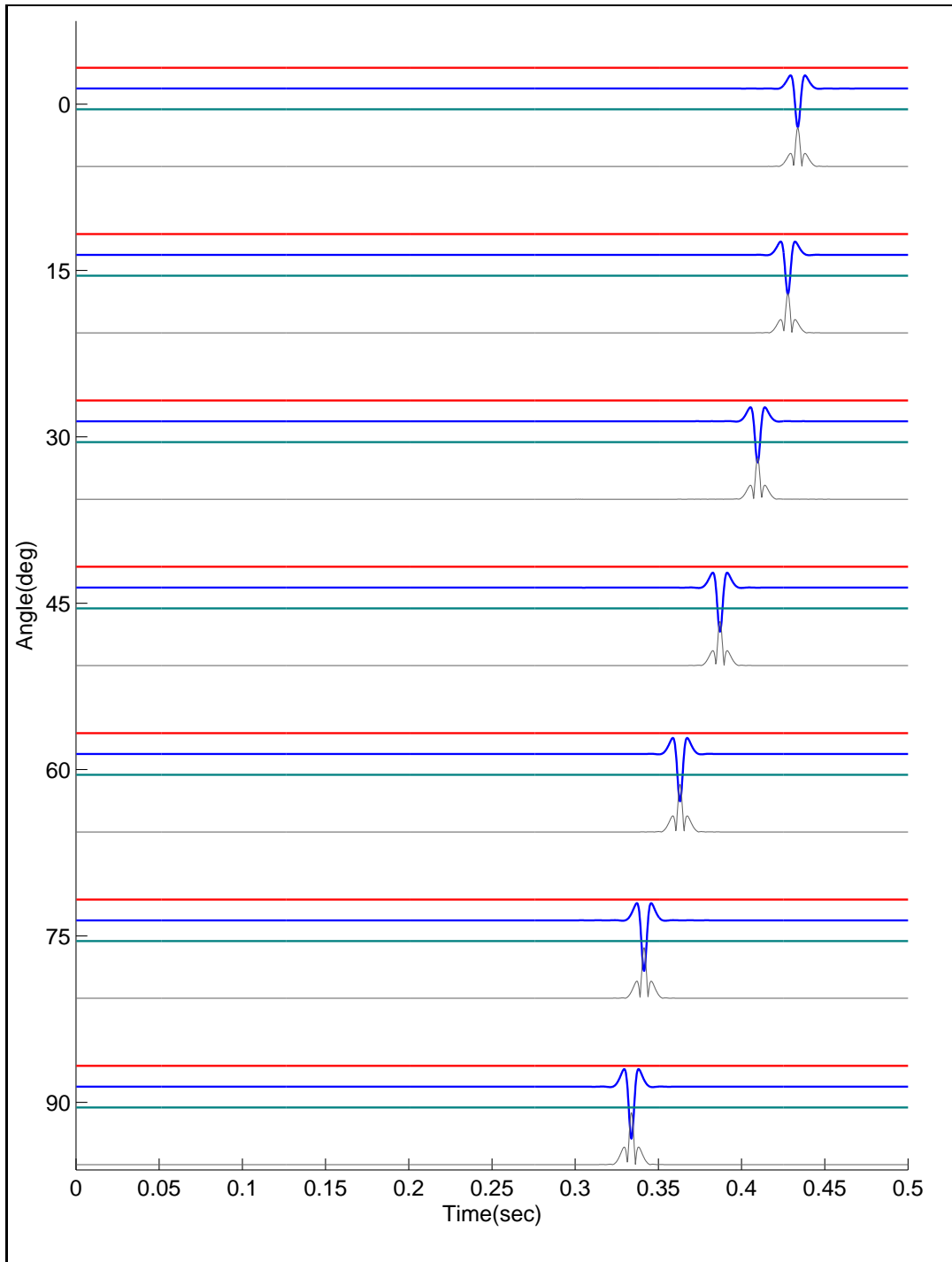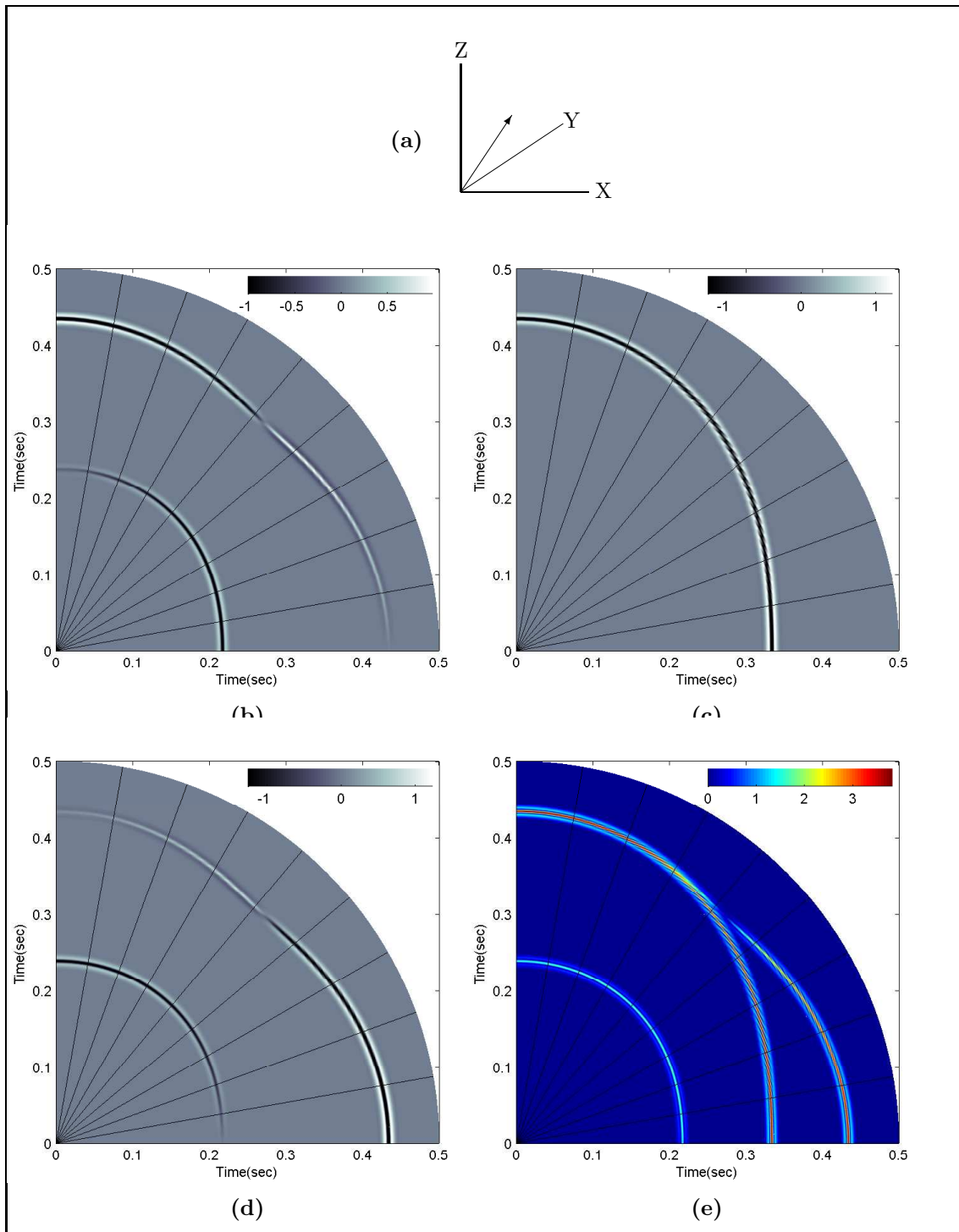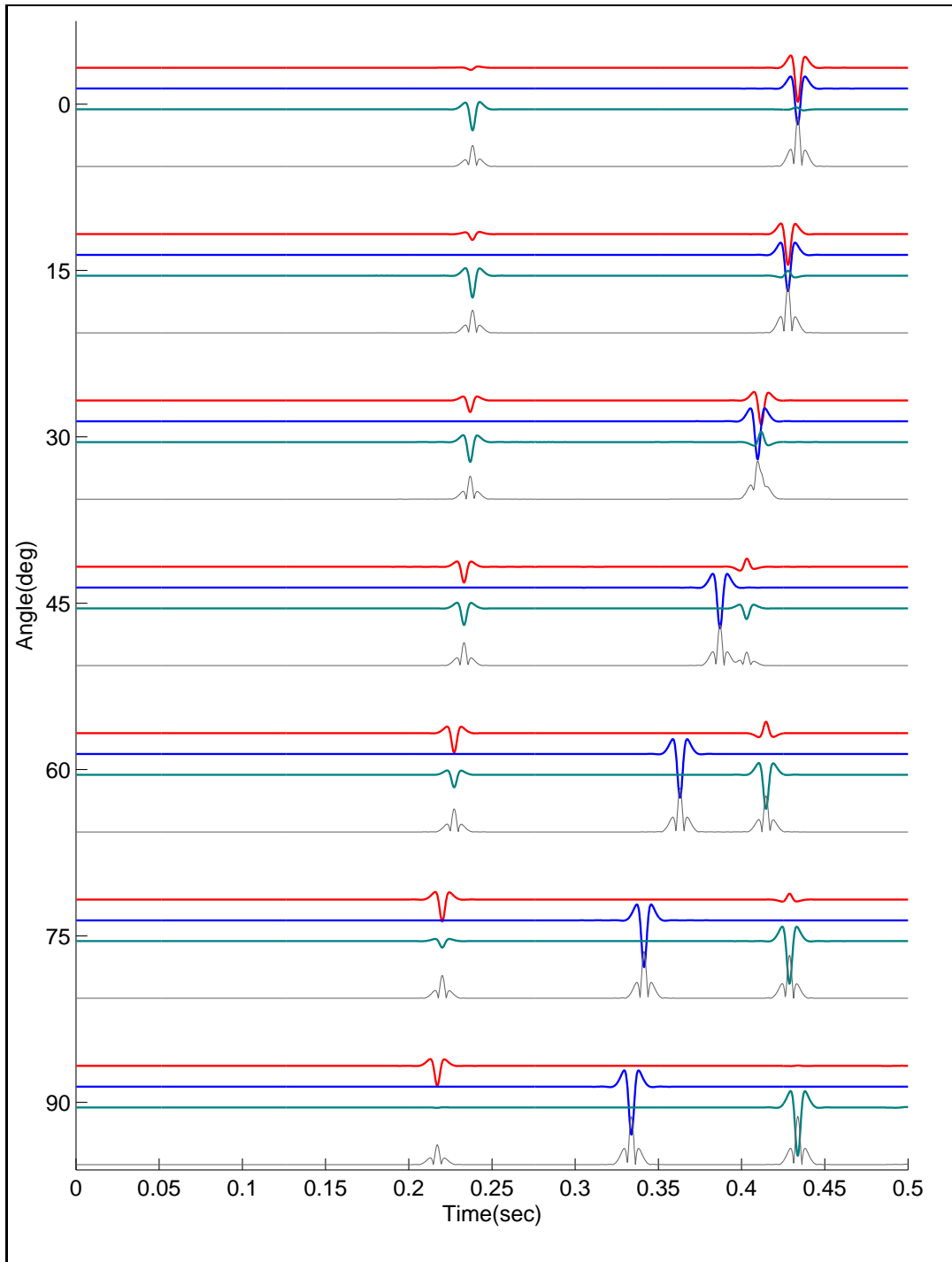
Figure 8.10: Synthetic seismograms: X-component(red), Y-component(blue), Z-component(bluish green), Absolute amplitude value(gray).

8.3 Effects of Attenuation on Radiation Pattern in Homogeneous Media

Effects of anisotropy on radiation patterns in terms of amplitudes of P- and S-waves were investigated by Tsvankin and Chesnokov (1990) and Gajewski (1993). Here the effects of attenuation on radiation amplitudes of P- and S-waves are addressed. The response of an unbounded homogeneous VTI medium to a vertical force is analyzed. The VTI model under consideration has the same elastic constants and density, which was used in the previous section, and it's phase velocity behavior is shown in figure 8.2. Attenuation is incorporated in the medium by the quality factor($\mathbf{Q}$). The quality factor is defined as the quantity proportional to the ratio of the real and imaginary part of elastic coefficients (White, 1965). The quality factor essentially represents a viscoelastic medium. Low values of Q suggest a high attenuating medium and vice-versa.

Here, radiation patterns are constructed as a polar diagram by taking the maximum amplitude of the first motions of P- and S-waves in a given plane. Here, the radiation pattern is shown in the vertical plane. The radiation pattern can also be thought of as a far-field radiation in terms of amplitude of the displacement. There are four subfigures in each figure starting from 8.11 to 8.18. Subfigures (a) and (b) in the figures show radial and vertical components, respectively, of P- and S-waves. Note that there is no transverse component, as the source is a vertical force and receivers are in a vertical plane. The absolute value of displacement is plotted in the subfigures (c). The subfigures (d) in these figures show the radiation pattern of P- and S-waves colored as red and blue, respectively. In order to show the effect of

99

anisotropy, the radiation pattern of an equivalent isotropic medium by a dashed line in Figure 8.11d. Radiation patterns are computed for Q equal to 50, 100, 300, 500, 1000, 5000, 10000 and 10, and are plotted in the same order. Radiation patterns appear as a "butterfly" with the head and tail showing P-wave radiation patterns and wings representing S-wave radiation patterns. Note that P-wave radiation shrinks as we increase the quality factor. In each radiation pattern the data are normalized to S-wave maximum amplitude. Change in amplitude can be summarized in a graph plotted in Figure 8.19. Amplitudes of P- and S-waves both decrease as we decrease the quality factor. Generally, an S-wave has a higher amplitude compared to that of a P-wave. Following a critical point on the attenuation axis the P-wave amplitude becomes larger than the S-wave amplitude, while in the radiation pattern "head and tail" becomes larger than the "wings" .

Figure 8.11: Attenuation parameter Q is 50. X- and Z-components of the synthetic seismograms are shown in (a) and (b), respectively. Absolute value of the displacement amplitude is shown in (c). Radiation patterns of P- and S-waves are shown in (d) with red and blue color, respectively. A dashed line represents radiation patterns in an equivalent isotropic medium.

101

Figure 8.12: Attenuation parameter Q is 100. X- and Z-components of the synthetic seismograms are shown in (a) and (b), respectively. Absolute value of the displacement amplitude is shown in (c). Radiation patterns of P- and S-waves are shown in (d) with red and blue color, respectively.
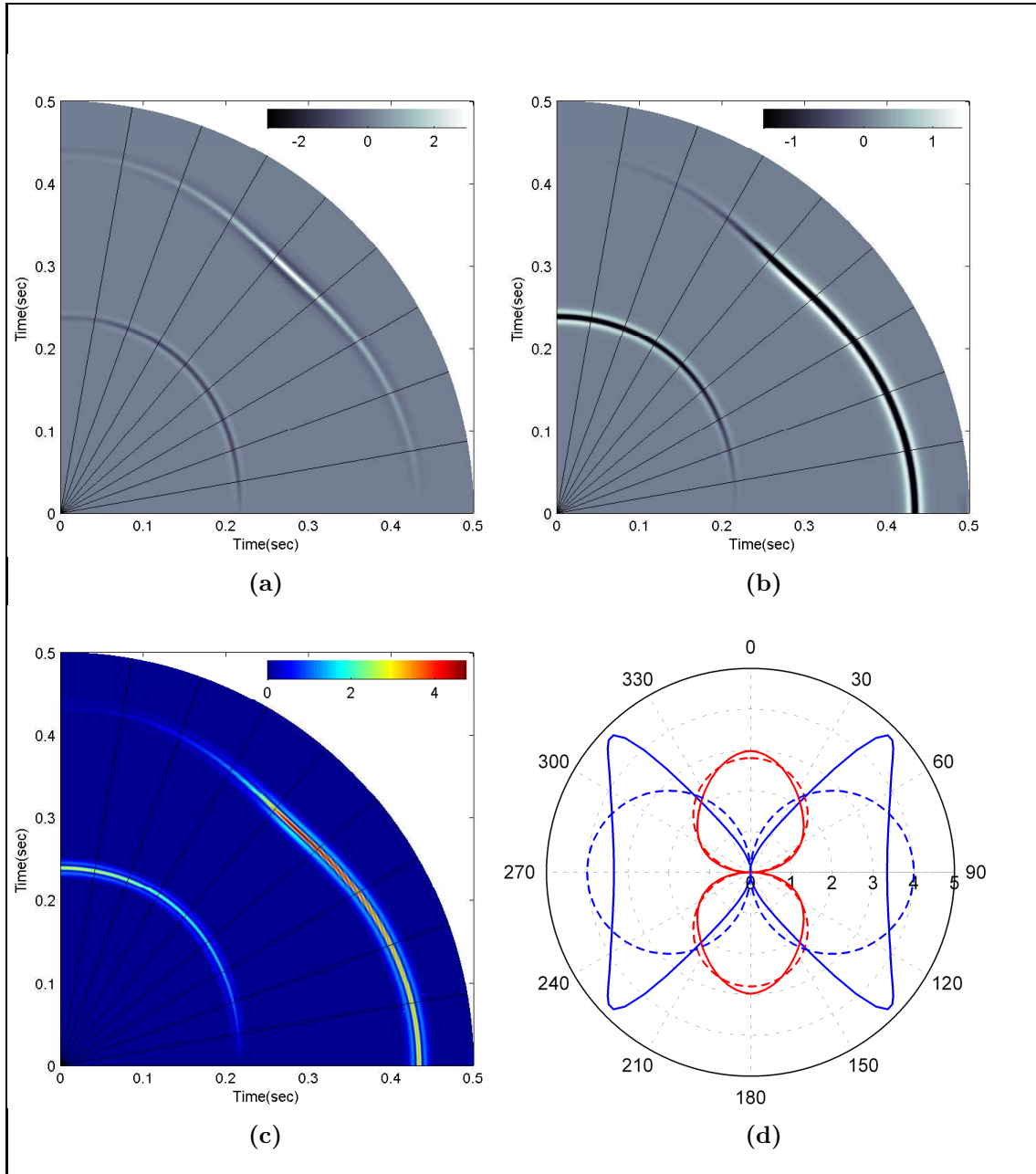
Figure 8.13: Attenuation parameter Q is 300. X- and Z-components of the synthetic seismograms are shown in (a) and (b), respectively. Absolute value of the displacement amplitude is shown in (c). Radiation patterns of P- and S-waves are shown in (d) with red and blue color, respectively.
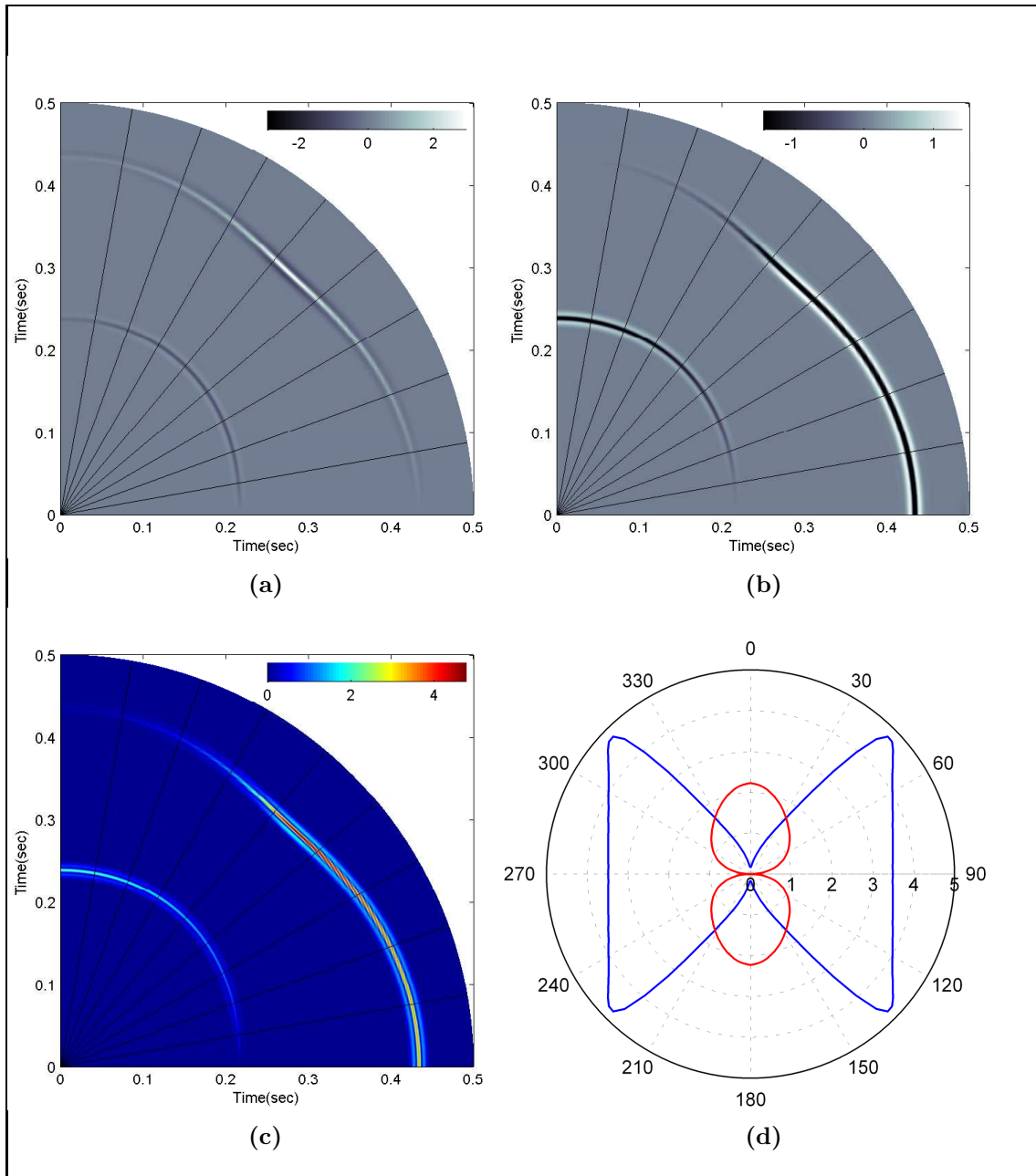
Figure 8.14: Attenuation parameter Q is 500. X- and Z-components of the synthetic seismograms are shown in (a) and (b), respectively. Absolute value of the displacement amplitude is shown in (c). Radiation patterns of P- and S-waves are shown in (d) with red and blue color, respectively.
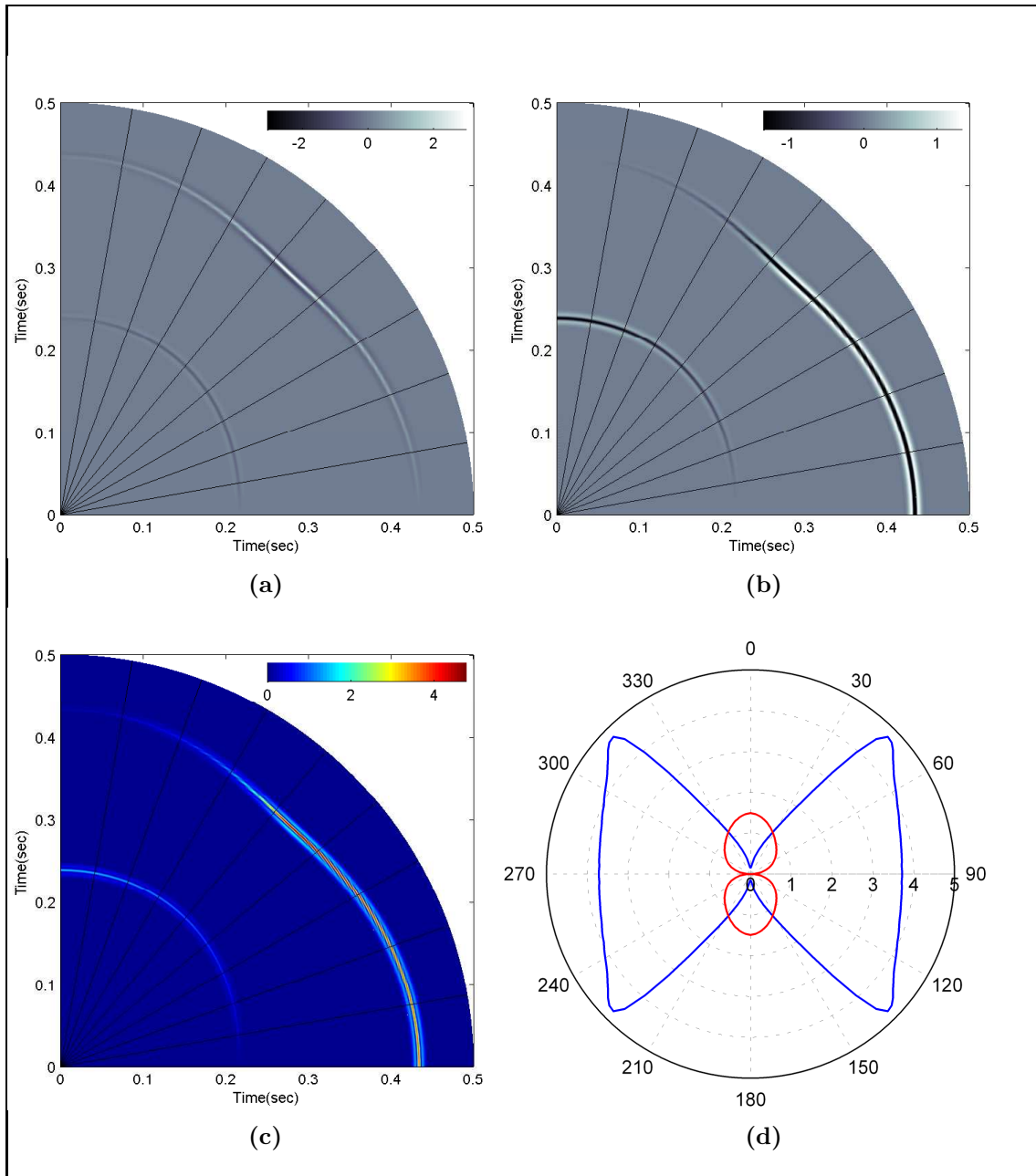
Figure 8.15: Attenuation parameter Q is 1000. X- and Z-components of the synthetic seismograms are shown in (a) and (b), respectively. Absolute value of the displacement amplitude is shown in (c). Radiation patterns of P- and S-waves are shown in (d) with red and blue color, respectively.
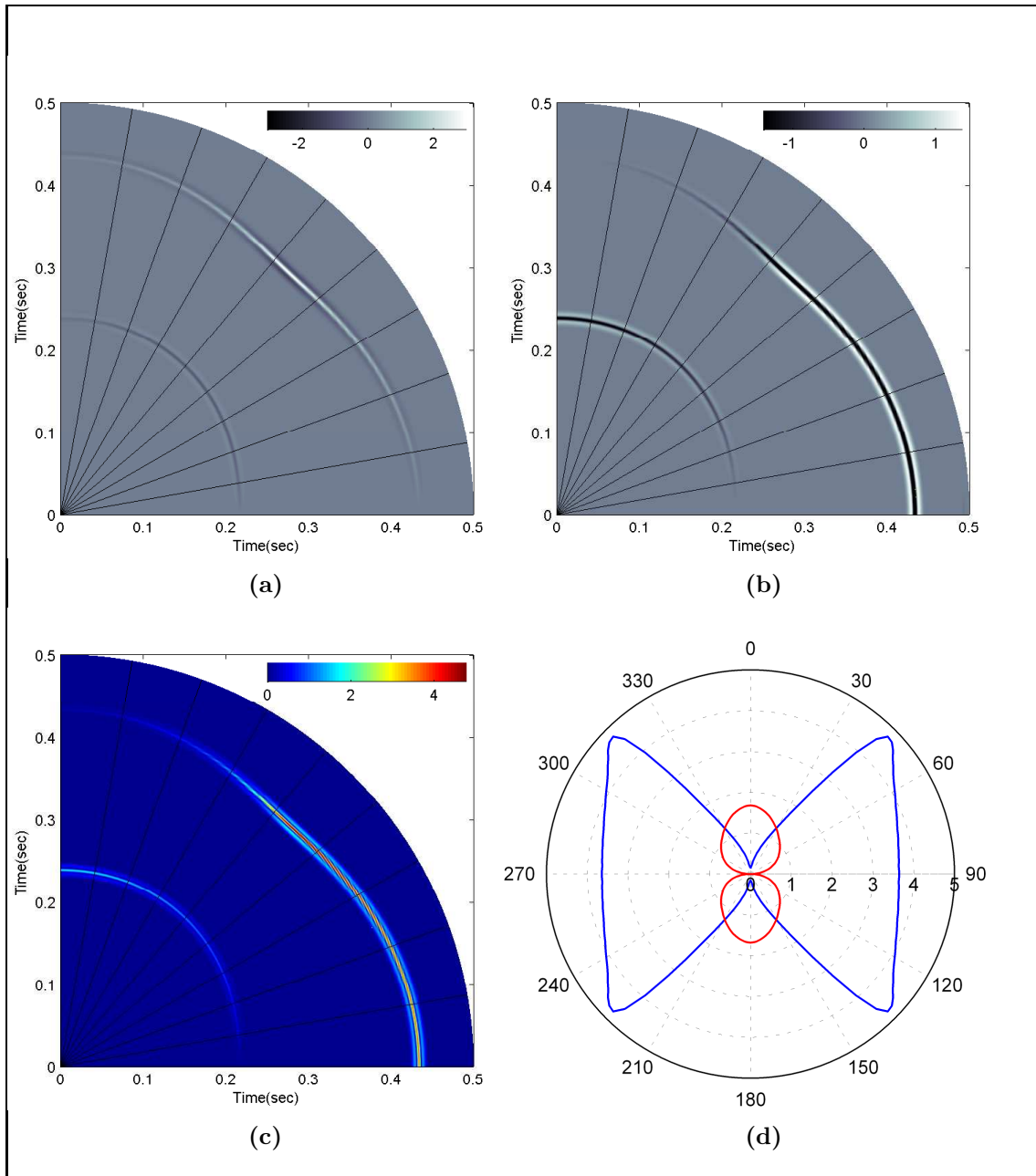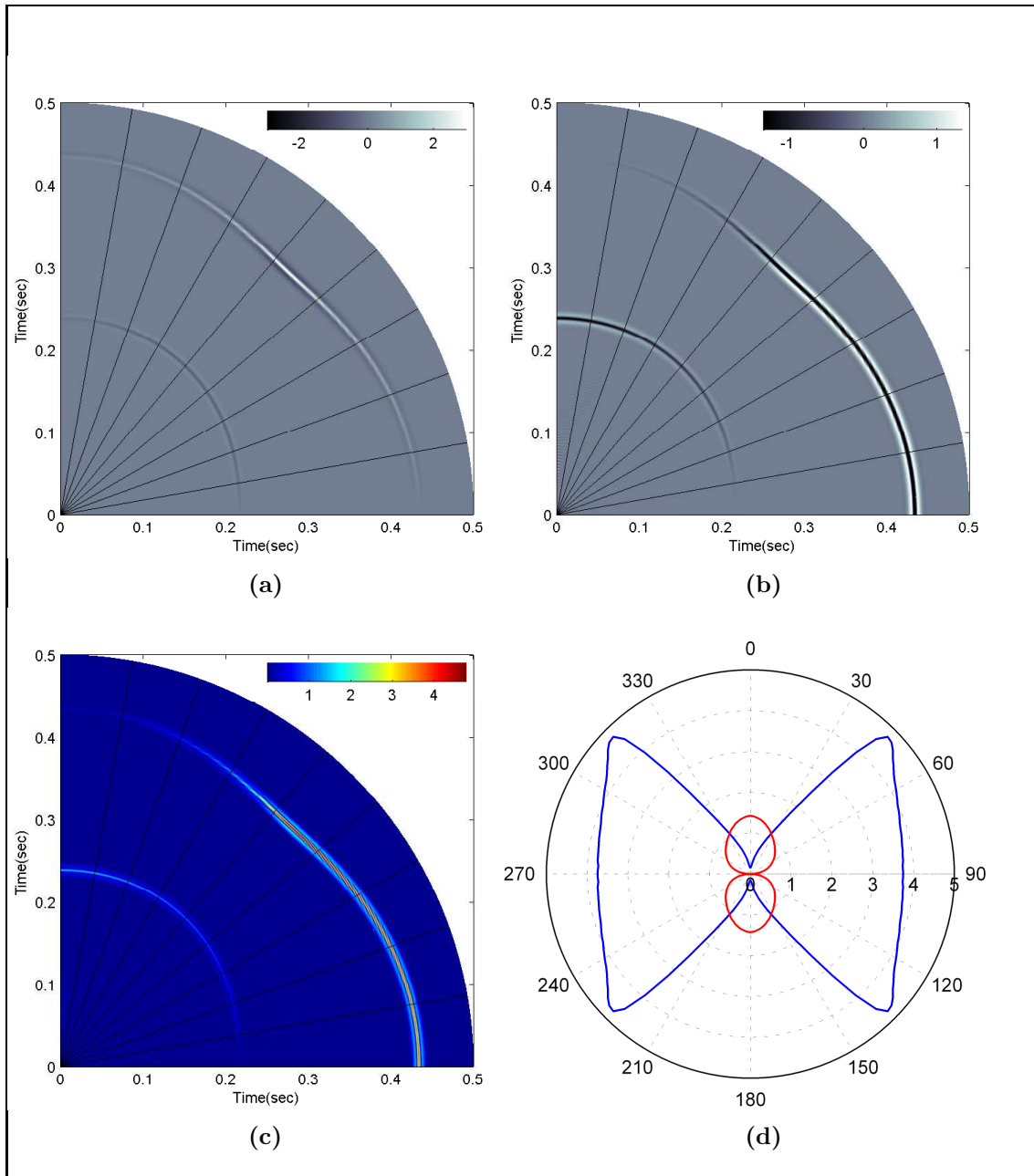
Figure 8.16: Attenuation parameter Q is 5000. X- and Z-components of the synthetic seismograms are shown in (a) and (b), respectively. Absolute value of the displacement amplitude is shown in (c). Radiation patterns of P- and S-waves are shown in (d) with red and blue color, respectively.
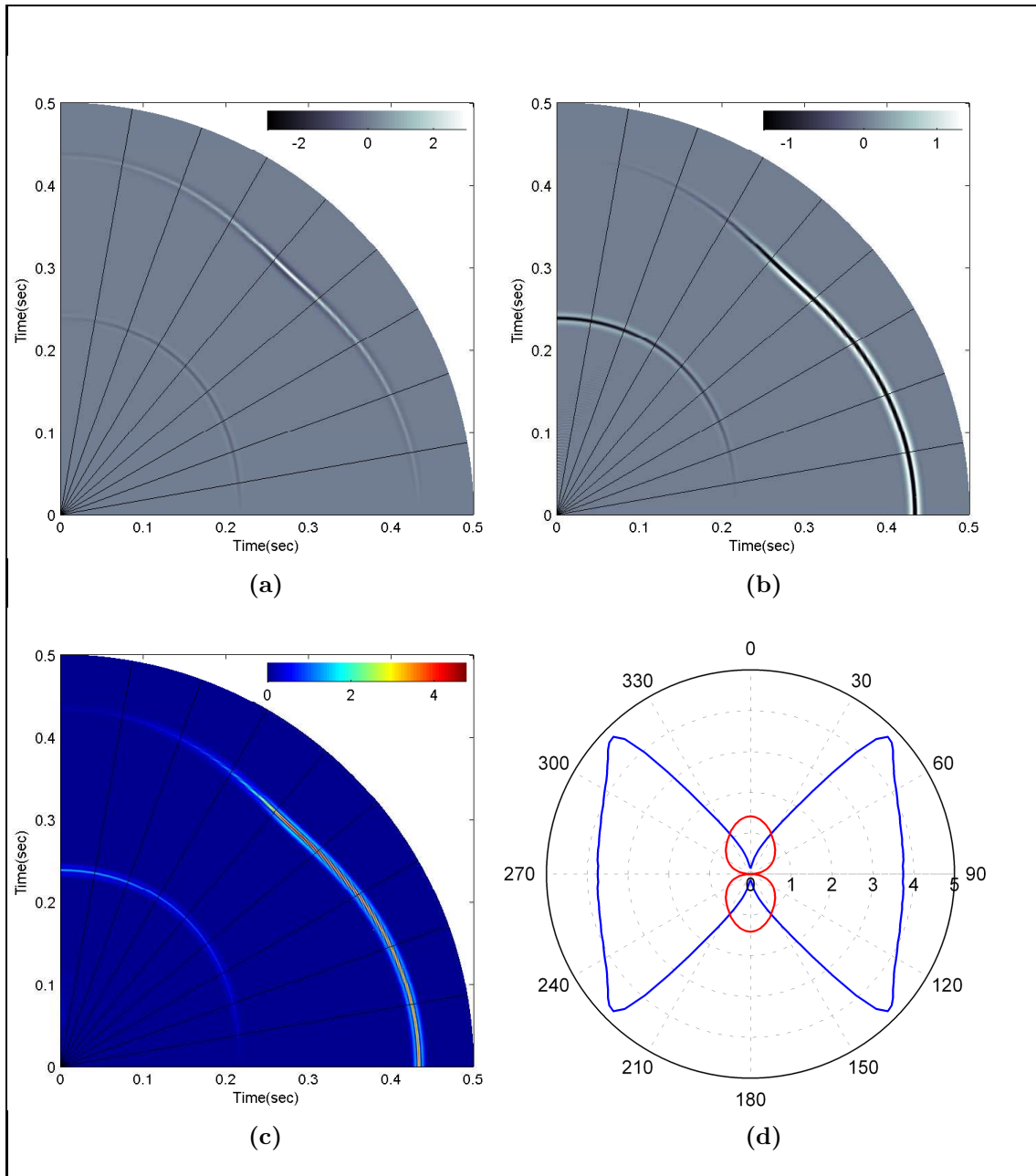
Figure 8.17: Attenuation parameter Q is 10000. X- and Z-components of the synthetic seismograms are shown in (a) and (b), respectively. Absolute value of the displacement amplitude is shown in (c). Radiation patterns of P- and S-waves are shown in (d) with red and blue color, respectively.
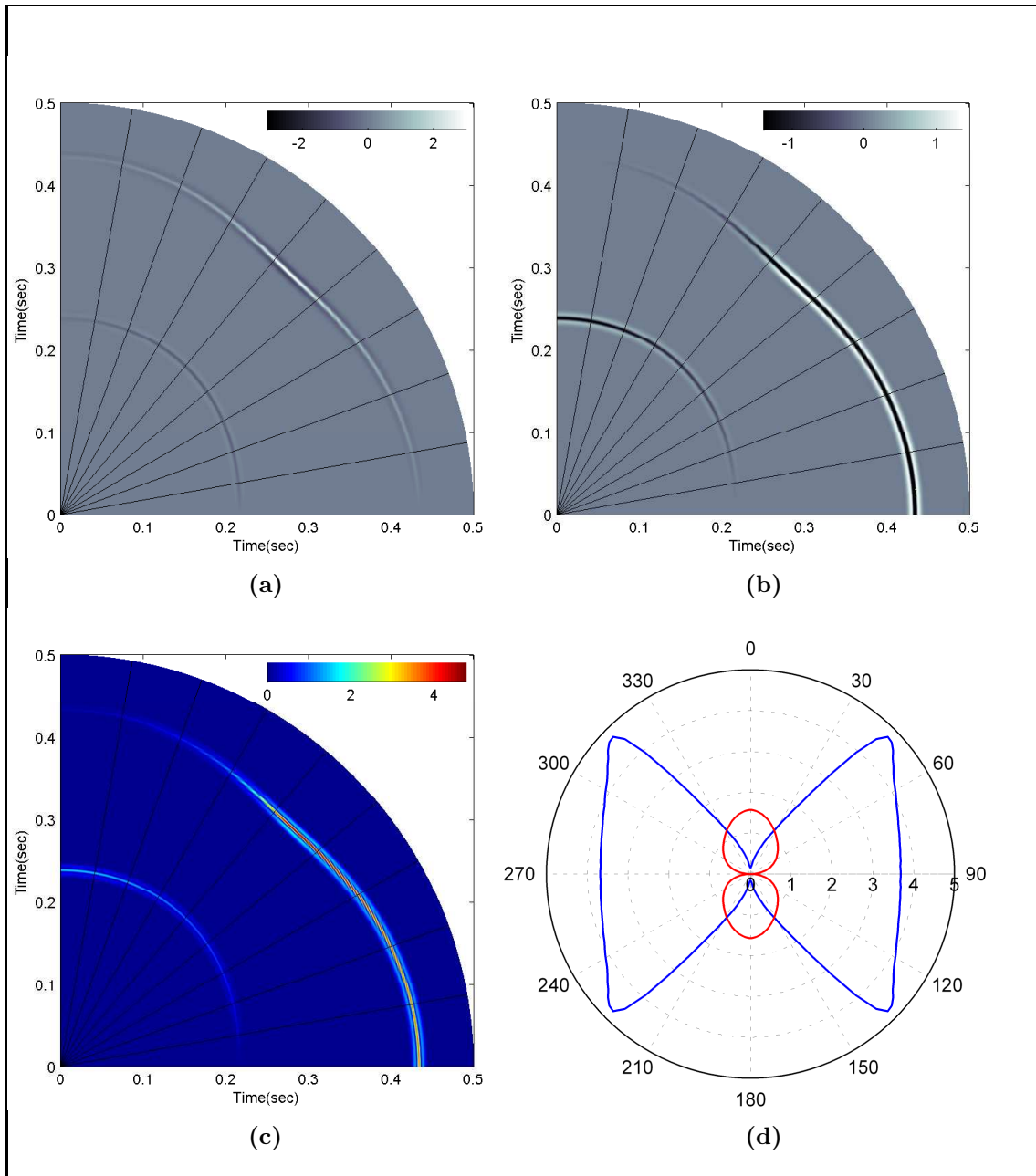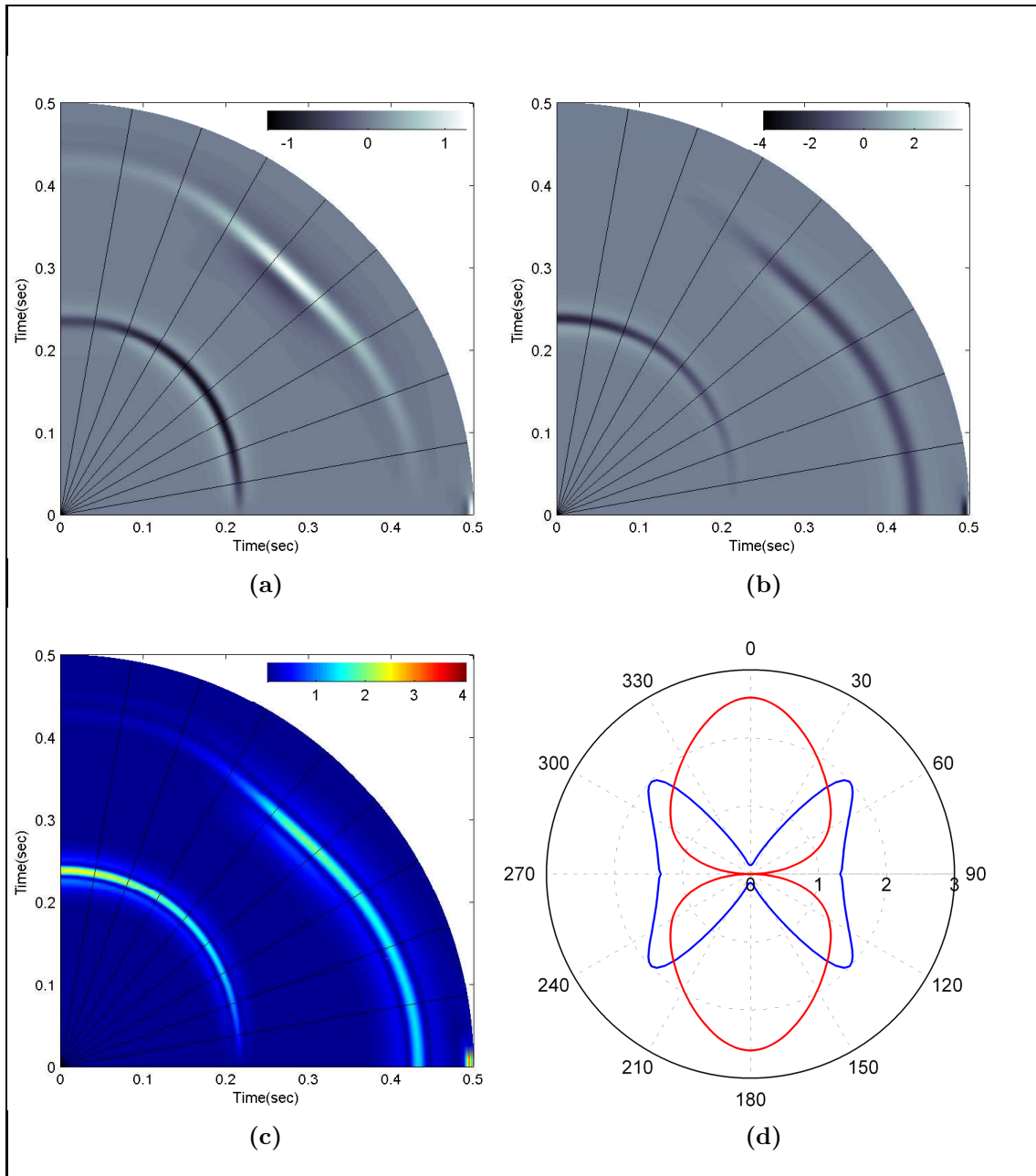
Figure 8.18: Attenuation parameter Q is 10. X- and Z-components of the synthetic seismograms are shown in (a) and (b), respectively. Absolute value of the displacement amplitude is shown in (c). Radiation patterns of P- and S-waves are shown in (d) with red and blue color, respectively.
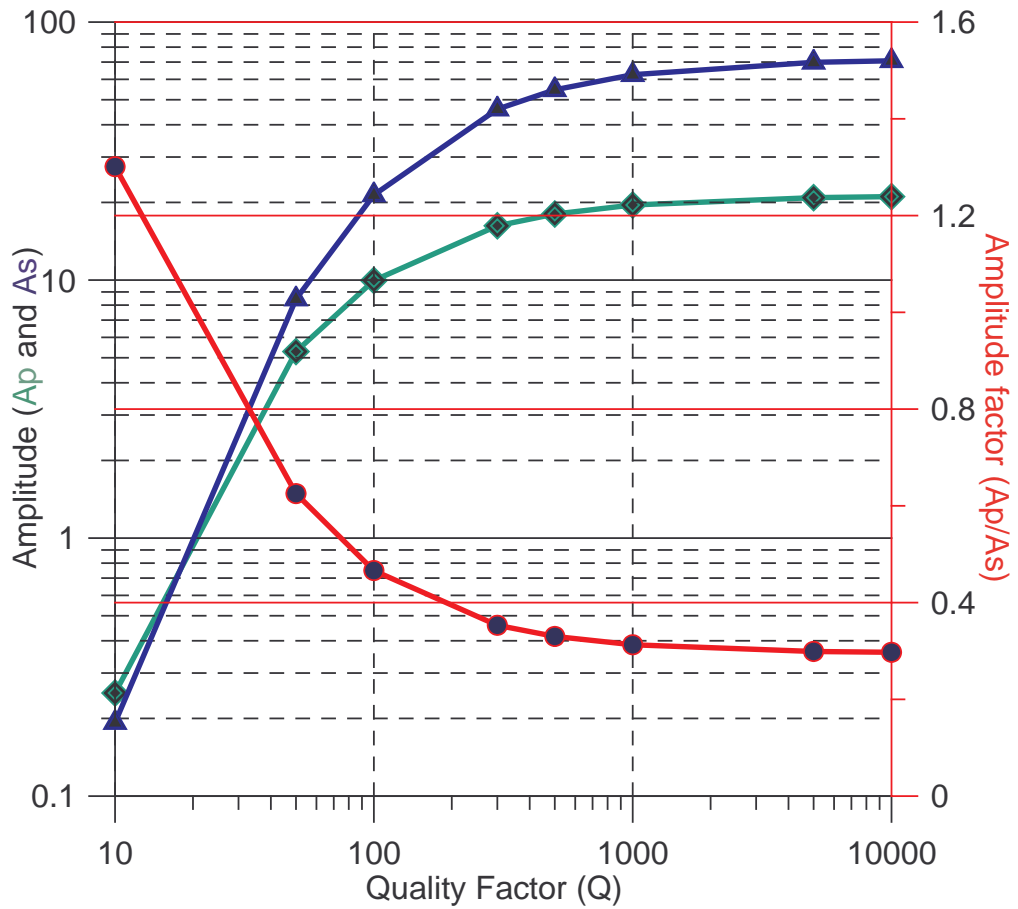
Figure 8.19: Change in P- and S-wave amplitudes with respect to quality factor. Amplitude factor is the ratio of P- and S-wave amplitudes.

In this section, the effects of attenuation on P- and S-waves amplitudes in a homogeneous anisotropic medium are examined. This understanding of amplitude attenuation will be applied to interpret full waveform synthetic seismograms in a multilayered anisotropic medium. In addition to this, effects of attenuation on frequency will also be analyzed using spectral decomposition.

8.4   Multilayered VTI Media

In this section, a point source in a multilayered viscoelastic anisotropic media is examined via a series of downhole multicomponent receivers. This is the same type of recording geometry used in micro-earthquake studies of hydraulic fracturing (Fehler et al., 2001). From here onwards, this geometry will be referred to as micro-earthquake seismic profile (MESP). Motivation for this study comes from the fact that such MESP profiles are often generated during hydraulic fracturing of shaly reservoirs, which have a varying degree of attenuation. Irrespective of their attenuation mechanisms, shales are assigned different values of Q to study amplitude and frequency characteristics of the synthetic seismograms.

A simple model of one layer VTI shale sandwiched between two VTI half spaces is considered. As shown in the schematic diagram (Figure 8.20), the VTI shale layer is 300 m thick. A vertical string of 96 channel multi-component receivers spread over 600 m, symmetrically apart above and below the source level, is placed 300 m away from the source. The source is situated equidistant from the upper and lower interface.

In this modeling, only two types of elastic coefficients for shales are considered: Type I - low velocity shale and Type II - high velocity shale. These shales have been considered for modeling reflection coefficients in previous chapters. Their elastic constants and phase velocity behaviors of various wave types are shown in figures 8.21 and 8.22. Multi-component MESPs are generated for four models having vertical and inclined force vectors and varying Q. These models are M1, M2-100, M2-10, M3 as listed in Figure 8.20.
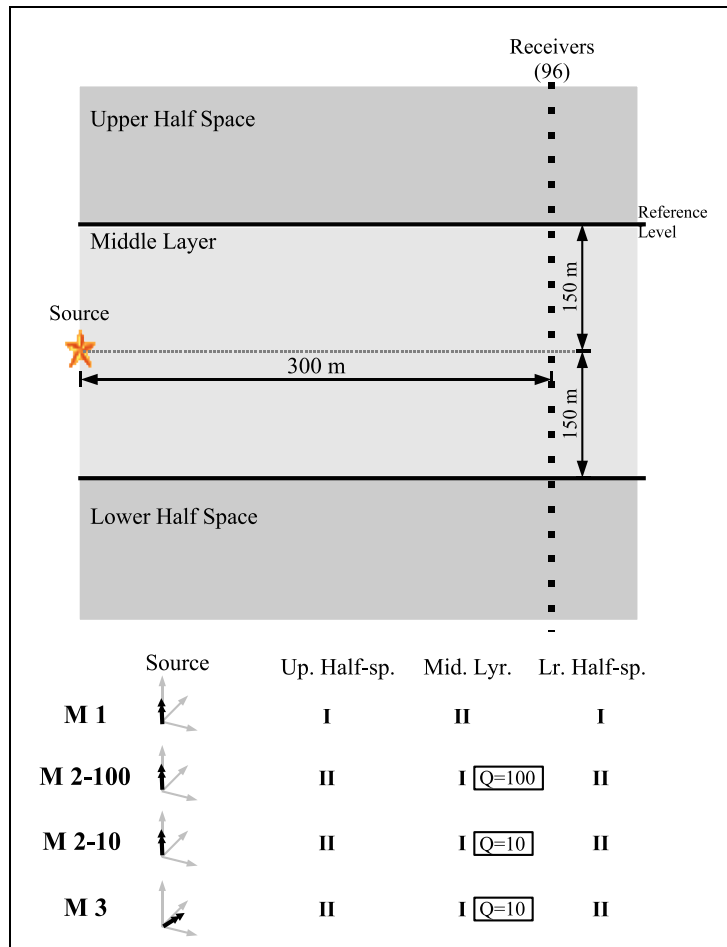
Figure 8.20: A schematic diagram showing a multilayered VTI model for the synthetic seismogram experiment with various orientations of a point force. There are 96 channel multi-component receivers to produce MESPs. Four models, namely M1, M2-100, M2-10 and M3, are generated by changing the orientation of force vector (i.e. source), the rock type (I and II), and the attenuation parameter Q.

$$C_{IJ} = \begin{pmatrix} 21.26 & 3.28 & 6.97 & 0 & 0 & 0 \\ 3.28 & 21.26 & 6.97 & 0 & 0 & 0 \\ 6.97 & 6.97 & 17.63 & 0 & 0 & 0 \\ 0 & 0 & 0 & 5.32 & 0 & 0 \\ 0 & 0 & 0 & 0 & 5.32 & 0 \\ 0 & 0 & 0 & 0 & 0 & 8.99 \end{pmatrix} \text{GPa}, \quad \rho = 2.34 \text{ gm/cc}$$

(a)

(b)

(c)

Figure 8.21: Model VTI Type I: (a)Elasticity tensor (b)P-wave velocity (c)S-wave velocity (SH (blue), SV (green)).

$$C_{IJ} = \begin{pmatrix} 59.40 & 20.0 & 15.82 & 0 & 0 & 0 \\ 20.0 & 59.40 & 15.82 & 0 & 0 & 0 \\ 15.82 & 15.82 & 42.42 & 0 & 0 & 0 \\ 0 & 0 & 0 & 15.27 & 0 & 0 \\ 0 & 0 & 0 & 0 & 15.27 & 0 \\ 0 & 0 & 0 & 0 & 0 & 19.7 \end{pmatrix} \text{GPa}, \quad \rho = 2.37 \text{ gm/cc}$$

(a)

(b)

(c)

Figure 8.22: Model VTI Type II: (a)Elasticity tensor (b)P-wave velocity (c)S-wave velocity (SH (blue), SV (green)).
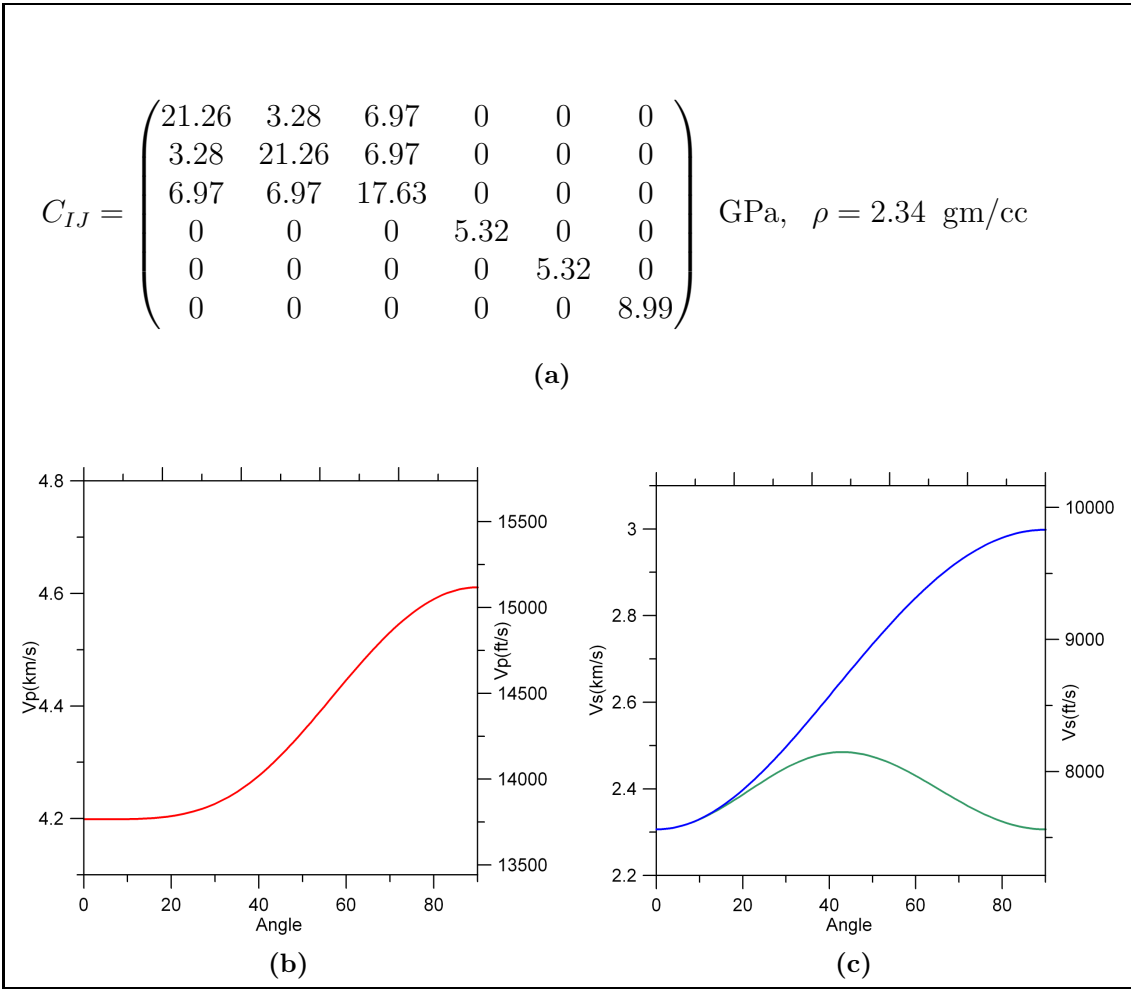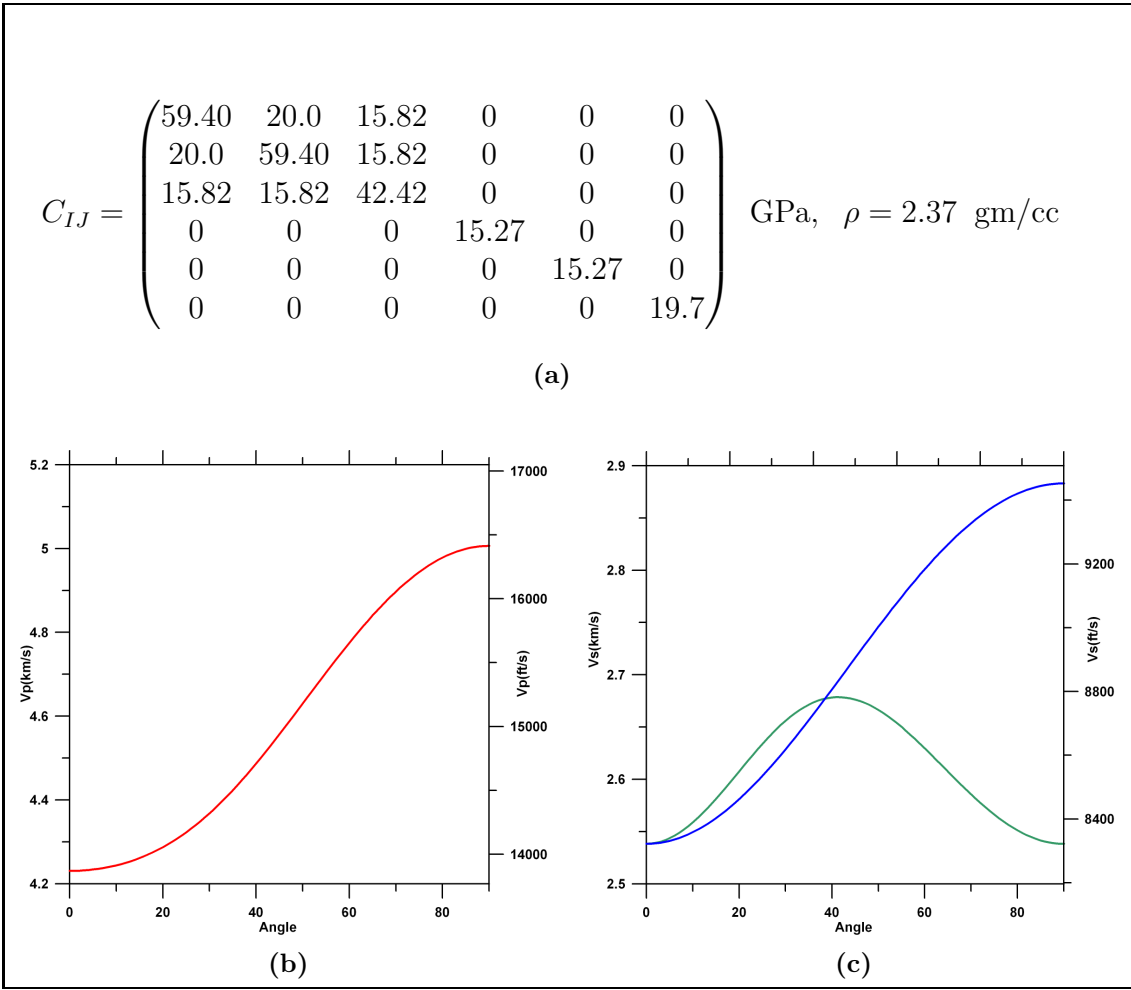
In the model M1, the sandwiched layer is a high velocity layer. The multilayered medium is non-attenuating. We observe all possible reflected, refracted and converted waves. S-waves shown in Figures 8.23 and 8.24 are of the SV-type. Since vertical force is applied in this VTI medium, it does not produce SH-waves. Amplitudes and the associated phase of P- and S-waves are consistent with the explanation given in Section 8.2. Note that there is total absence of the radial component of P- and S-waves in the source plane, and the S-wave lightens up in the vertical component.

While keeping the force vector vertical, shale layers are interchanged in the next model M2-100 such that the sandwiched layer has low velocity. This model is important from a seismic exploration point of view because hydrocarbon reservoirs are generally low velocity zones trapped between high velocity layers. A Q value of 100 is assigned to the sandwiched layer. Radial and vertical components of the MESP synthetic for this model are shown in Figures 8.25 and 8.26. Note that the head waves (HW) appear in the MESP. A necessary condition for a head wave to appear is that the wave propagates in a low velocity layer with a bounding high velocity zone.

Keeping everything the same from the previous model but the value of Q, a new model is created. The idea here is to examine the effect of changing attenuation. This change in attenuation could be due, for example, to producing a shaly reservoir or changing fluid saturation between shale layers by injecting fluids in the reservoir. Change in attenuation is modeled by altering the value of Q. In the model M2-10, Q is assigned a value of 10, i.e. the sandwiched layer is now more attenuating. Radial and vertical components of the synthetic MESP for this model are shown in Figures

114

8.27 and 8.28. Note that the wavelet shapes and amplitudes of P- and S-wave types have changed. Comparison of Figures 8.25 and 8.27 reveals that the radiation energy has shifted from S-wave to P-wave. This is in consistent with the findings in Section 8.3.

In the next model, the force direction is changed such that it is inclined to the vertical direction and off the X-Z plane. In fact, the force vector used in this case is [1.0,1.0,0.2]. This force vector is close to the horizontal plane. The basic idea here is to record the SH-wave and its reflection and refraction. All three components of the synthetic MESP for this new model M3 are shown in Figures 8.29, 8.30 and 8.31. Reflection and refraction of SH-waves are simple as no conversion of the wavetype was involved. Note that the P-wave energy on the radial component is very high, due to the fact that the force vector is close to the horizontal plane.

Figure 8.23: Synthetic MESP showing the radial component of polarization vectors for model **M1**.

Figure 8.24: Synthetic MESP showing the vertical component of polarization vectors for model **M1**.

Figure 8.25: Synthetic MESP showing the radial component of polarization vectors for model **M2-100**.
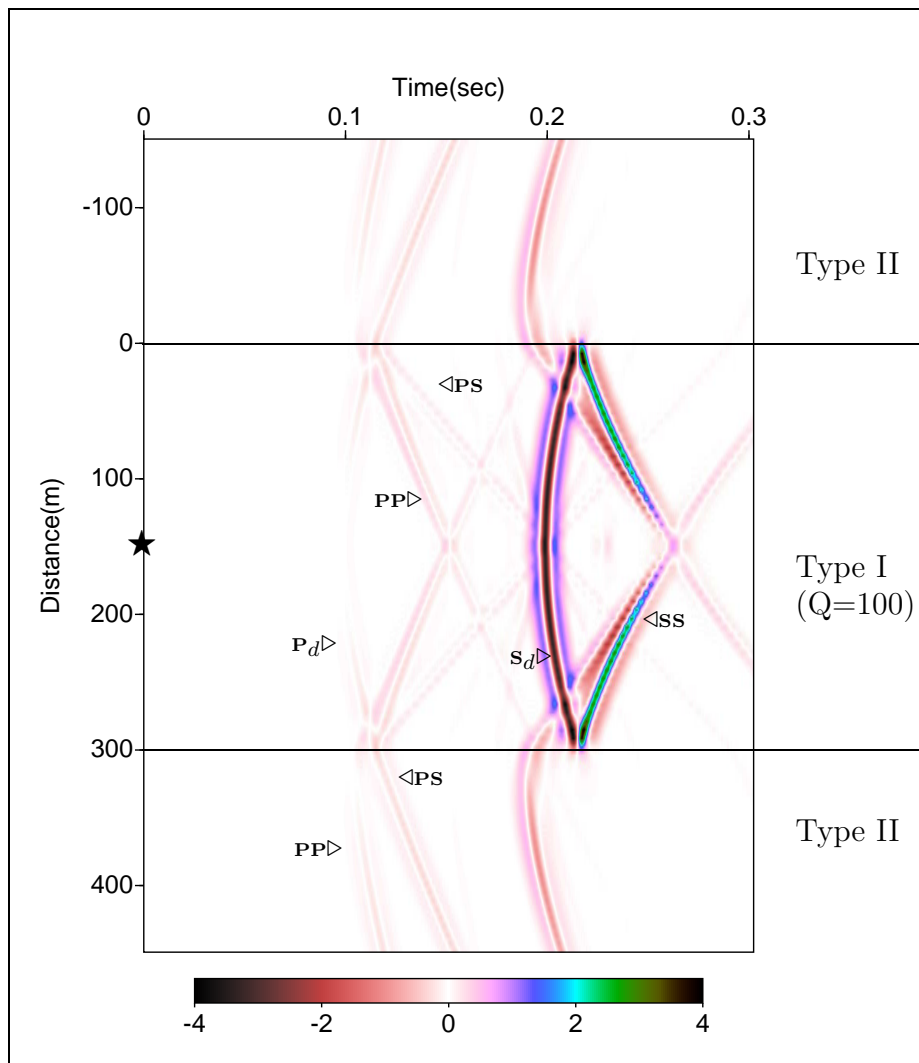
Figure 8.26: Synthetic MESP showing the vertical component of polarization vectors for model **M2-100**.
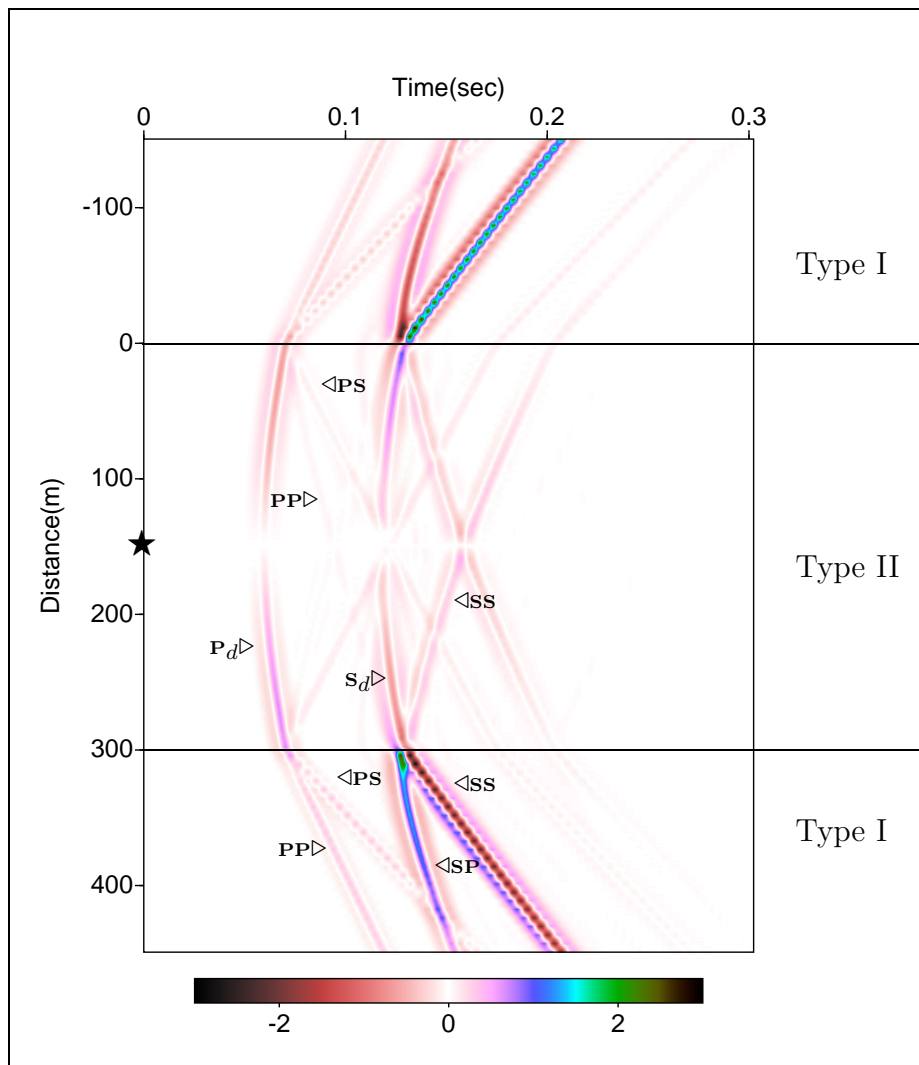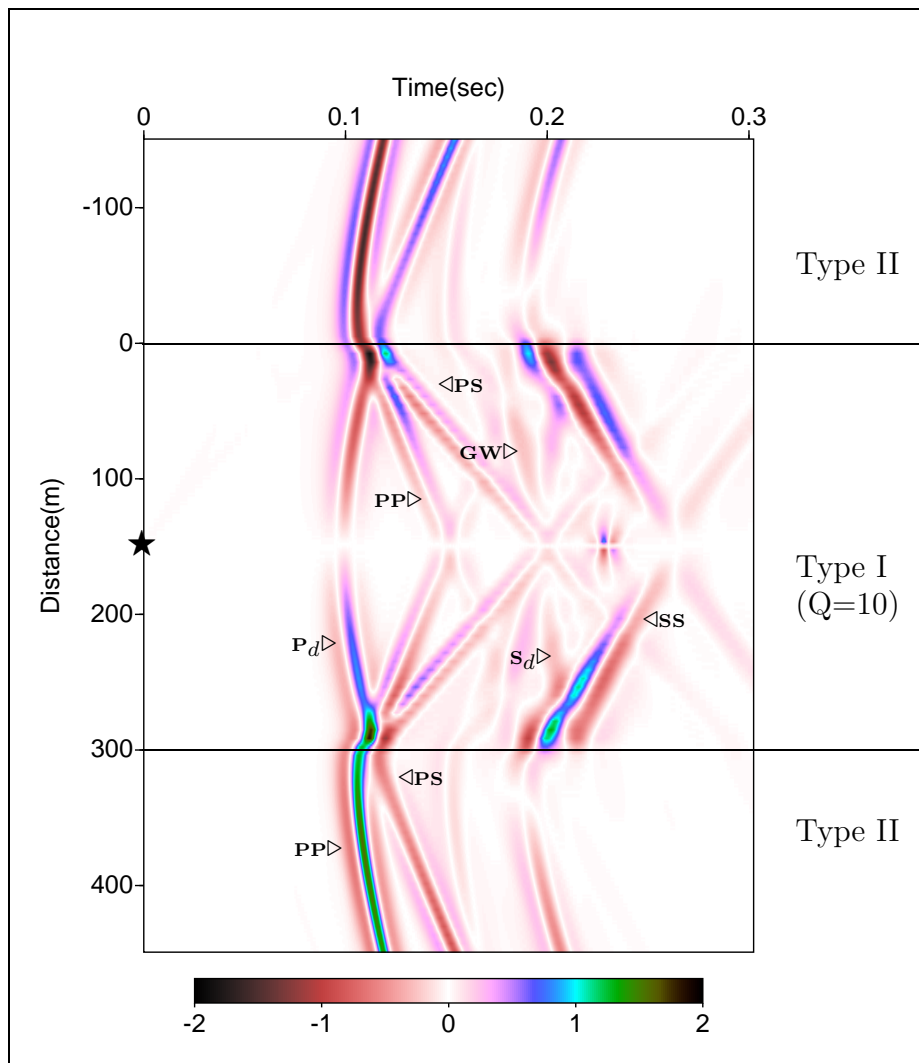
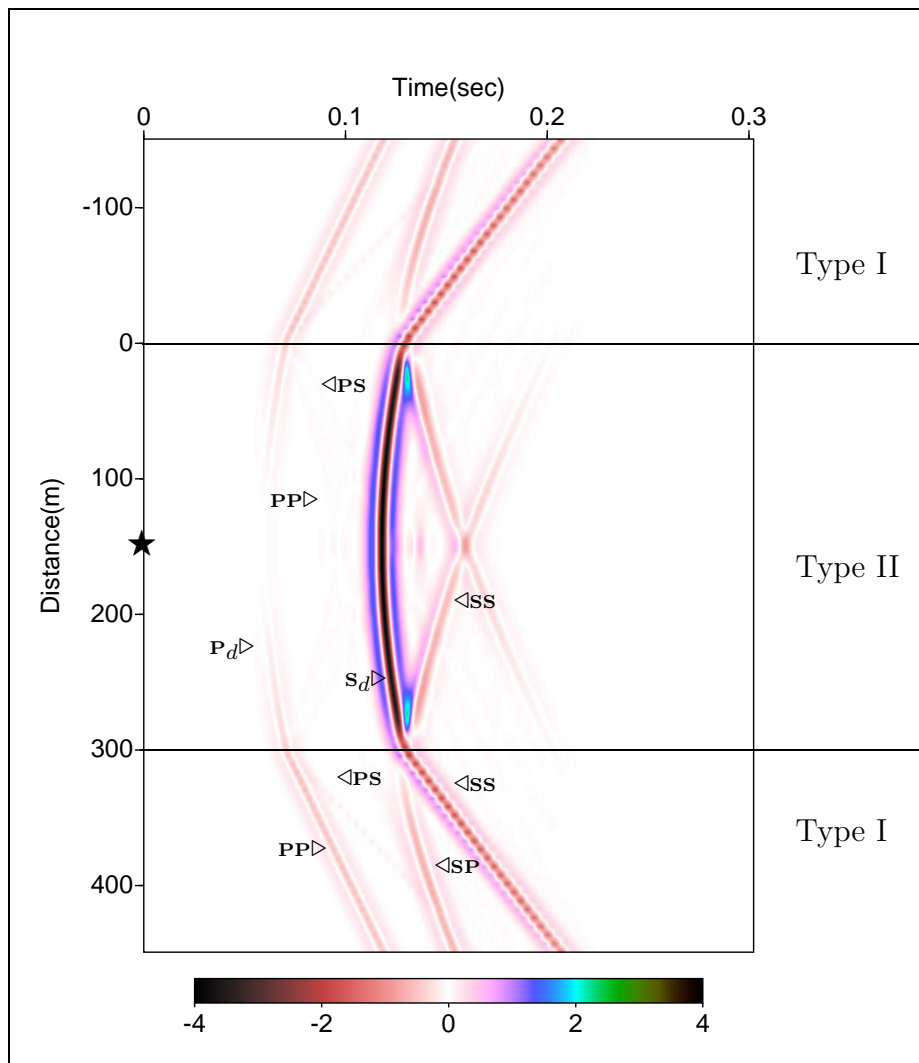Figure 8.27: Synthetic MESP showing the radial component of polarization vectors for model **M2-10**.
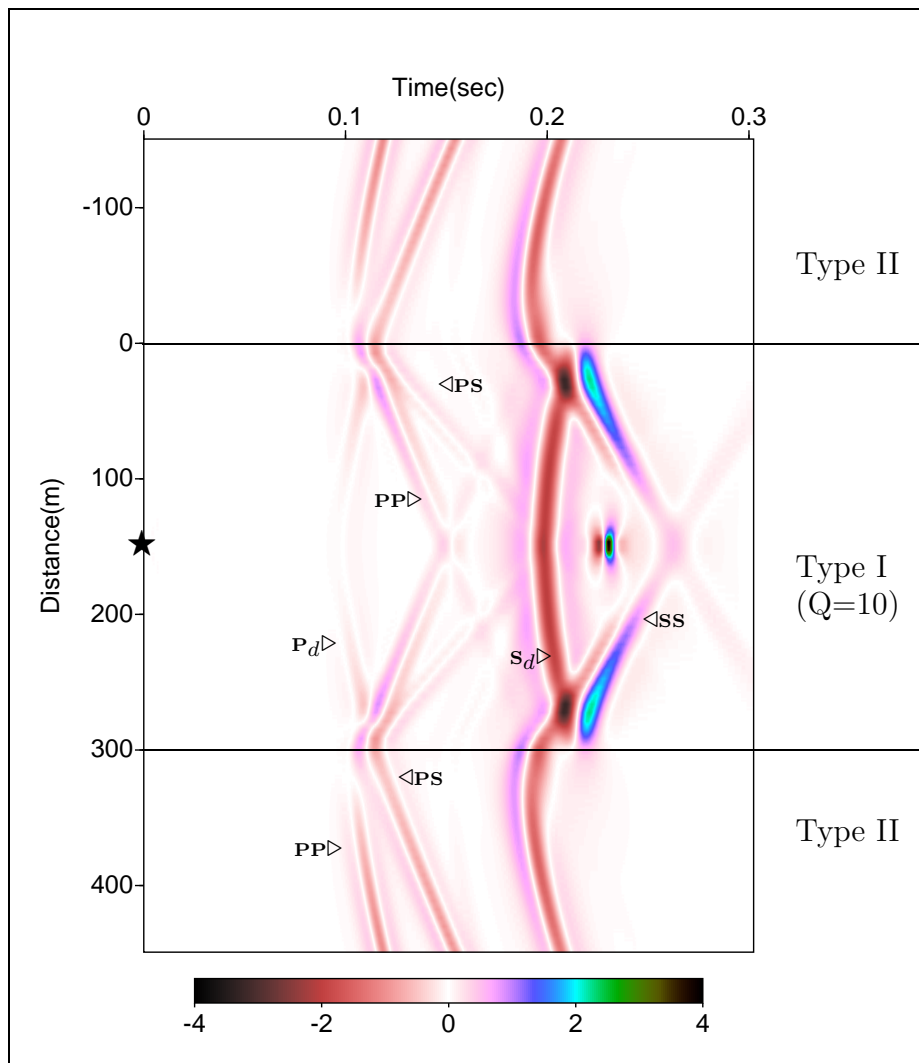
Figure 8.28: Synthetic MESP showing the vertical component of polarization vectors for model **M2-10**.

Figure 8.29: Synthetic MESP showing the radial component of polarization vectors for model **M3**. Force vector is inclined from the vertical and out of the X-Z plane.
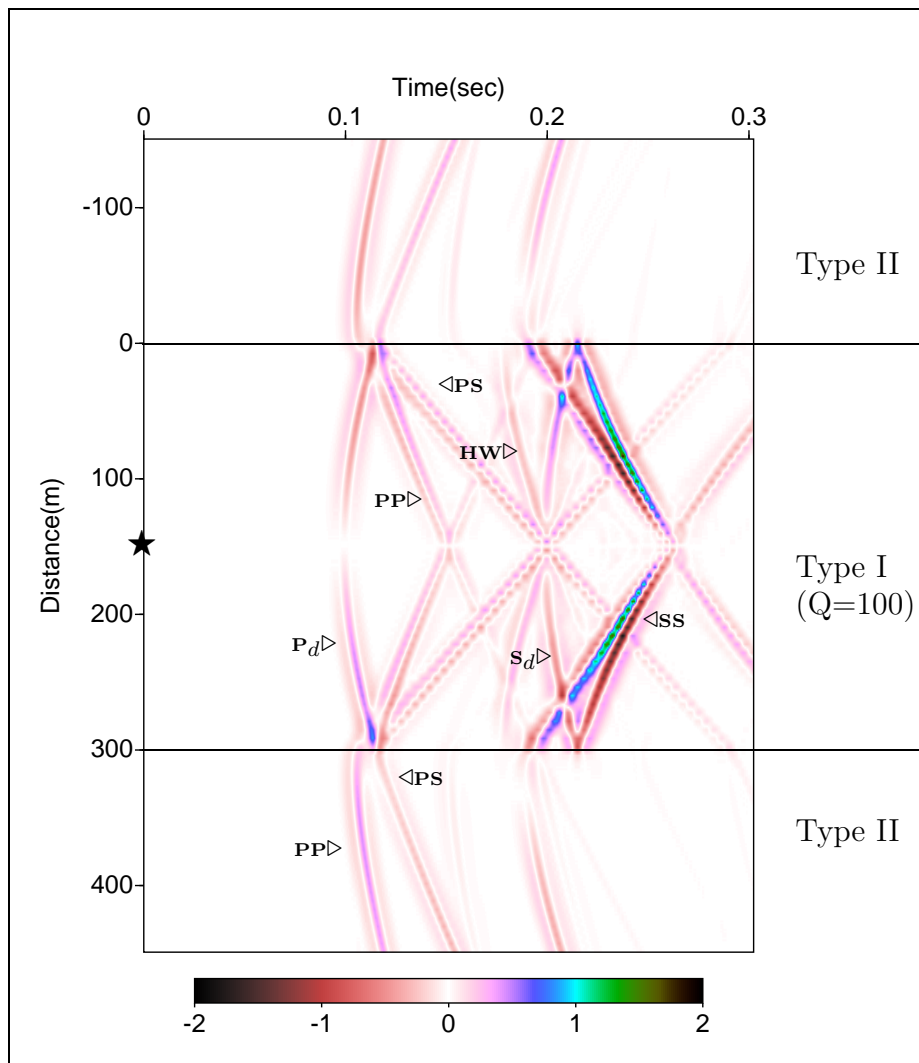
Figure 8.30: Synthetic MESP showing the transverse component of polarization vectors for model **M3**. Force vector is inclined from the vertical and out of the X-Z plane.

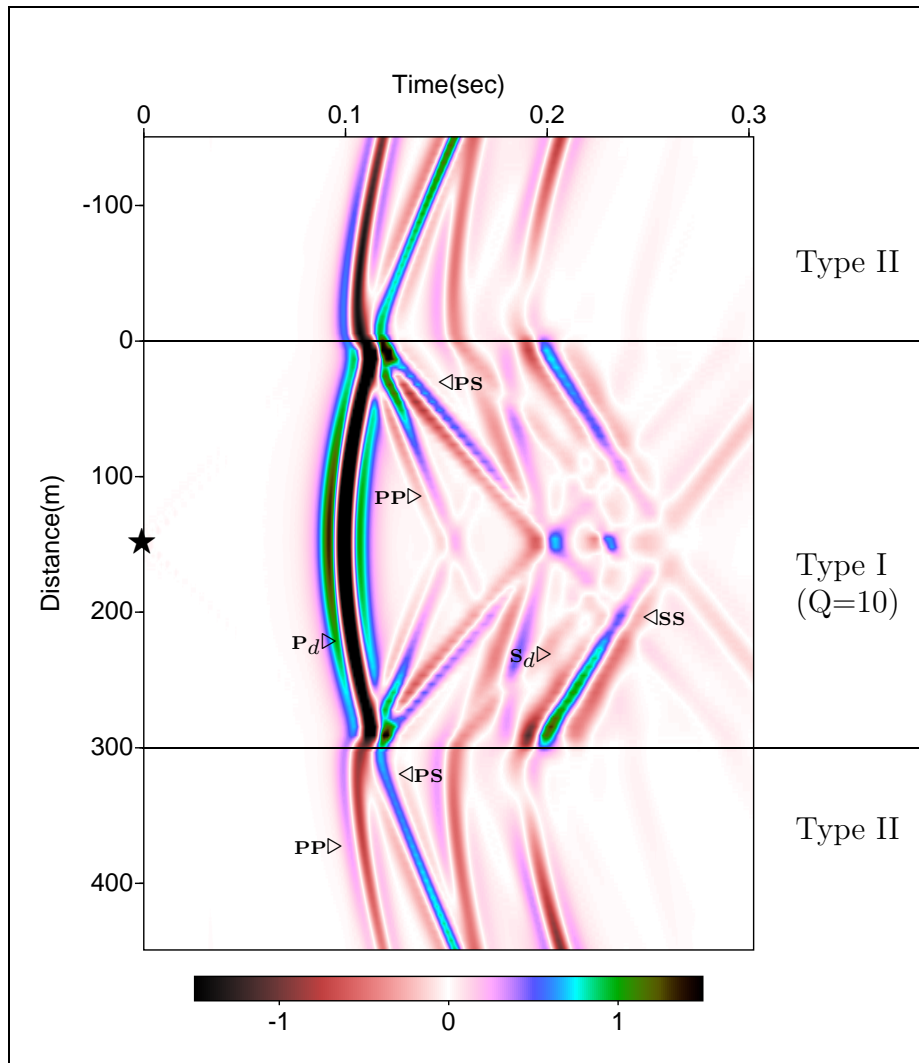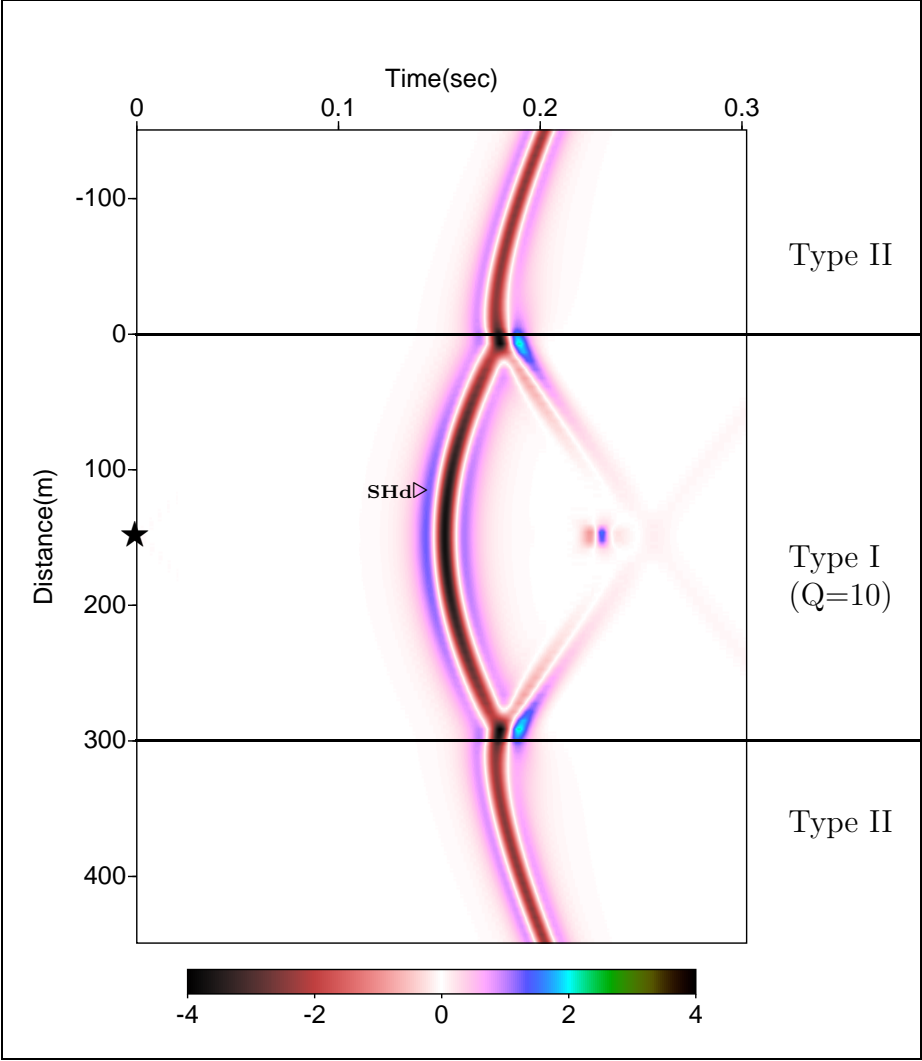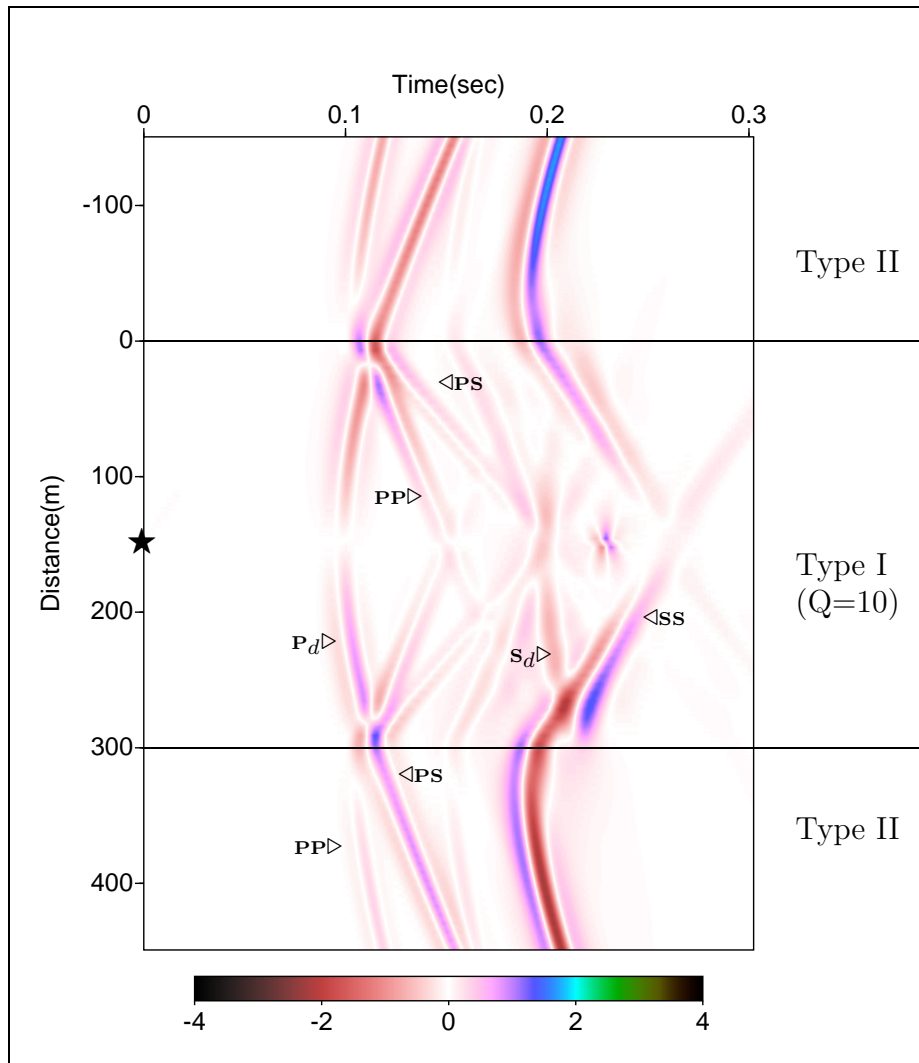Figure 8.31: Synthetic MESP showing the vertical component of polarization vectors for model **M3**. Force vector is inclined from the vertical and out of the X-Z plane.

8.5 Effects of Attenuation on Spectral Characteristics of Synthetic Seismograms

In the previous section, the synthetic MESPs from models M2-100 and M2-10 suggested that attenuation could change the wavelet shapes of P- and S-waves and redistribute their energies. In this section, spectral decomposition is utilized to study both aspects (i.e. wave shapes relating to frequency and energy related to wave amplitude) of the full waveform synthetic in attenuating media.

For this purpose, the spectral decomposition technique, based on continuous wavelet transform called TFCWT (Sinha et al., 2005), is utilized. It is noted in the above-referenced article that the TFCWT method is best-suited for seismic data analyses. This method has already been applied to detect attenuation due to hydrocarbon reservoirs from the real seismic data. The Morlet wavelet (Morlet et al., 1982) is used here for the spectral decomposition because it has a good time-frequency resolution.

For the spectral analysis of synthetic seismograms, two traces are chosen: the first one is from the synthetic MESP of M2-100 and the second from the synthetic MESP of M2-10; both are from the same receiver placed within the sandwiched layer. These traces are plotted in figure 8.32a. A spectral decomposition map of trace 1 is plotted in Figure 8.32b and partly enhanced (between 0 and 0.18 sec) to plot as 8.32c to show the range of frequency content. A spectral decomposition map for trace 2 is plotted in Figure 8.32d. Note that for Q values of 100 and 10, the dominant frequency is around 100 Hz and 50 Hz, respectively, as shown by arrows frequency axes in Figures 8.32c and 8.32d. The interpretation here is that

as attenuation increases (i.e. Q decreases), dominant frequency of the seismogram decreases. Furthermore, by comparing Figures 8.32b and 8.32d, we can say that radiation energy shifts from S wave to P wave as attenuation increases.

8.6 Summary

The full waveform method is successfully implemented in elastic and viscoelastic, homogeneous and multilayered anisotropic media to generate synthetic seismograms for various orientations of sources. Radiation patterns in the VTI media are explained in light of radiation patterns in isotropic media. It is found that P- and S-wave radiation patterns are affected by the attenuation in the viscoelastic media, and it has the technological potential in hydrocarbon exploration. Not only are the amplitudes affected, but also frequency contents of all wave types are modified by the attenuating media. Implementation of the spectral decomposition of the synthetic seismograms in viscoelastic media unfolds the effects of attenuation, in terms of amplitude and frequencies of the seismograms. Thus, spectral decomposition should be extensively utilized as a seismic exploration tool to study attenuation effects on seismic wave patterns.
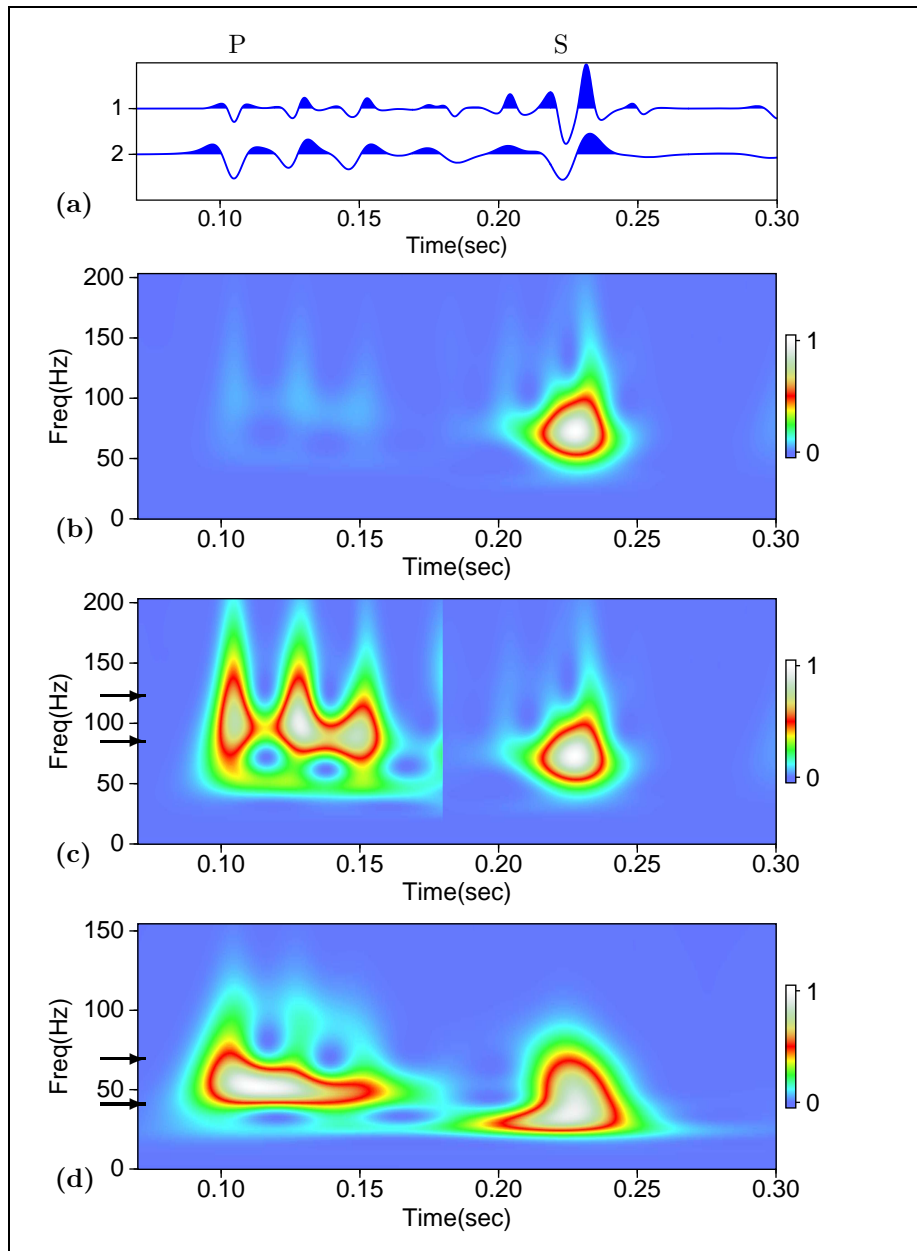
Figure 8.32: (a) Synthetic seismograms for 100Q(1) and 10Q(2) (b)Spectral decomposition of trace 1 and partly enhanced in between 0 and 0.18 sec(c). (d) spectral decomposition of trace 2.

127

Chapter 9

Shale Anisotropy

9.1   Shale Models

Shales are important from the standpoint of hydrocarbon exploration because they form either source rocks or reservoir rocks. Since shales are generally anisotropic, it is important to understand shales from a seismic point of view in order to accurately image the subsurface. The nature of anisotropy varies from one shale to another. Anisotropy in shales can be caused by the following reasons.

1. preferred orientation of clay minerals

2. orientation of silt minerals - quartz, feldspar, and pyrite. Quartz is the most anisotropic crystal among silt minerals.

3. orientation of cracks

The scope of this work is to investigate seismic anisotropy of shales by constructing synthetic seismograms from point sources in shale models. The following models are considered:

1. Hornby shales: (i) Measured, (ii) Predicted: (a)aligned clay particles (b) distributed clay particles. (Hornby et al., 1994)

2. Non-porous shale vs. porous shale with nearly spherical pores (with 12% porosity).

3. Clay particles are aligned and other minerals are randomly oriented. Cracks are aligned along clay minerals.

   - Gas saturated cracks; aspect ratio of cracks: 0.03 and 0.1; porosity varying from 0.5 to 4%

   - Water saturated cracks; aspect ratio of cracks: 0.03 and 0.1; porosity varying from 0.5 to 12%

4. All minerals including clay particles are randomly oriented. Cracks have preferred orientation.

   - Gas saturated cracks; aspect ratio of cracks: 0.03; porosity varying from 0.5 to 4%

   - Water saturated cracks; aspect ratio of cracks: 0.03; porosity varying from 0.5 to 4.0%

These models are created to show the anisotropy effects of clay orientation, the crack's aspect ratio, fluid types, porosity and various combination of these parameters on the synthetic seismograms. The General Singular Approximation (GSA) method is used to model shales theoretically (Bayuk and Chesnokov, 2000). The above descriptions of the models do not essentially correspond to the arrangement

of the models shown in Table 9.1. The next section presents the detailed analyses of each model shown in Table 9.1 in terms of synthetic seismograms and velocity behavior of P and S waves.

9.2   Synthetic Seismograms and Interpretations

All the listed models in Table 9.1 are VTI. Due to symmetricity in a VTI medium, anisotropy is observed only in the vertical plane and not in the azimuthal plane. For all the models, full waveform synthetic seismograms are generated in the X-Z plane for angles of propagation ranging from 0 to 90 degrees. Figures, such as 9.1-a, show arrival times for P, SH, and SV waves from the receivers distributed radially from the source in the vertical plane X-Z. Color represents displacement amplitude of various wave types. The distance between source and receivers are adjusted so that P- and S-wave arrivals could be shown on the same figure.

The following can be interpreted from the modeling:

1. Figure 9.1 shows synthetic seismograms for Hornby shale models (Model 1-a, b and c in Table 9.1). It appears that the cusps on the SV wave surface become stronger with clay plate alignment. Comparison of the three models suggests that the real shale has only a fraction of clay platelets aligned. The development of cusps gives rise to more than two S-wave arrivals in certain directions.

2. When nearly spherical pores are introduced in a non-porous shale, change in shear wave pattern is insignificant (Figure 9.2). This is due to the fact that

randomly distributed nearly spherical pores do not introduce any order in the medium.

3. Phase velocity characteristics are also dependent on whether the cracks are water saturated or gas saturated. Gas saturated cracks tend to produce a strong anisotropy in the medium. Water saturated cracks develop wide cusps while gas saturated cracks develop small cusps, if any (Figure 9.3).

4. In the case of gas filled cracks, the maximum change in P- and S-wave velocities are observed normal to the cracks. By comparing Figures 9.4 and 9.5, it is evident that the change in aspect ratio has a pronounced effect on P- and SV-wave velocity anisotropy (i.e. the amount of anisotropy) in case of gas-filled cracks, whereas the anisotropy pattern (e.g. cusps) is modified in the case of water-filled cracks.

5. In a model with a constant aspect ratio of flat cracks, porosity is increased or decreased by increasing or decreasing the fracture density in the model. Due to the change in porosity (hence, fracture density), the maximum change in P- and S-wave velocities are observed perpendicular to the fractures. By changing the porosity in the model, the anisotropy patterns in the case of water-filled cracks are altered more compared to that in the case of gas-filled cracks (Figures 9.6 - 9.9).

6. Cracks have dominant effects as compared to the orientation of clay platelets, on the anisotropy behavior of shales (Figure 9.10).

Model #	C_{11}	C_{33}	C_{55}	C_{66}	C_{13}	ρ	A_r	$\phi(\%)$	Fluid Type
Model 1-a	34.3	22.7	5.4	10.6	10.7	2.3	NA	11	NA
1-b	38.12	16.6	2.95	12.74	8.32	2.3	NA	11	NA
1-c	34.67	22.16	6.02	10.76	11.46	2.3	NA	11	NA
Model 2-a	49.57	38.21	7.72	13.64	7.22	2.59	NA	0	NA
2-b	36.95	29.05	6.29	10.74	5.63	2.28	0.99	12	W
Model 3-a	35.82	13.63	7.5	12.41	5.83	2.59	0.03	0.5	G
3-b	38.19	27.43	7.61	12.42	11.55	2.59	0.03	0.5	W
Model 4-a	35.82	13.63	7.5	12.41	5.83	2.59	0.03	0.5	G
4-b	37.18	21.79	9.44	12.38	9.29	2.59	0.1	0.5	G
Model 5-a	38.19	27.43	7.61	12.42	11.55	2.59	0.03	0.5	W
5-b	38.15	27.55	9.5	12.39	11.65	2.59	0.1	0.5	W
Model 6-a	35.82	13.63	7.5	12.41	5.83	2.59	0.03	0.5	G
6-b	34.82	8.88	5.76	12.34	3.9	2.57	0.03	1.0	G
6-c	33.78	5.2	3.91	12.19	2.4	2.55	0.03	2.0	G
6-d	32.55	2.81	2.36	11.89	1.41	2.5	0.03	4.0	G
Model 7-a	37.74	17.63	8.52	12.28	11.25	2.58	0.1	1.0	W
7-b	35.5	20.41	5.21	11.68	9.42	2.54	0.1	4.0	W
7-c	32.90	15.72	3.35	10.90	7.9	2.47	0.1	8.0	W
7-d	30.57	17.63	2.41	10.17	6.9	2.41	0.1	12.0	W
Model 8-a	33.65	27.36	4.08	11.02	10.2	2.57	0.03	2.0	W
8-b	37.12	23.59	4.04	12.19	10.21	2.57	0.03	2.0	W

Table 9.1: Elastic coefficients, density, aspect ratio of cracks, porosity and fluid type for each theoretical VTI shale model.

Thus, the anisotropy in shales depends on numerous parameters and a few of them are investigated in this study. These are: orientation of clay particles, aspect ratio of cracks, change in porosity and fluid types. Investigation of these models in terms of synthetic seismograms is unique. The development of cusps on the SV wave surfaces should be investigated to avoid pitfalls in the interpretations of real seismograms.
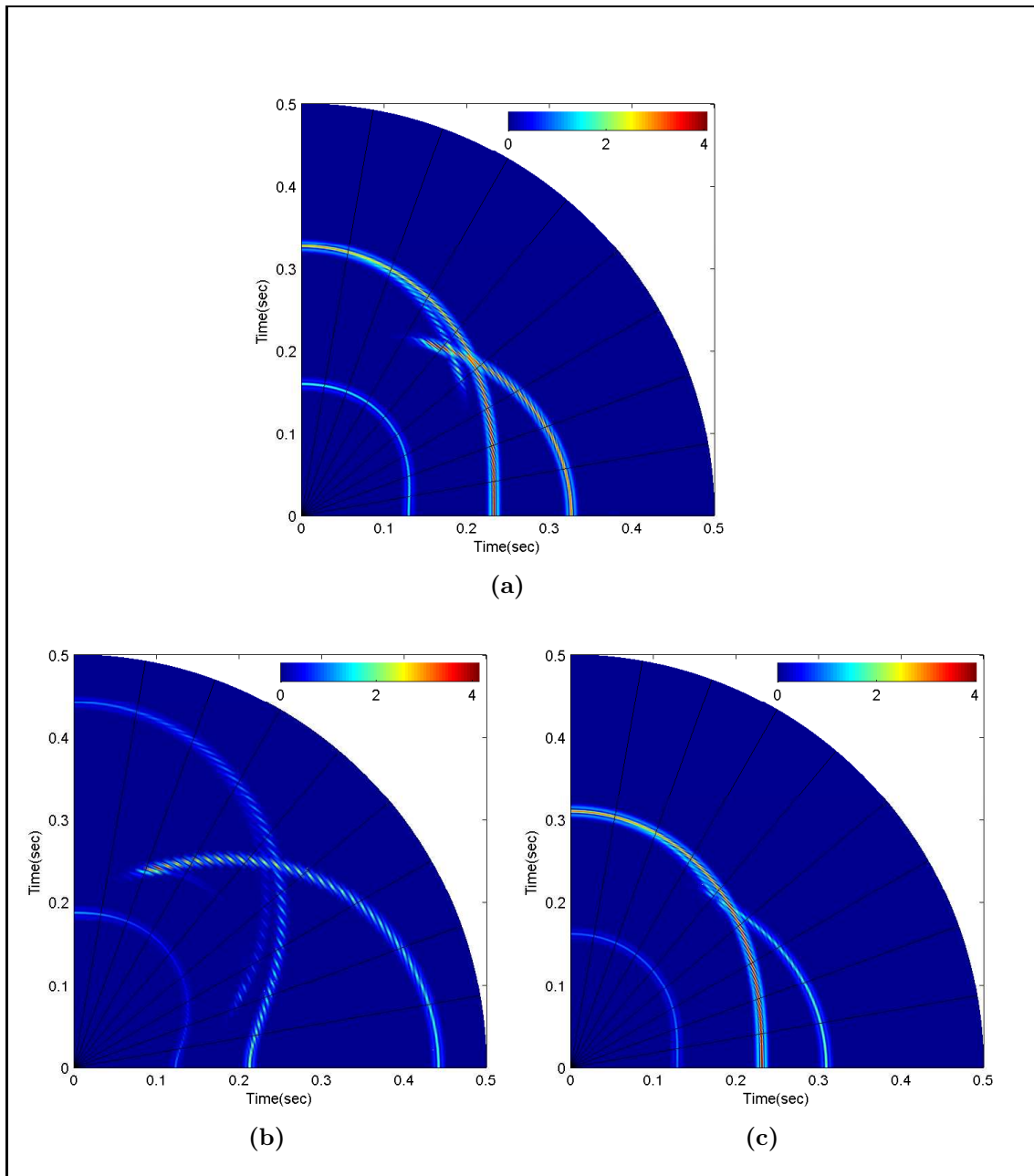
Figure 9.1: Synthetic seismograms for Model 1-a, b and c (Table 9.1). Model parameters are taken from Hornby et al. (1994). These synthetic seismograms are created for (a) measured shale parameters; and, (b) and (c) predicted shale parameters with clay platelets aligned and distributed, respectively. The source-receiver distance for this computation is 500 m.
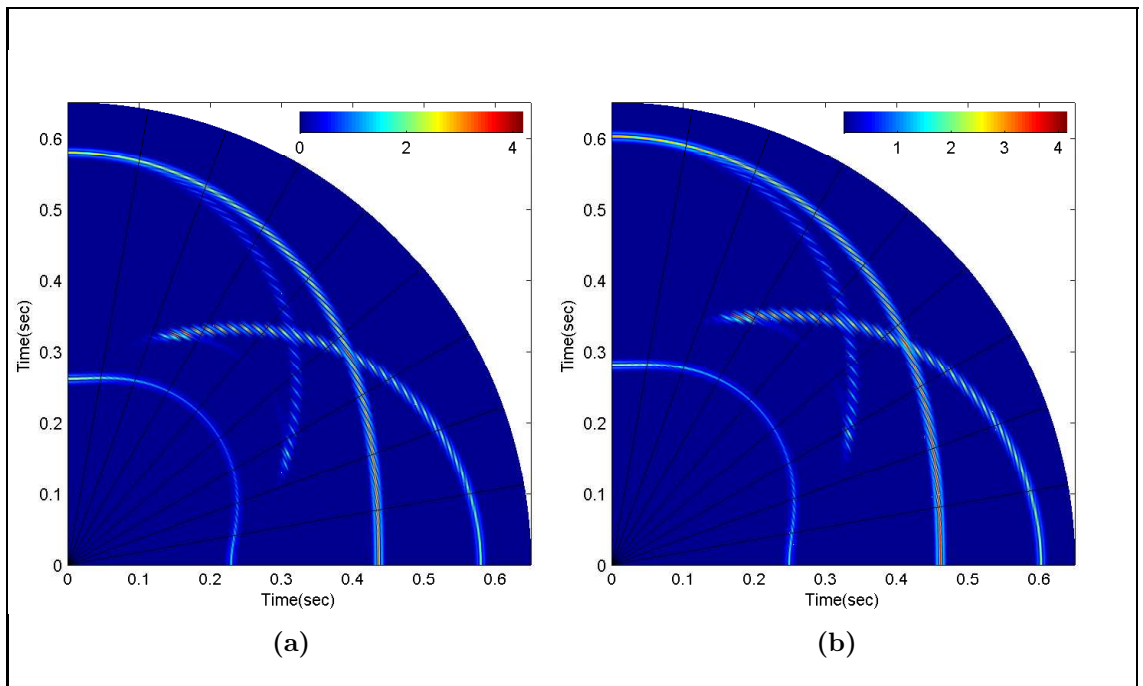
Figure 9.2: Comparison of the synthetic seismograms for (a) porous shale versus (b) non-porous shale.
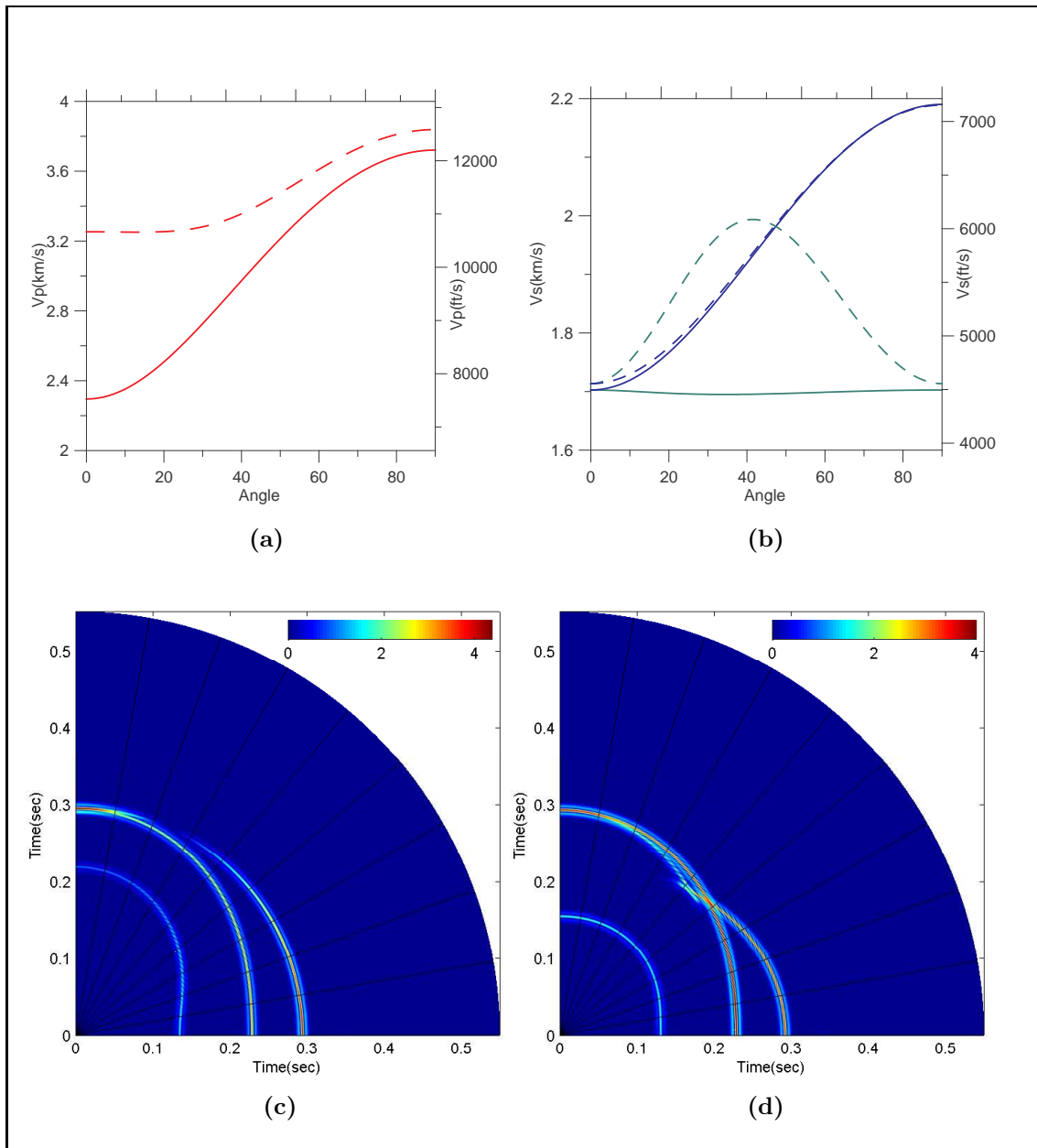
Figure 9.3: Effects of fluid types. (a) and (b) show P- and S-wave velocity behavior, respectively, for gas filled (solid line) and water filled (dashed line) cracks. Synthetic seismograms in a vertical plane corresponding to gas-filled and water-filled cracks are shown in (c) and (d), respectively. The model parameters are given in Table 9.1-Model#3.
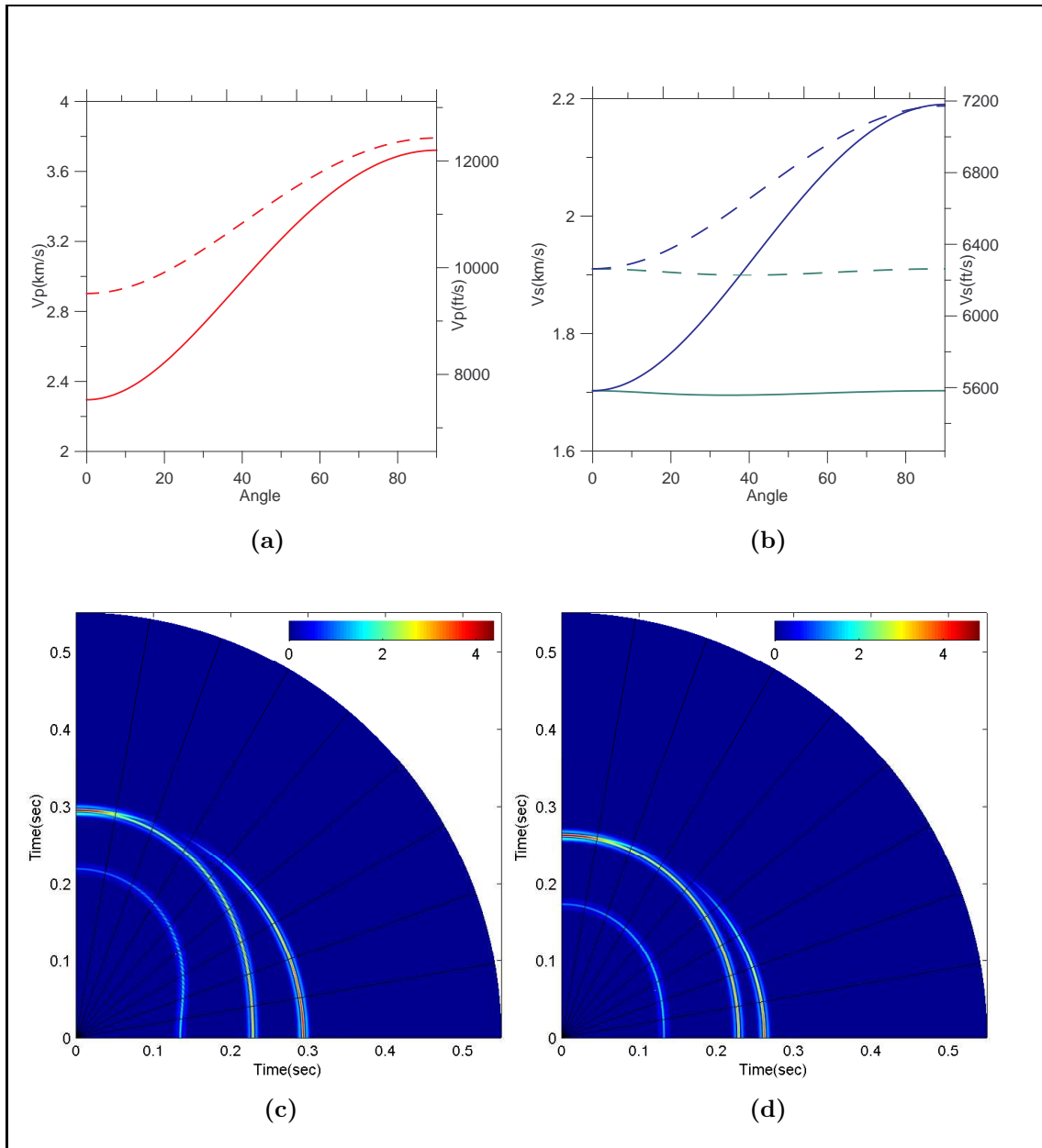
135

Figure 9.4: Gas filled cracks. Porosity 0.5%, Solid and dashed lines in (a) and (b) correspond to the aspect ratio of 0.03 and 0.1, respectively. Synthetic seismograms in a vertical plane: (c) for Ar=0.03; and, (d) for Ar=0.1
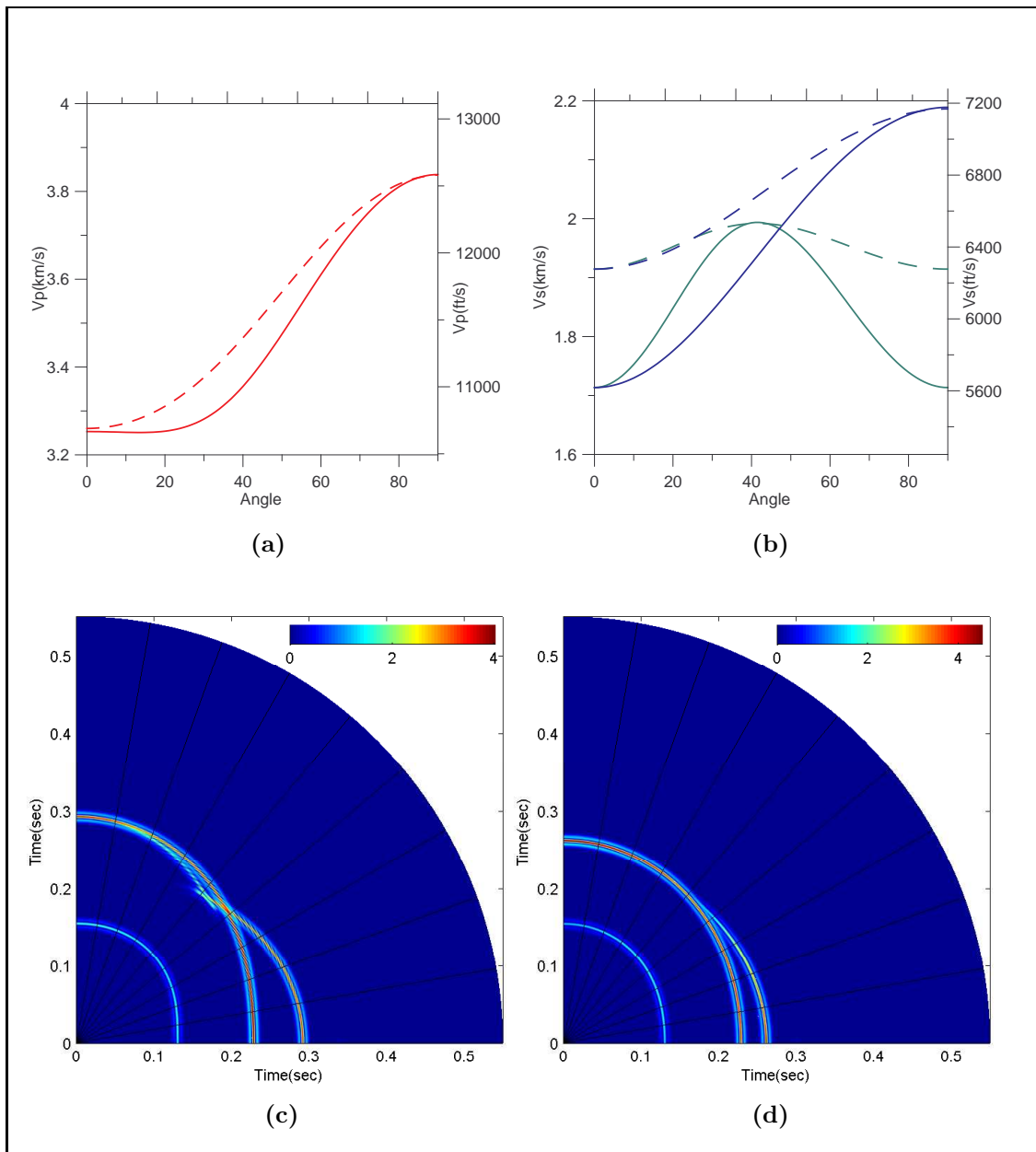
Figure 9.5: Water-filled cracks. Porosity 0.5%, Solid and dashed lines in (a) and (b) correspond to the aspect ratio of 0.03 and 0.1, respectively. Synthetic seismograms in a vertical plane: (c) for Ar=0.03; and, (d) for Ar=0.1

Figure 9.6: Vp and Vs behavior with changing porosity 0.5% (solid line), 1.0%(dashed line), 2.0%(dashed dot), 4.0%(dashed dot dot). Its phase velocity characteristics for P -wave are shown in (a) and for S-waves are shown in (b) (SH – Blue colored, SV – Green colored).

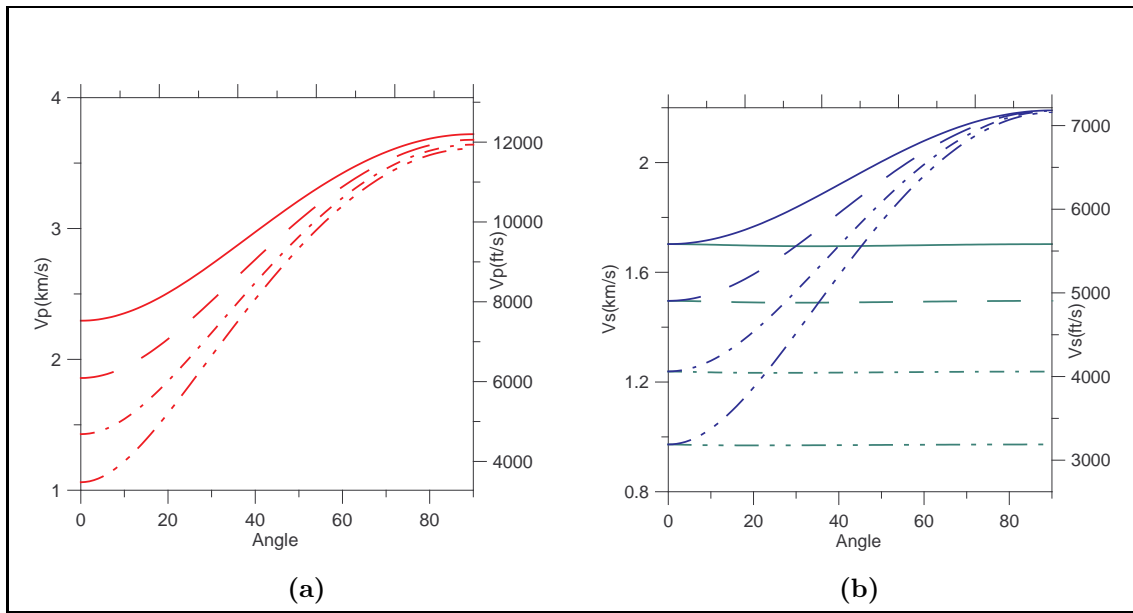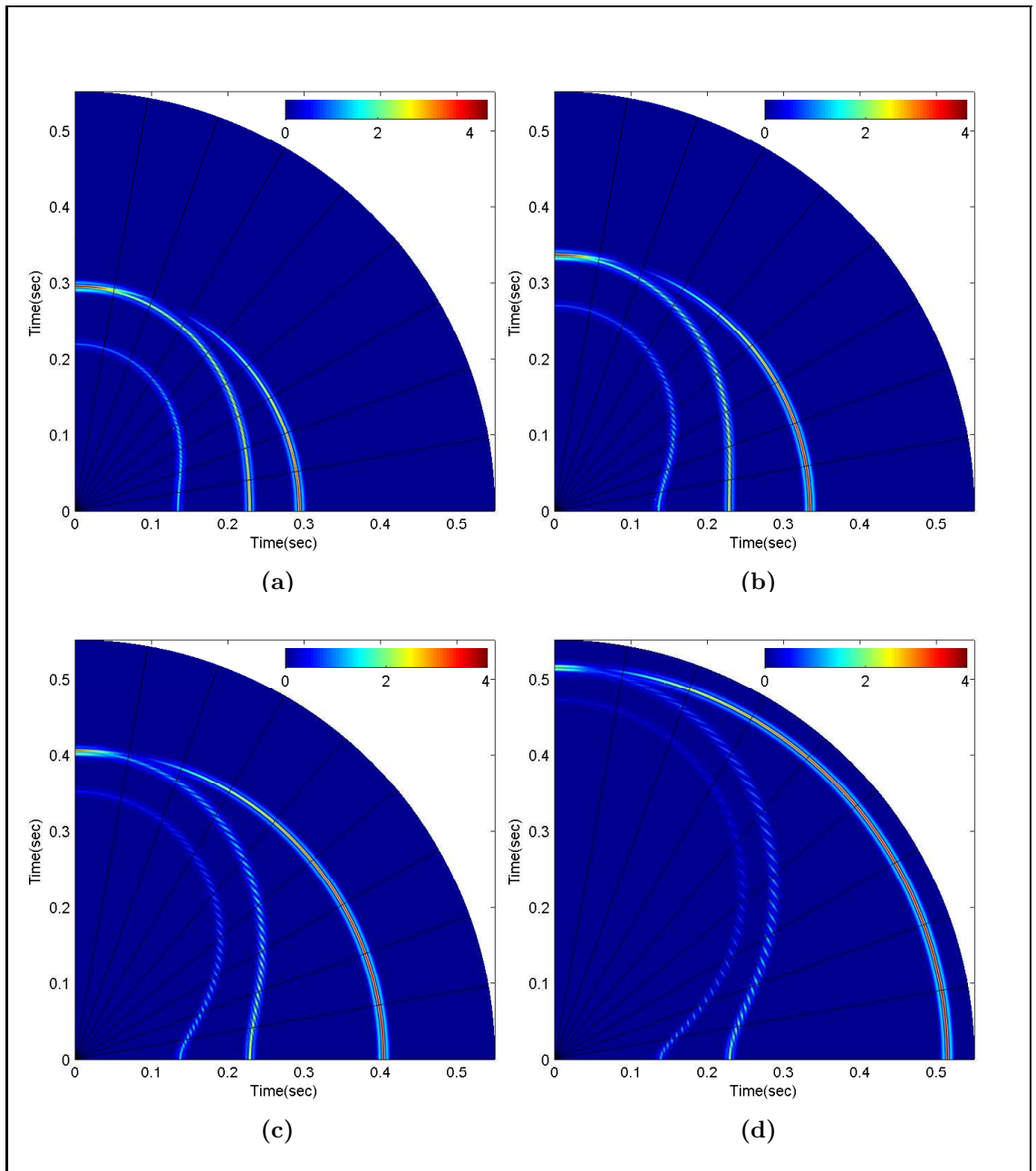Figure 9.7: Synthetic seismograms in a vertical plane for the model:(a)0.5% (b) 1.0% (c) 2.0% (d) 4.0%
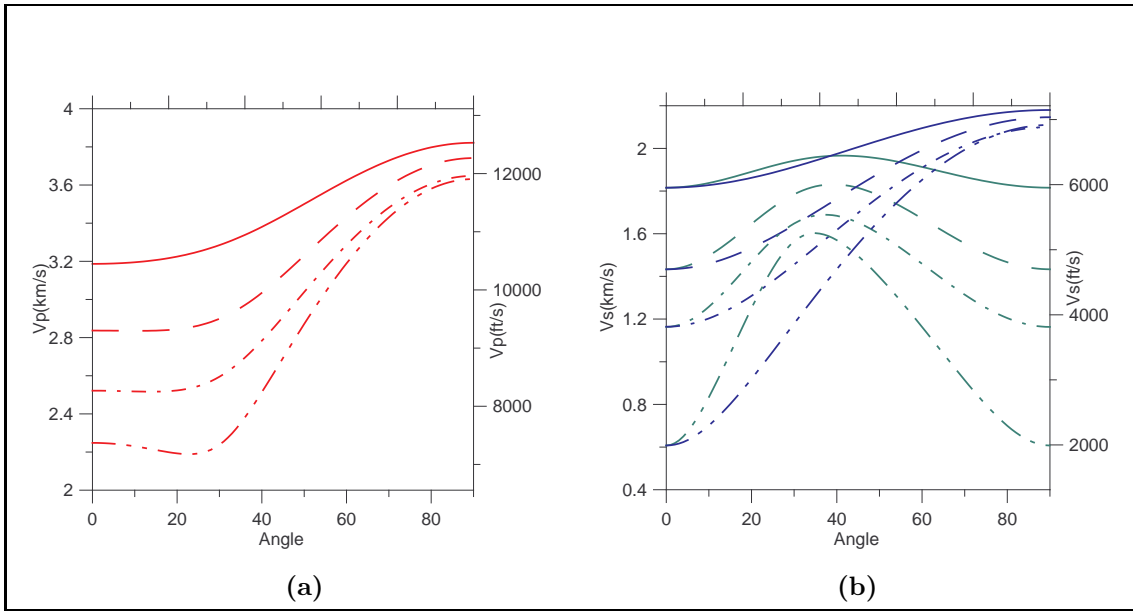
Figure 9.8: Vp and Vs behavior with changing porosity 1.0% (solid line), 4.0%(dashed line), 8.0%(dashed dot), 12.0%(dashed dot dot). Its phase velocity characteristics for P -wave are shown in (a) and for S-waves are shown (b) (SH – Blue colored, SV – Green colored).
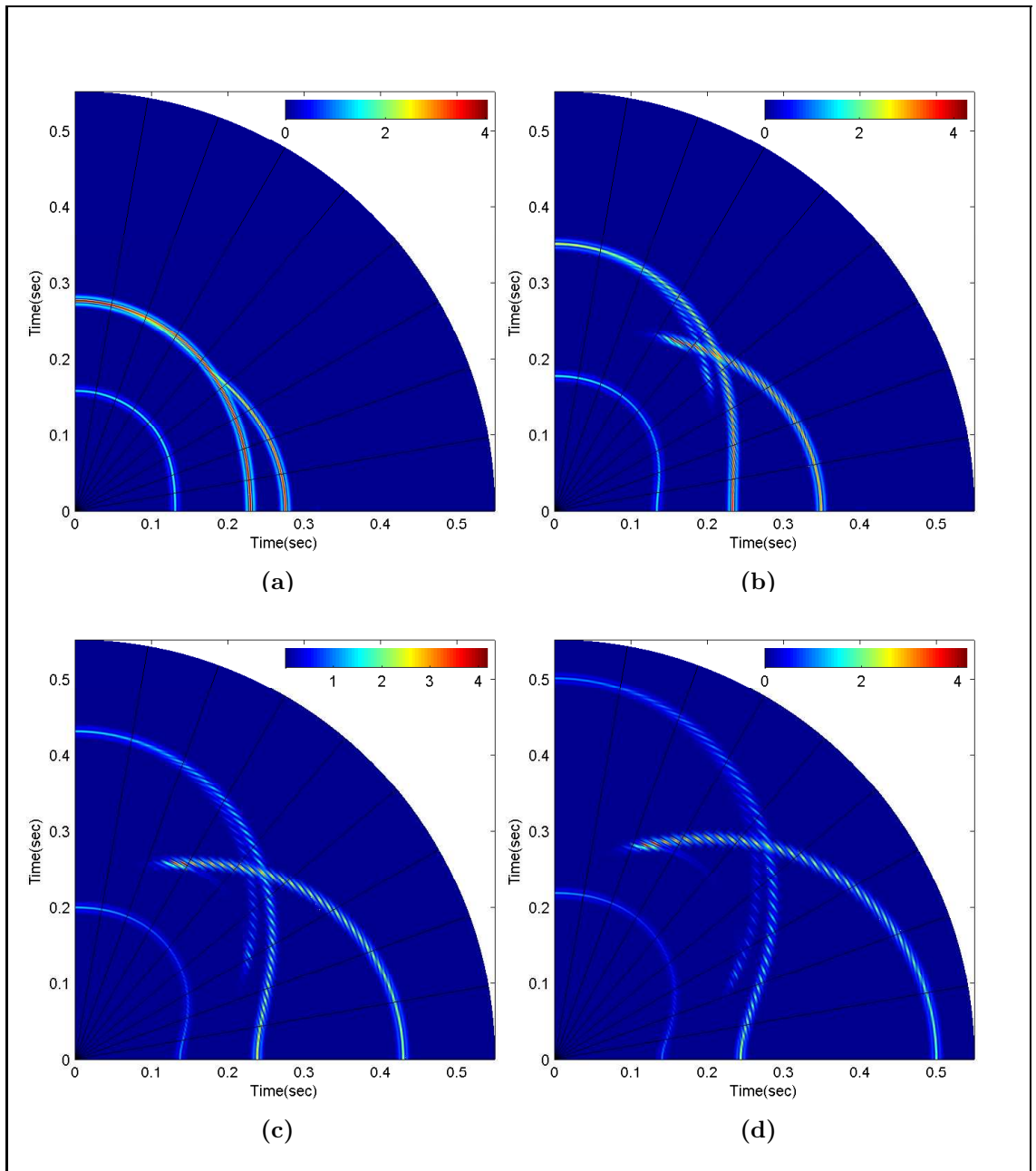
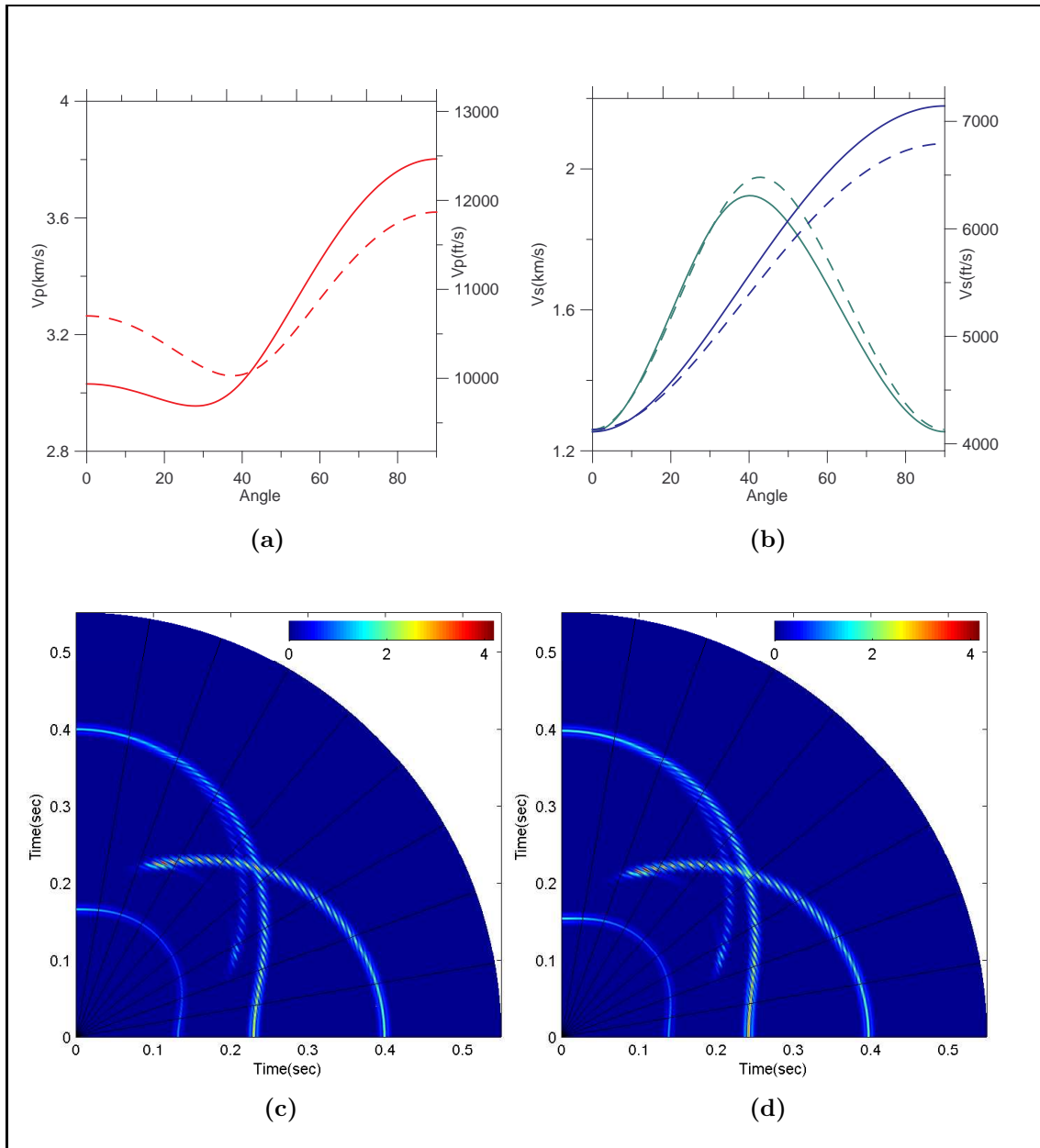Figure 9.9: Synthetic seismograms in a vertical plane for the model:(a)1.0% (b) 4.0% (c) 8.0% (d) 12.0%

Figure 9.10: Effects of clay orientation. The models have oriented cracks of aspect ratio 0.03. Solid and dashed lines in (a) and (b) represent oriented clay and random clay, respectively. Synthetic seismograms in a vertical plane (c) orientated clay and (d) random clay orientation

Chapter 10

Conclusions

The results of this dissertation contribute to the fundamental understanding of wave propagation in viscoelastic anisotropic media. A numerical technique for computing synthetic seismograms has been developed in the framework of the full waveform theory. Although full waveform synthetic is a time-consuming procedure compared to the ray synthetic, it offers the advantage of accurate computation of the wavefield of interest, including head waves. Moreover, it is not scuh an expensive method considering our present day computational power.

Although numerical implementation of an elastic wave equation in the form of the Green-Christoffel equation looks simple, a problem arises when shear wave slowness surfaces meet at acoustic axes, where the two shear waves can exchange polarizations. In this dissertation a novel method is developed to trace continuity in the polarizations.

Wave propagation in multilayered media requires that displacement and stress vectors be continuous everywhere, including the interfaces. A concise form of the

reflectivity method, which is unconditionally stable and easy to implement, is developed. The reflectivity method not only gives the full wavefield solution at any point in the multilayered media, but also yields frequency dependent reflection coefficients. Modeling of multilayered media suggests that the AVO behavior can be misunderstood if proper consideration of sounding frequency of investigation and layer thickness is not given. Reflection coefficient modeling of fractured media suggest that AVOAz can be potentially utilized in fracture characterization.

In another new development, radiation patterns of P- and S-waves are investigated in an unbounded homogeneous viscoelastic medium. It is observed that, as the quality factor Q decreases, S-wave radiation pattern shrinks faster than the P-wave radiation pattern does, and after a critical point on attenuation, the P-wave radiation pattern becomes larger than the S-wave radiation pattern. Not only are P and S waves amplitude characteristics modified in attenuating media, but their frequency characteristics are also altered. For this purpose spectral decomposition is used. Time-frequency spectrum of synthetic seismogram reveals that reference frequencies of the signal decrease with the decrease of Q values. This method has potential application in hydraulic fracturing of shales. Time dependent rock properties in a fractured reservoir can be estimated. With proper acquisition layout of micro-seismic measurements, the extent of fractured reservoir can be calculated.

Investigation of shale anisotropy from the standpoint of synthetic seismograms gives us the opportunity to understand seismic characteristics of shales. From theoretical shale models and their synthetic seismograms, it appears that investigation of the development of cusps on shear wave surfaces and their size could be another possible line of research. Note that the key parameters of the seismic anisotropy

144

models are: preferred orientation of clay particles, aspect ratio of cracks, porosity, and fluid type.

Bibliography

Aki, K., and Richards, P. G., 2002, Quantitative seismology: Univ. Sci. Books.

Bayuk, I. O., and Chesnokov, E. M., 2000, Modeling the physical properties of porous cracked anisotropic media: GeoCanada 2000 - The millenium Geoscience Summit.

Booth, D. C., and Crampin, S., 1983, The anisotropic reflectivity technique: Theory: Geophys. J. R. astr. Soc., **72**, 755–766.

Browning, D. B., 2006, Invesitgating well production in the barnett shale using curvature, anisotropy and microseismic events: Master's thesis, Univ. of Oklahoma.

Budreck, D. E., 1993, An eigenfunction expansions of the elastic wave Greens' fucntion for anisotropic media: Q. J. Mech. Appl. Math., **46**, 1–26.

Burrdige, R., 1967, The singularity on the plane lids of the wave surface of elastic media with cubic symmetry: Q. J. Mech. Appl. Math., **20**, 41–56.

Castaings, M., and Hosten, B., 1994, Delta operator technique to improve thomsonhaskell method stability for propagation in multilayered anisotropic absorbing plates: J. Acoust. Soc. Am., **95**, 1931–1941.

146

Cerveny, V., and Psencik, I., 2005, Plane waves in viscoelastic anisotropic media - I. Theory: Geophys. J. Int., **161**, 197–212.

Cerveny, V., and Ravindra, R., 1971, Theory of seismic head waves: Univ. Tor. Press.

Cerveny, V., 1972, Seismic rays and ray intensities in inhomogeneous anisotropic media: Geophys. J. R. astr. Res., **29**, 1–13.

Chadwick, P., and Smith, G. D., 1977, Foundations of the theory of surface waves in anisotropic elastic materials: Adv. Appl. Mech., **17**, 303–376.

Chen, H., 2000, Anisotropic effects upon amplitude-vs-offset response in realistic earth models: Ph.D. thesis, University of Oklahoma.

Chesnokov, E. M., and Abaseev, S. S., 1986, Theoretical seismograms of seismic surface waves in anisotropic media: Dokl. Acad. Sci. USSR, **286**, 592–597.

Chesnokov, E. M., Kukharenko, Y. A., and Kukharenko, P. Y., 1995, Method of diagram technique for calculation of effective physical parameters of microinhomogeneous media: SPIE, **2571**, 2–12.

Chung, M. Y., and Ting, T. C. T., 1995a, Line force, charge, and dislocation in angularly inhomogeneous anisotropic piezoelectric wedges and spaces: Phil. Mag. A, **71**, 1335–1343.

—— 1995b, Line force, charge, and dislocation in anisotropic piezoelectric composite wedges and spaces: J. Appl. Mech., **62**, 423–428.

Cormier, V. F., and Richards, P. G., 1977, Full wave theory applied to a discontinuous velocity increase: the inner core boundary: J. Geophys., **43**, 3–31.

Crampin, S., Chesnokov, E. M., and Hipkin, R. G., 1984, Seismic anisotropy - the state of the art: II: Geophys. J. R. astr. Soc., **76**, 1–16.

Crampin, S., 1981, A review of wave motion in anisotropic and cracked elastic media: Wave Motion, 343–391.

Duff, G. F. D., 1960, The cauchy problem of elastic waves in an anisotropic medium: Phil. Trans. R. Soc. Lond., **A252**, 249–273.

Dunkin, J. W., 1965, Computation of modal solutions in layered, elastic media at high frequencies: Bull. Seismol. Soc. Am., **55**, 335–358.

Eshelby, J. D., Read, W. T., and Shockley, W., 1953, Anisotropic elasticity with applications to dislocation theory: Acta Metall., **1**, 251–259.

Fedorov, F. I., 1968, Theory of elastic waves in crystals: Plenum Press, New York.

Fehler, M., Jupe, A., and Asanuma, H., 2001, More than cloud: New techniques for characterizing reservoir structure using induced seismicity: The Leading Edge, **20**.

Fryer, G. J., and Frazer, L. N., 1984, Seismic waves in stratified anisotropic media: Geophys. J. R. astr. Soc., **78**, 691–710.

Fryer, G. J., and Frazer, L. N., 1987, Seismic waves in stratified anisotropic media - II. Elastodynamic eigensolutions for some anisotropic systems: Geophys. J. R. astr. Soc., **91**, 73–101.

Fuchs, K., and Muller, G., 1971, Computation of synthetic seismograms with the reflectivity method and comparison with observations: Geophys. J. R. astr. Soc., **23**, 417–433.

Gajewski, D., and Psencik, I., 1987, Computation of high frequency seismic wavefields in 3-d laterally inhomogeneous anisotropic media: Geophys. J. R. astr. Soc., **91**, 383–412.

Gajewski, D., 1993, Radiation from point sources in general anisotropic media: Geophys. J. Int., **113**, 299–317.

Haskell, N. A., 1953, The dispersion of surface waves on multilayered media: Bull. Seism. Soc. Am., **43**, 17–34.

Head, A. K., 1953, Interaction of dislocations and boundaries: Phil. Mag., **44**, 92–94.

Helmberger, D. V., and Harkrider, D. G., 1978, Modeling earthquakes with generalized ray theory *in* J., M., and Achenbach, J., Eds., Modern Problems in Elastic Wave Propagation:: John Wiley and Sons, 499–518.

Hornby, B. E., Schwartz, L. M., and Hudson, J. A., 1994, Anisotropic effective-medium modeling of the elastic properties of shales: Geophysics, **59**, 1570–1583.

Ivanenko, D. D., and Sokolov, A. A., 1951, Classical theory of field: GITTL, Moscow.

Johnston, D. H., and Toksoz, M. N., 1981, Definitions and terminology: Seismic Wave Attenuation, 1–5.

Kachanov, M., 1992, Effective elastic properties of cracked solids: Critical review of some basic concepts: Appl. Mech. Rev., **45**, 304–335.

Kennett, B. L. N., and Kerry, N. J., 1979, Seismic waves in stratified half space: Geophys. J. R. astr. Soc., **57**, 557–583.

Kennett, B. L. N., 1974, Reflections, rays and reverbarations: Bull. Seismol. Soc. Am., **64**, 1685–1696.

Kennett, B. L. N., 1975, The effects of attenuation on seismograms: Bull. Seismol. Soc. Am., **65**, 1643–1651.

Knopoff, L., 1964, A matrix method for elastic wave porblems: Bull. Seismol. Soc. Am., **54**, 431–438.

Lifshitz, I. M., and Rozenzweig, L. N., 1947, On the construction of Green's tensor for the fundamental equation of the theory of elasticity of an anisotropic infinite medium: Zh. Eksp. Teor. Fiz.(in Russ.), **17**, 783–791.

Lowe, M. J. S., 1995, Matrix techniques for modeling ultrasonic waves in multilayered media: IEEE Trans. Ultrason. Ferroelectro. Freq. Contr., **42**, 525–542.

Lynn, H. B., 2004, The winds of change: Anistrophic rocks–their preferred direction of fluid flow and their associated seismic signatures, part 1: The Leading Edge, **23**, 1156–1162.

Mandal, B., and Toksoz, M. N., 1990, Computation of complete waveforms in general anisotropic media - results from an explosion source in an anisotropic medium: Geophys. J. Int., **103**, 33–45.

Martynov, V. N., and Mikhailenko, B. G., 1984, Numerical modeling of propagation of elastic waves in anisotropic inhomogeneous media for the half-space and the sphere: Geophys. J. R. astr. Soc., **76**, 53–63.

Morlet, J., Arens, G., Fourgeau, E., and Giard, D., 1982, Wave propagation and sampling theory: Geophysics, **47**, no. 2, 203–206.

Nayfeh, A. H., 1991, The general problem of elastic wave propagation in multilayered anisotropic media: J. Acoust. Soc. Am., **89**, 1521–1531.

Norris, A. N., 1994, Dynamic Green's functions in anisotropic piezoelectirc, thermoelastic and poroelastic solids: Proc. R. Soc. Lond. A, 175–188.

Oda, M., Suzuki, K., and Maeshibu, T., 1984, Elastic compliance for rock-like materials with random cracks: Soils and Foundations, **24**, 27–40.

Pan, E., 2003, Three-dimensional green's functions in an anisotropic half-space with general boundary conditions: J. Appl. Mech., **70**, 101–110.

Petrashen, G. I., and Kashtan, B. M., 1984, Theory of body-wave propagation in inhomogeneous anisotropic media: Geophys. J. R. astr. Soc., **76**, 29–39.

Rokhlin, S. I., and Wang, L., 2002, Stable recursive algorithm for elastic wave propagation in layered anisotropic media: Stiffness matrix method: J. Acoust. Soc. Am., **112**, 822–834.

Rokhlin, S. I., Bolland, T. K., and Laszlo, A., 1986, Reflection and refraction of elastic waves on a plane interface between two generally anisotropic media: J. Acout. Soc. Am., **79**.

Schoenberg, M., and Sayers, C. M., 1995, Seismic anisotropy of fractured rock: Geophysics, **60**, 204–211.

Searcy, T. Y., Abaseyev, S., Chesnokov, E. M., and Ammerman, M., 2005, Microearthquake investigations in the barnett shale, newark east field, wise county, texas:, *in* 75th Annual International Meeting Soc. of Expl. Geophys., 166–169.

Shermergor, T. D., 1977, Theory of elasticity of microinhomogeneous media: Nauka (in Russian).

Sinha, S., Routh, P. S., Anno, P. D., and Castagna, J. P., 2005, Spectral decomposition of seismic data with continuous-wavelet transform: Geophysics, **70**, no. 6, P19–P25.

Stroh, A. N., 1958, Dislocations and cracks in anisotropic elasticity: Phil. Mag., **3**, 625–646.

Stroh, A. N., 1962, Steady state problems in anisotropic elasticity: J. Math. Phys., **41**, 77–103.

Synge, J. L., 1957, Elastic waves in anisotropic media: J. Math. Phys., **35**, 323–334.

Taylor, D. B., 1987, Double contour integration for transmissions from point sources through anisotropic layers as used in rocpac software: Geophys. J. R. astr. Soc., **91**, 373–382.

Thomson, W. T., 1950, Transmission of elastic waves through a stratified media: J. Appl. Phys., **21**, 89–93.

Ting, T. C. T., and Lee, V.-G., 1997, The three-dimensional elastostatic Green's
function for general anisotropic linear elastic solids: Q. J. Mech. Appl. Math., **50**,
407–426.

Ting, T. C. T., 1996, Anisotropic elasticity: Theory and applications: Oxford Univ.
Press.

Tsvankin, I. D., and Chesnokov, E. M., 1990, Synthetic waveforms and polarizations
at the free surface of an anisotropic half-space: Geophys. J. Int., **101**, 497–505.

Vshivtsev, A. S., Tatarintsev, A. V., and Chesnokov, E. M., 1995, The Green func-
tion of wave equation in the presence of an anisotropic medium: Physics of the
Solid Earth, **30**, 822–829.

Wang, C. Y., and Achenbach, J. D., 1993, A new method to obtain 3-d Green's
functions for anisotropic solids: Wave Motion, **18**, 273–289.

White, J. E., 1965, Seismic waves: Radiation, transmission, and attenuation:
McGraw-Hill Book Co.,Inc., New York.

Willis, J. R., 1970, Stress field produced by dislocations in anisotropic media: Phil
Mag., **21**, 931–949.

Yilmaz, O., 2000, Seismic data analysis vol 1: Soc. Expl. Geophys.

Zhu, Y., and Tsvankin, I., 2006, Plane-wave propagation in attenuative transversely
isotropic media: Geophysics, **71**, T17–T30.

Appendix A

Dynamic Green Tensor in ω and k domain

$$(\delta_{im}\rho\partial_t^2 - \partial_j C_{ijmn}\partial_n)G_{ml}(t;\mathbf{r}) = \delta_{il}\delta(\mathbf{r})\delta(t)$$

or,
$$L_{im}(t;\mathbf{r})G_{ml}(t;\mathbf{r}) = \delta_{il}\delta(\mathbf{r})\delta(t) \qquad \text{(A.1)}$$

where $L_{im}(t;\mathbf{r}) = (\delta_{im}\rho\partial_t^2 - \partial_j C_{ijmn}\partial_n)$ is a partial differential operator.

Using the Fourier transformation, one can write:

$$G_{ml}(t;\mathbf{r}) = \int \frac{d\omega}{2\pi} \int \frac{d\mathbf{k}}{(2\pi)^3} G_{ml}(\omega;\mathbf{k})e^{i(\mathbf{kr}-\omega t)} \qquad \text{(A.2)}$$

$$\delta(t) = \int \frac{d\omega}{2\pi}e^{-i\omega t} \qquad \text{(A.3)}$$

$$\delta(\mathbf{r}) = \int \frac{d\mathbf{k}}{(2\pi)^3}e^{i\mathbf{kr}} \qquad \text{(A.4)}$$

Substituting equations A.2, A.3 and A.4 in equation A.1, one obtains:

$$(-\delta_{im}\rho\omega^2 + C_{ijmn}k_j k_n)G_{ml}(\omega;\mathbf{k}) = \delta_{il}$$

$$L_{im}(\omega;\mathbf{k})G_{ml}(\omega;\mathbf{k}) = \delta_{il} \qquad \text{(A.5)}$$

Appendix B

Propagation in Homogeneous Anisotropic

Medium
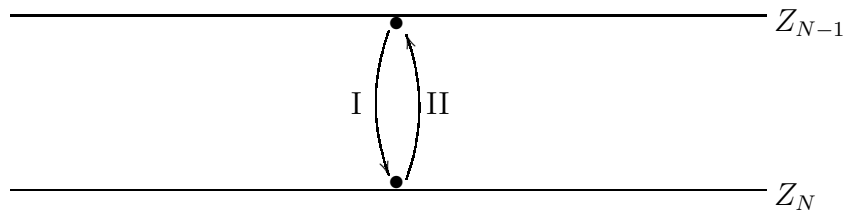
Figure B.1: This is a schematic diagram showing a layer and two points – one just below the upper boundary and another just above the lower boundary.

Let us say that the upgoing wavefields just below the upper boundary layer and just above the lower boundary layer are $f_{Z_{N-1}}^{\oplus}$ and $f_{Z_N}^{\oplus}$, respectively. When a source is below the layer, the R-T coefficients are computed by moving the wavefield from the upper half space or free surface to the source. Thus, within a homogeneous anisotropic layer, one can move wavefield from the $(N-1)^{th}$ layer to the Nth layer marked as **I** in the figure above. Similarly, when the source is above the layer, one

can move the wavefield from the Nth layer to $(N-1)^{th}$ layer marked as **II** in the above figure. One can write:

$$f_{Z_{N-1}}^{\oplus} = e^{-i\omega p_z^{\oplus} Z_{N-1}} \mathbb{U}$$

and, $\qquad f_{Z_N}^{\oplus} = e^{-i\omega p_z^{\oplus} Z_N} \mathbb{U}.$

$\therefore \qquad e^{i\omega p_z^{\oplus} Z_{N-1}} f_{Z_{N-1}}^{\oplus} = e^{i\omega p_z^{\oplus} Z_N} f_{Z_N}^{\oplus}$

or, $\qquad f_{Z_N}^{\oplus} = e^{i\omega p_z^{\oplus}(Z_{N-1}-Z_N)} f_{Z_{N-1}}^{\oplus}$

or, $\qquad f_{Z_N}^{\oplus} = (E^{\oplus})^{-1} f_{Z_{N-1}}^{\oplus}.$

Similarly, $\qquad f_{Z_N}^{\ominus} = (E^{\ominus})^{-1} f_{Z_{N-1}}^{\ominus}.$ $\hfill$ (B.1)

where $(E^{\oplus}) = e^{-i\omega p_z^{\oplus} \Delta Z}$, and $(E^{\ominus}) = e^{-i\omega p_z^{\ominus} \Delta Z}$; ΔZ being thickness of the layer and is a positive quantity. Similarly in the case **II**, one can write:

$$f_{Z_{N-1}}^{\oplus} = E^{\oplus} f_{Z_N}^{\oplus} \quad \text{and} \quad f_{Z_{N-1}}^{\ominus} = E^{\ominus} f_{Z_N}^{\ominus} \qquad \text{(B.2)}$$

Appendix C

Additional Figures for Reflection Coefficients
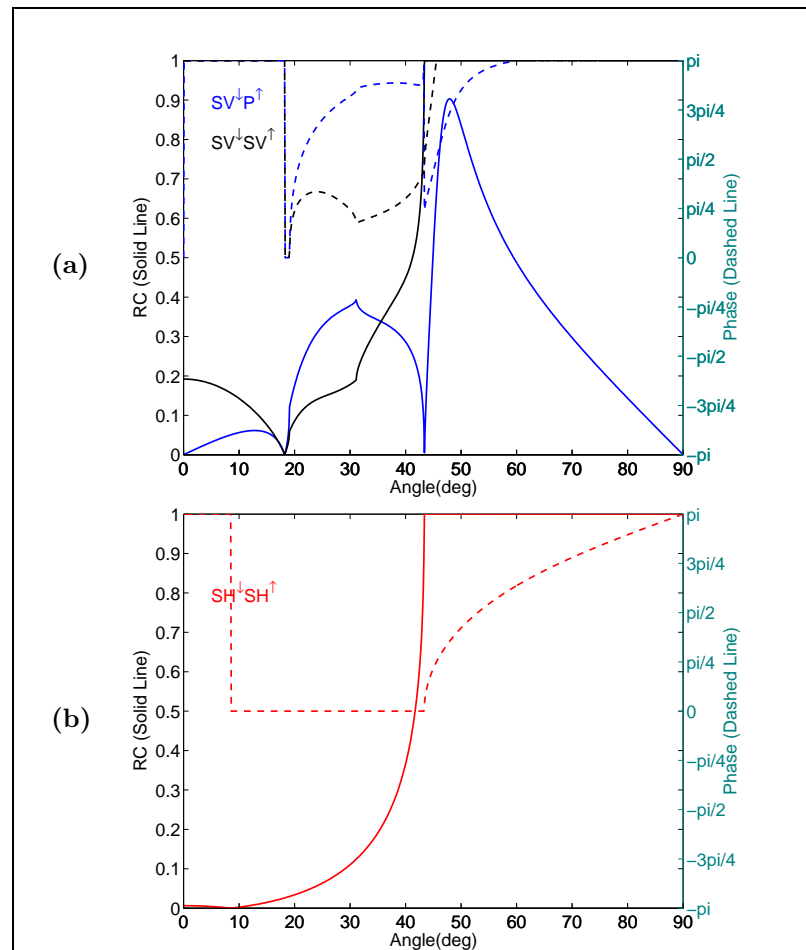
Figure C.1: Reflection coefficients (solid line) and phase change (dashed line) at the interface between two isotropic half spaces for the incident SV and SH waves are shown in (a) and (b), respectively. The elastic coefficients used for the computation are given in Table 5.1.
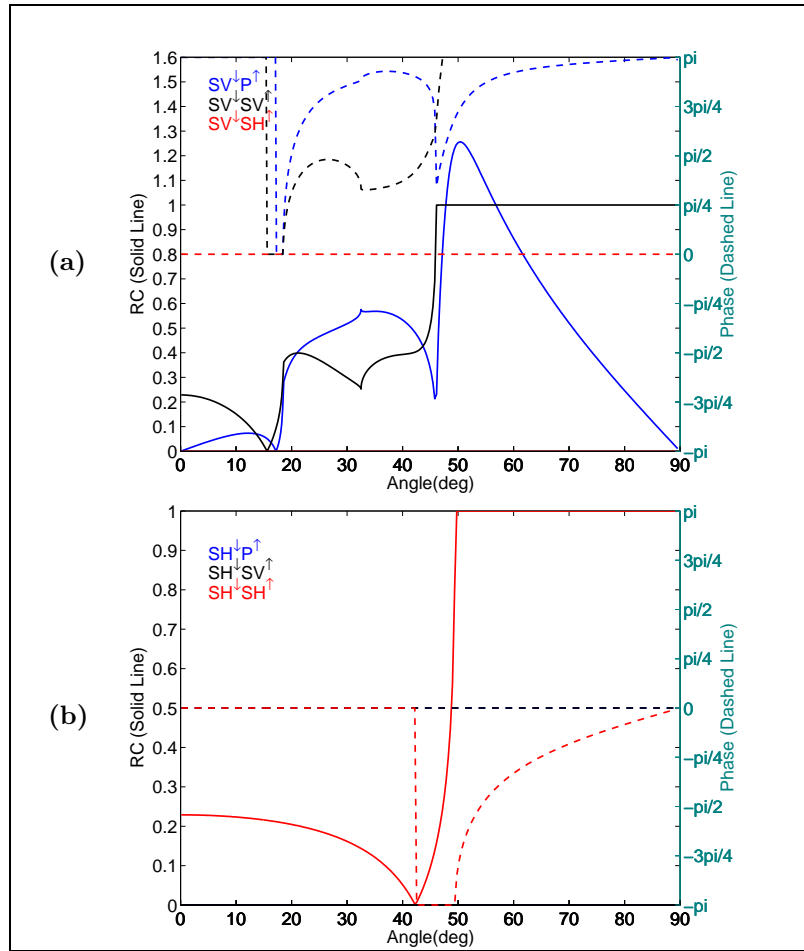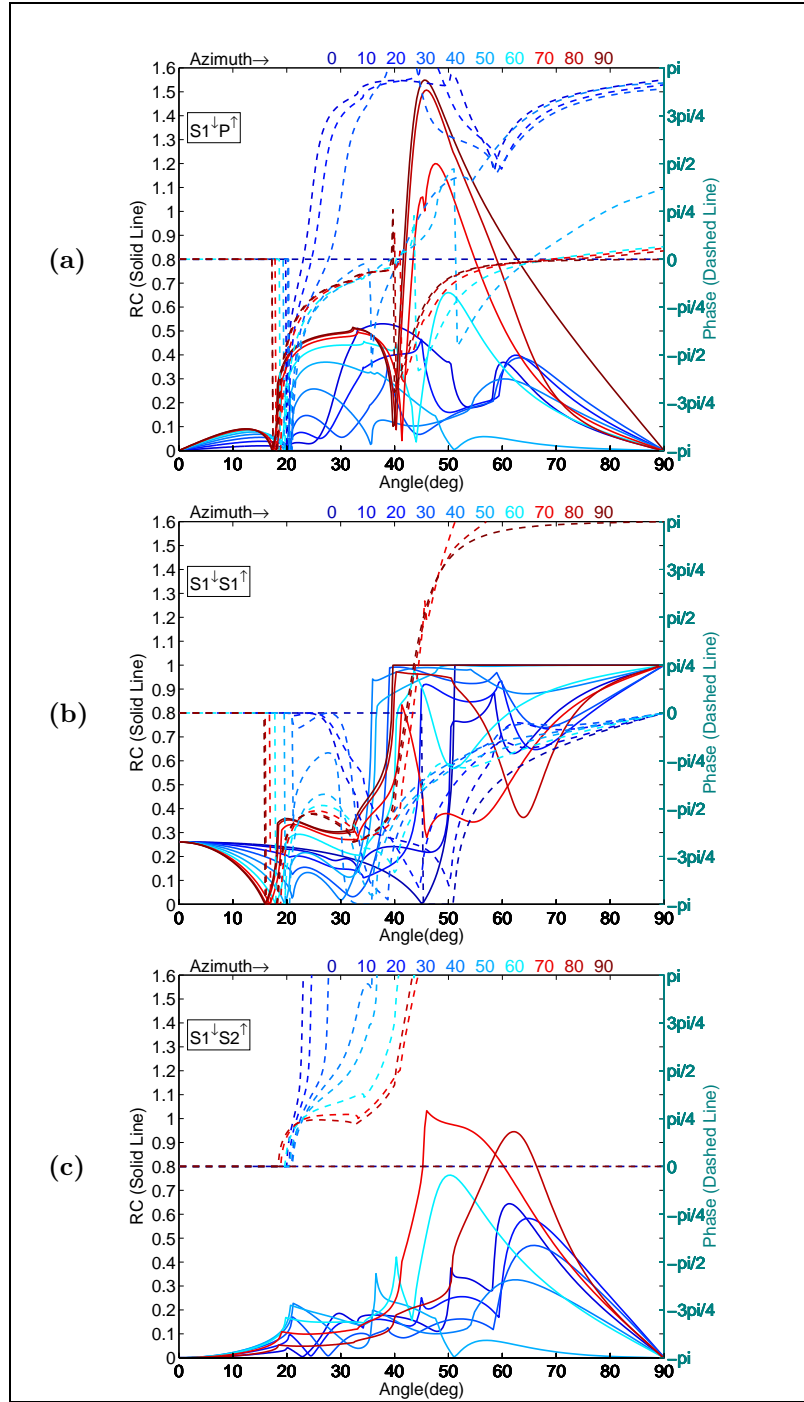
Figure C.2: Reflection coefficients and phase change at the interface between tow VTI half spaces for the incident SV and SH waves are shown in (a) and (b), respectively. The elastic coefficients used for the computation are given in Table 5.1.

Figure C.3: Reflection coefficients and phase change at the boundary between two orthorhombic half spaces. The elastic constants for the two half spaces are given in Table 5.1. The reflection coefficients are computed for an incident S1-wave and the reflected (a) P, (b) S1, and (c) S2 wave types. The curves are colored according to the azimuthal variation of the reflection coefficients.

159
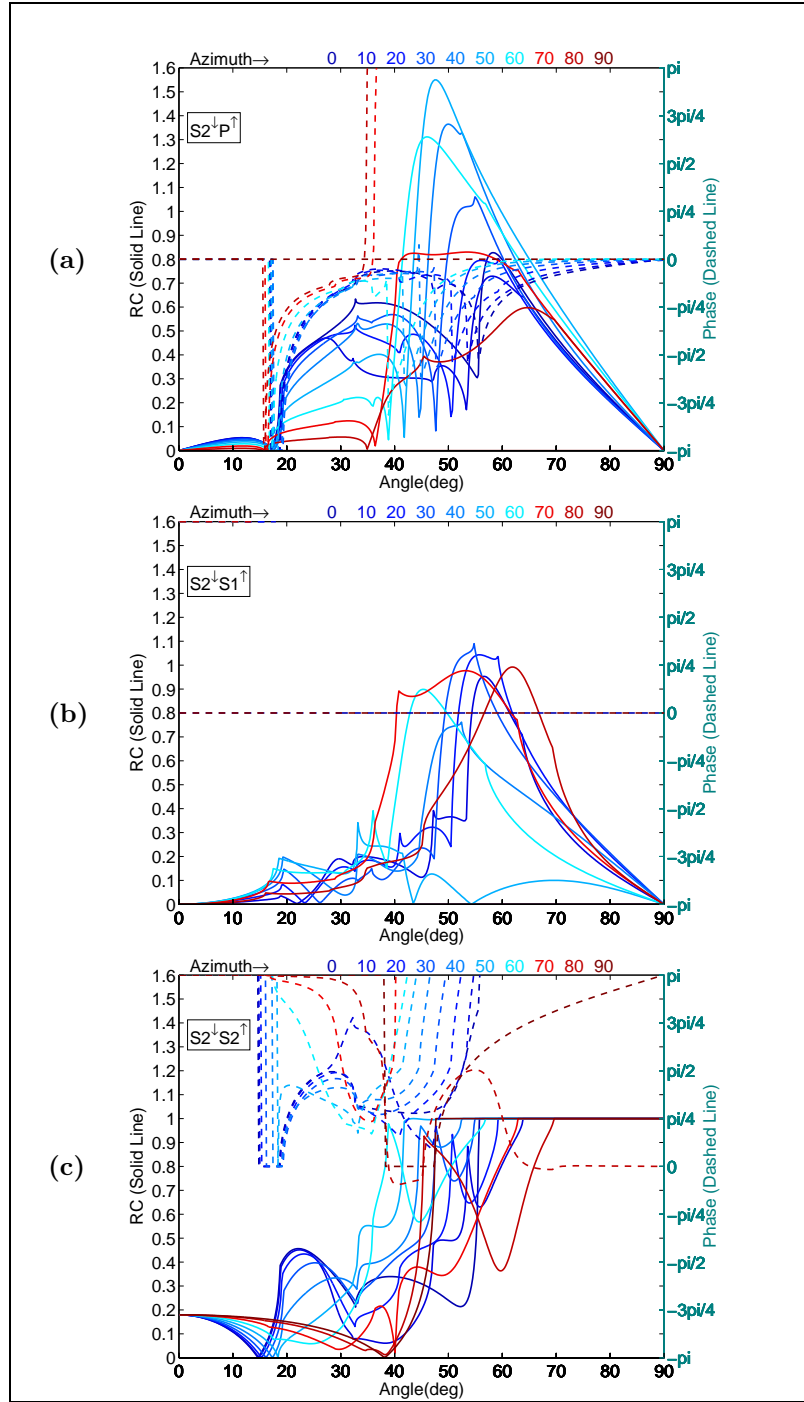
Figure C.4: Reflection coefficients and phase change at the boundary between two orthorhombic half spaces. The elastic constants for the two half spaces are given in Table 5.1. The reflection coefficients are computed for an incident S2-wave and the reflected (a) P, (b) S1, and (c) S2 wave types. The curves are colored according to the azimuthal variation of the reflection coefficients.
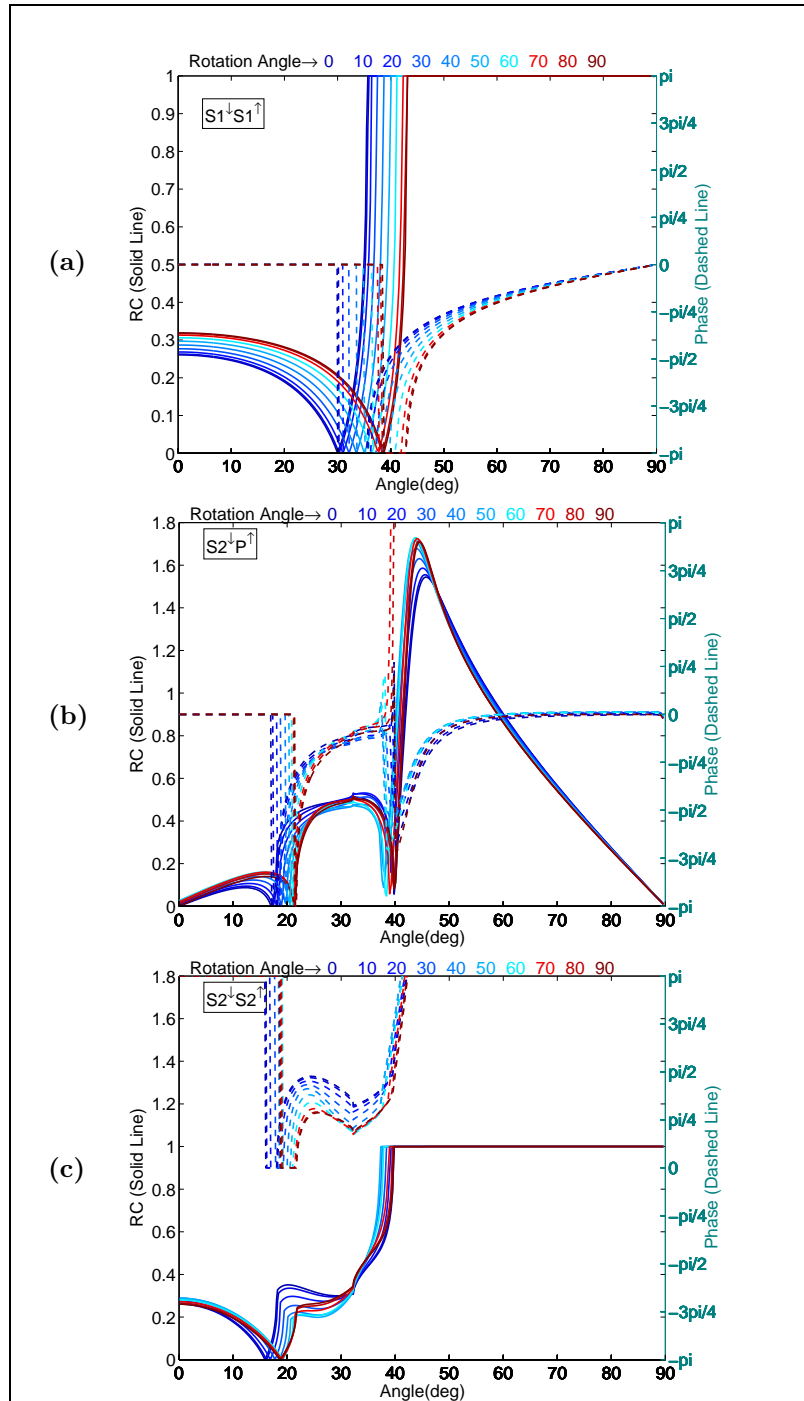
Figure C.5: Reflection coefficients are in the vertical plane containing the vertical symmetry axis of the upper half space and the tilted symmetry axis of the lower half space: (a) for incident S1 and reflected S1, (b) and (c) for incident S2 and reflected P and S2 waves, respectively. The curves are colored according to the rotation angle of symmetry axis from the vertical in the lower half space.

161
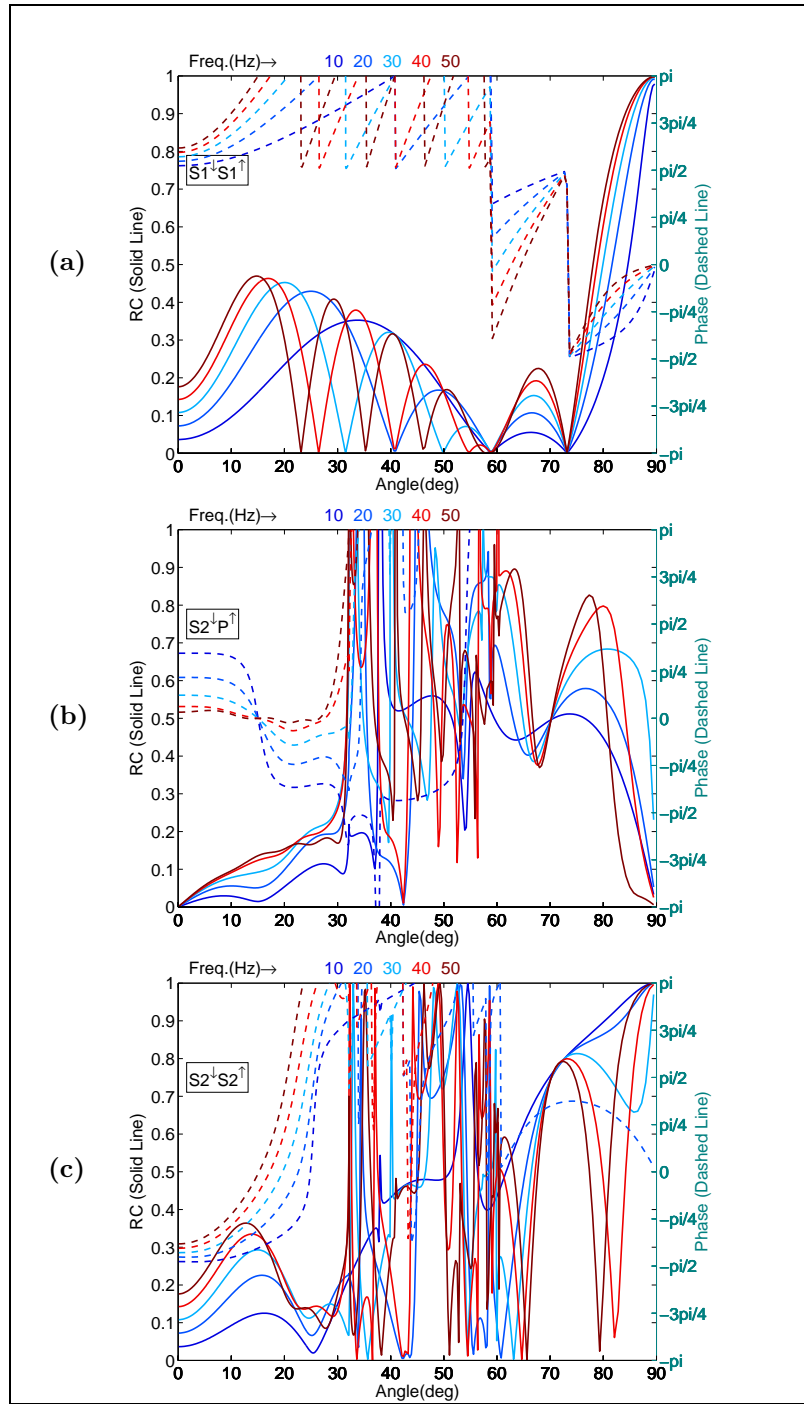
Figure C.6: Reflection coefficient and phase for the reflected (a) S1-wave from an incident S1-wave and for the reflected (b) P-wave and (c) S2-wave from an incident S2-wave in the frequency range of 10 to 50Hz. The elastic coefficients used for this calculation are given in Table 5.3.
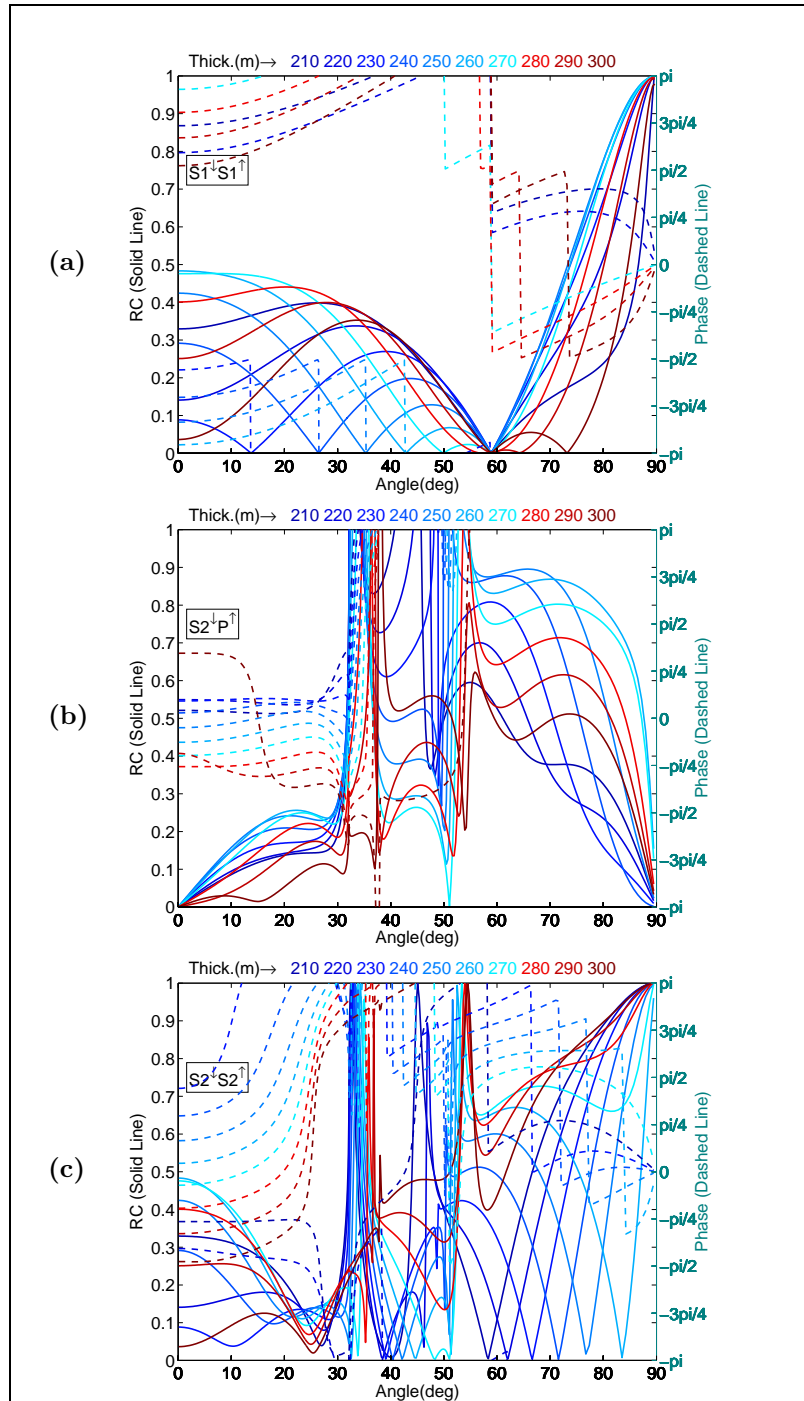
Figure C.7: Reflection coefficient and phase for the reflected (a)S1-wave from an incident S1-wave and for the reflected (b) P-wave and (c) S2-wave from an incident S2-wave. The curves are colored according the thickness variation (210-300m) of the sandwiched layer. The elastic coefficients used for this calculation are given in Table 5.3.

Appendix D

Additional Figures for Fractured Media

Additional figures are included here for the reflection coefficients of the five fracture models used in chapter 6. Figures D.1, D.2 and D.3 are plotted for the reflection coefficients of P, S1 and S2 waves, respectively, from an incident S1 wave and the corresponding reflection coefficients for an incident S2 waves are shown in Figures D.4 to D.6.
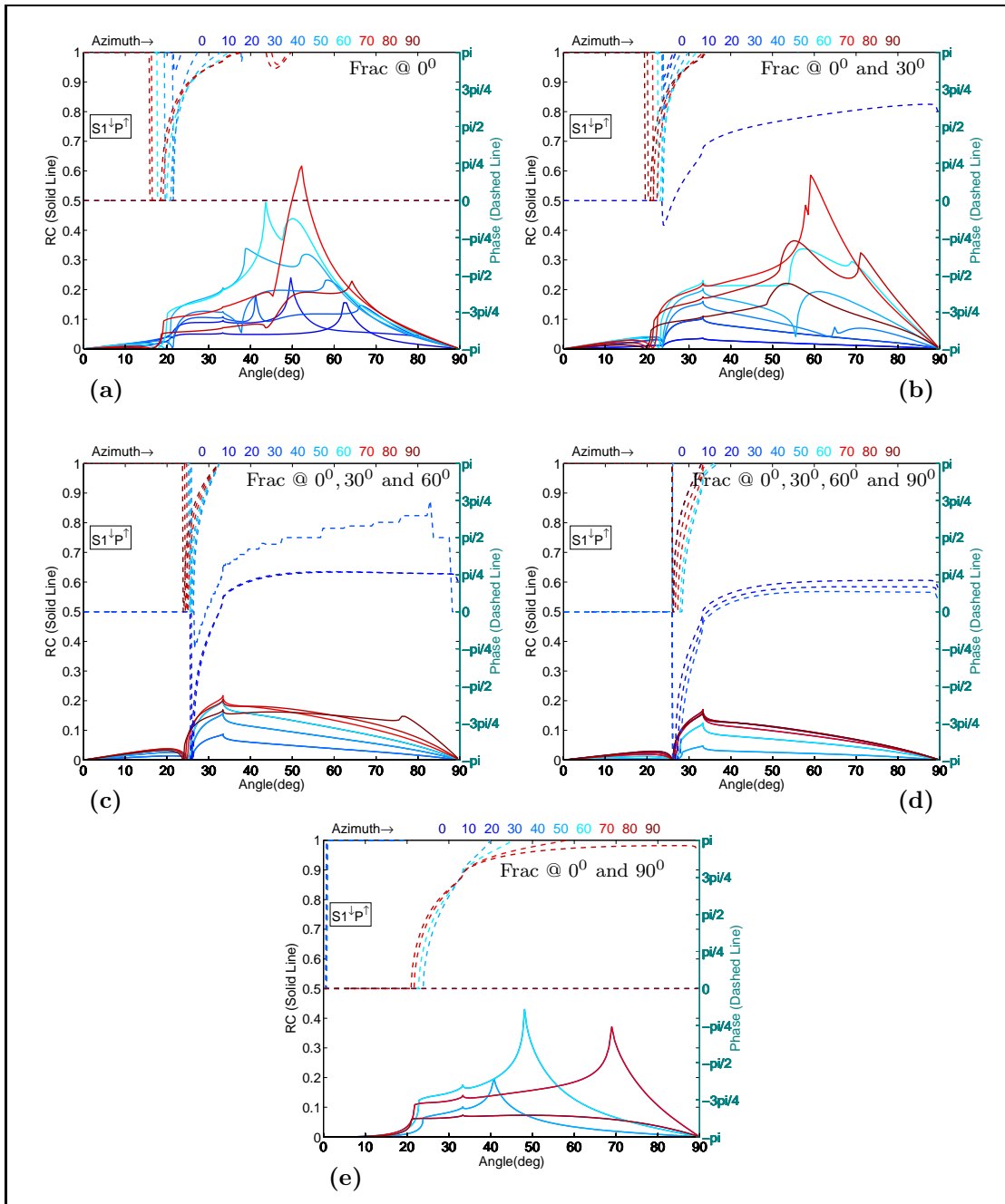
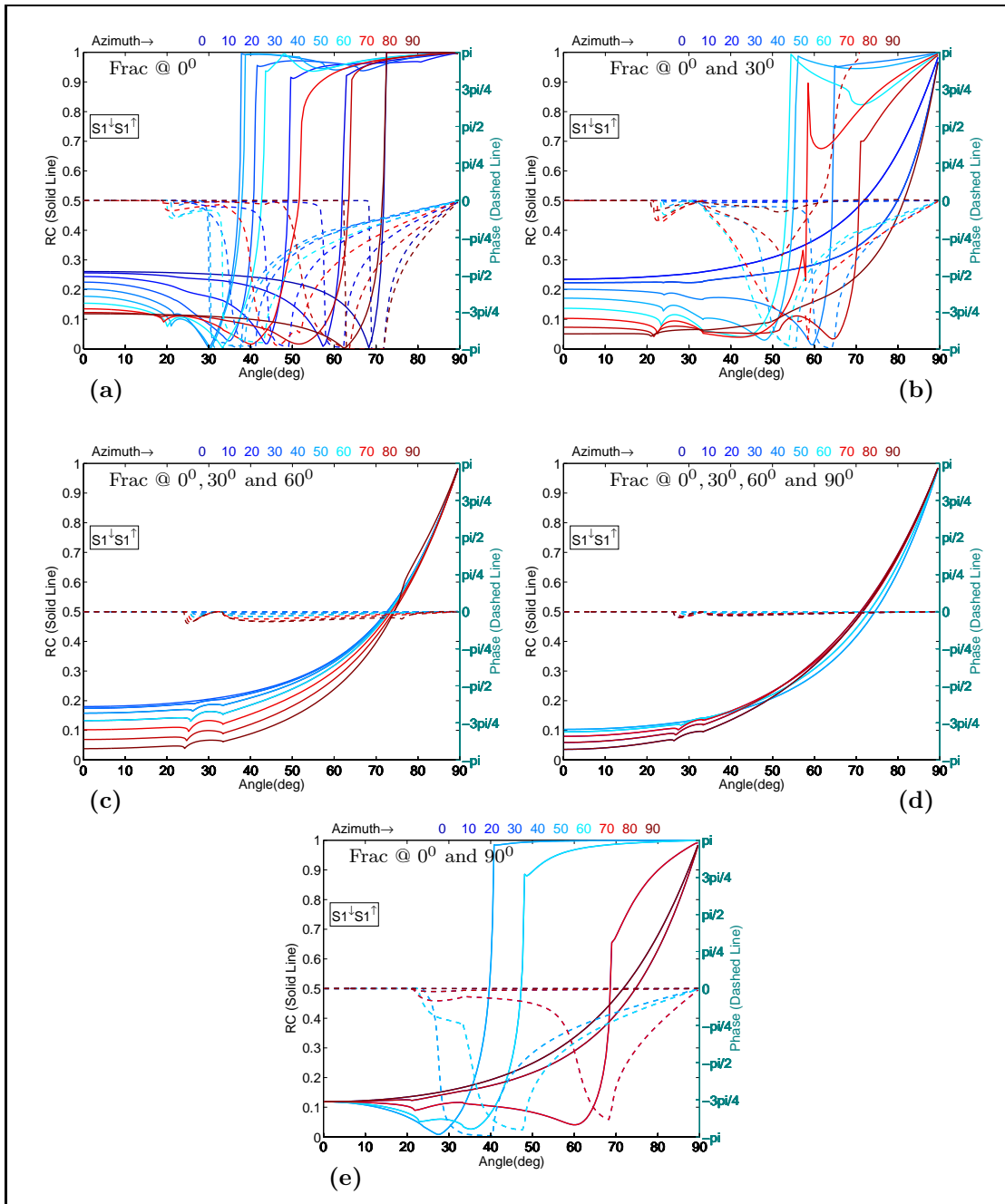Figure D.1: S1P reflection coefficients and phase variation with angle and azimuth.

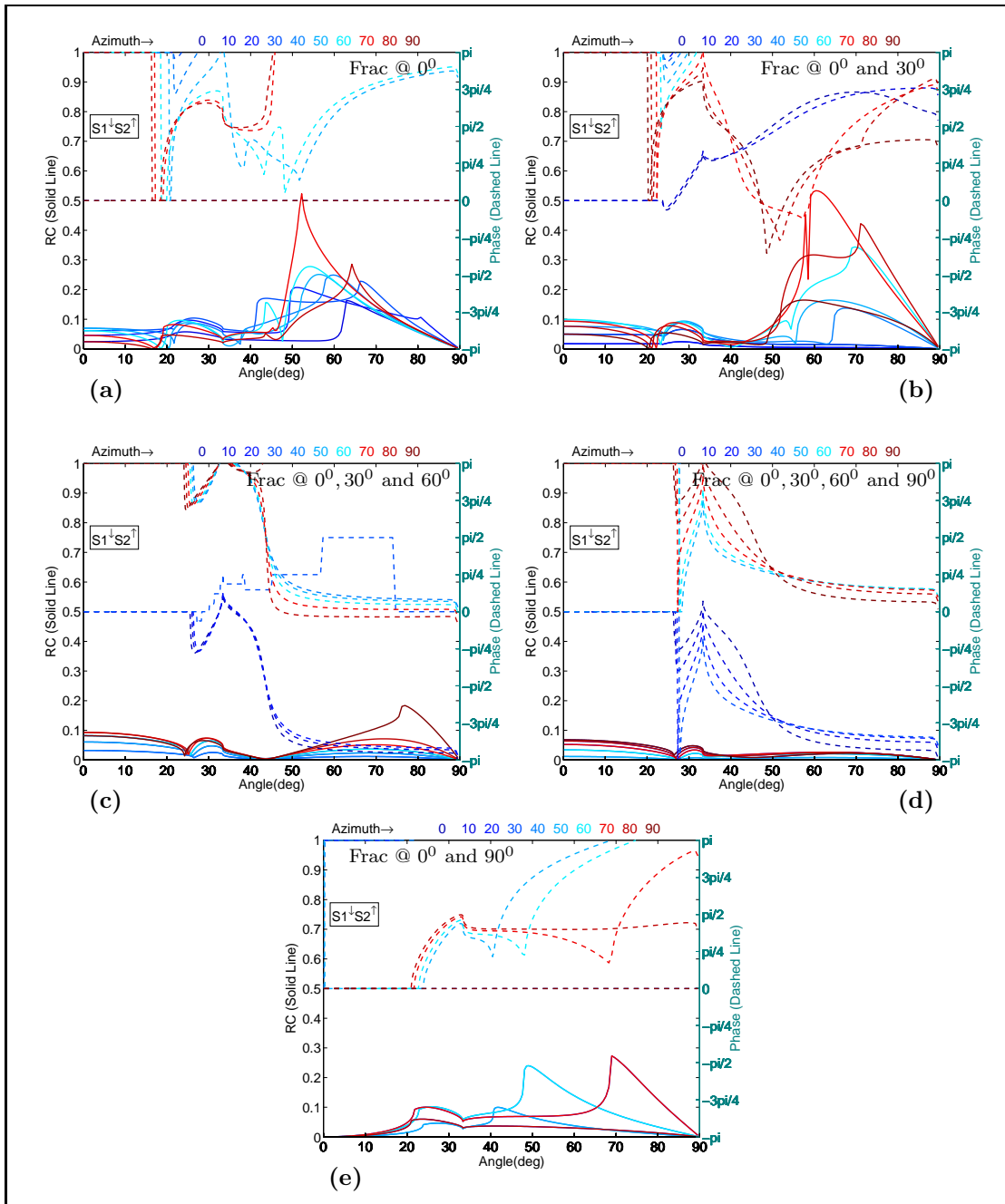Figure D.2: S1S1 reflection coefficients and phase variation with angle and azimuth.

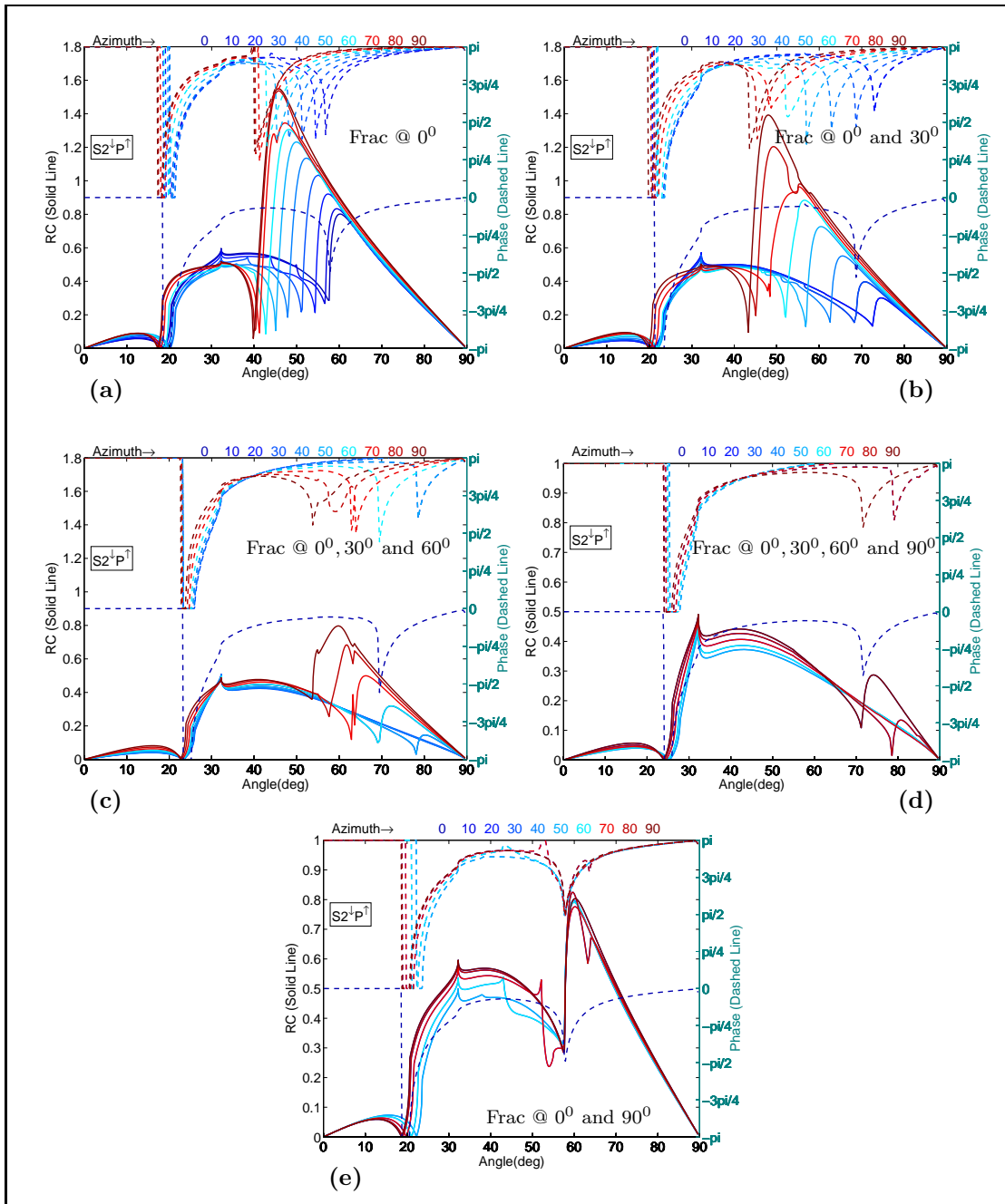Figure D.3: S1S2 reflection coefficients and phase variation with angle and azimuth.

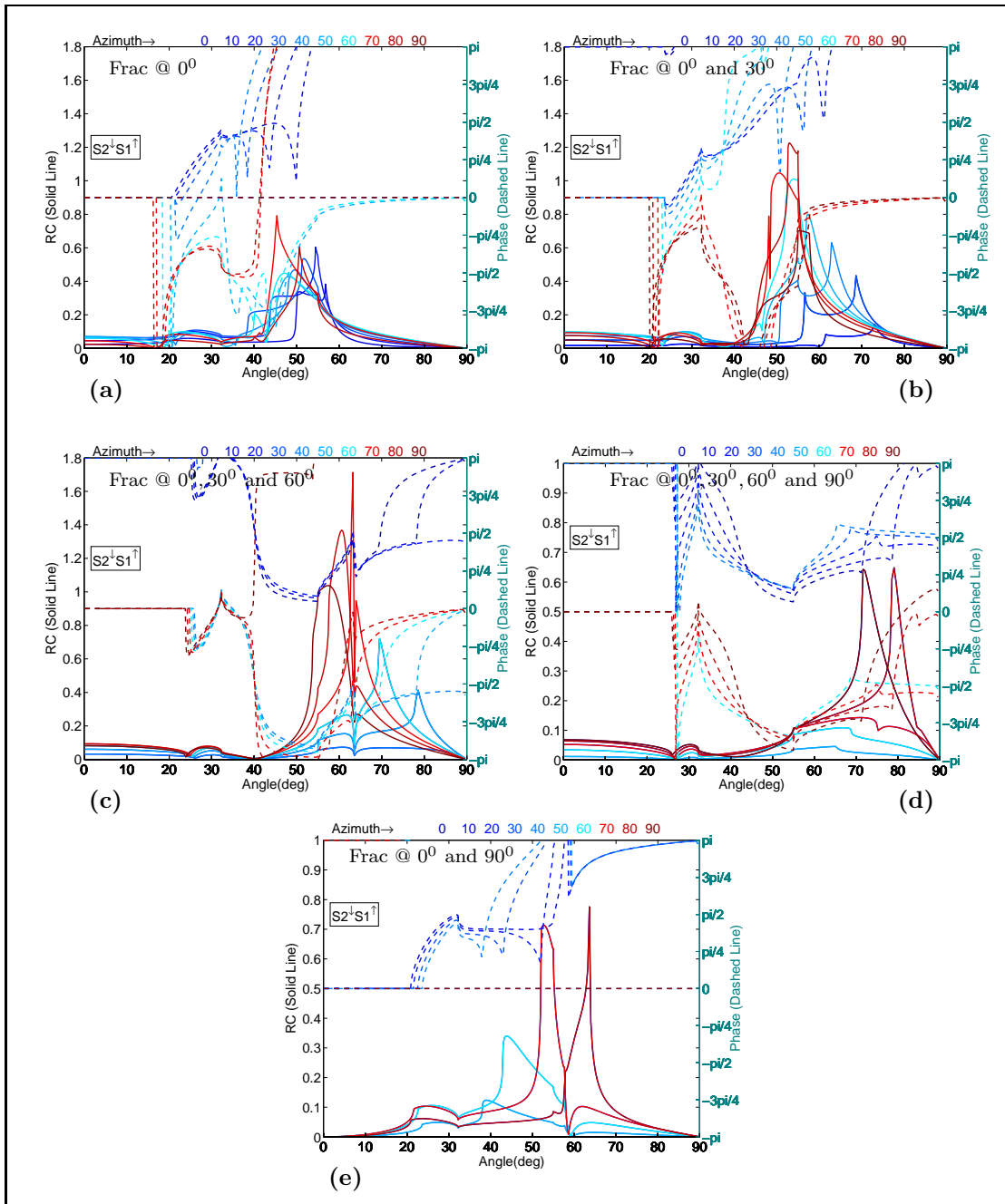Figure D.4: S2P reflection coefficients and phase variation with angle and azimuth.

Figure D.5: S2S1 reflection coefficients and phase variation with angle and azimuth.
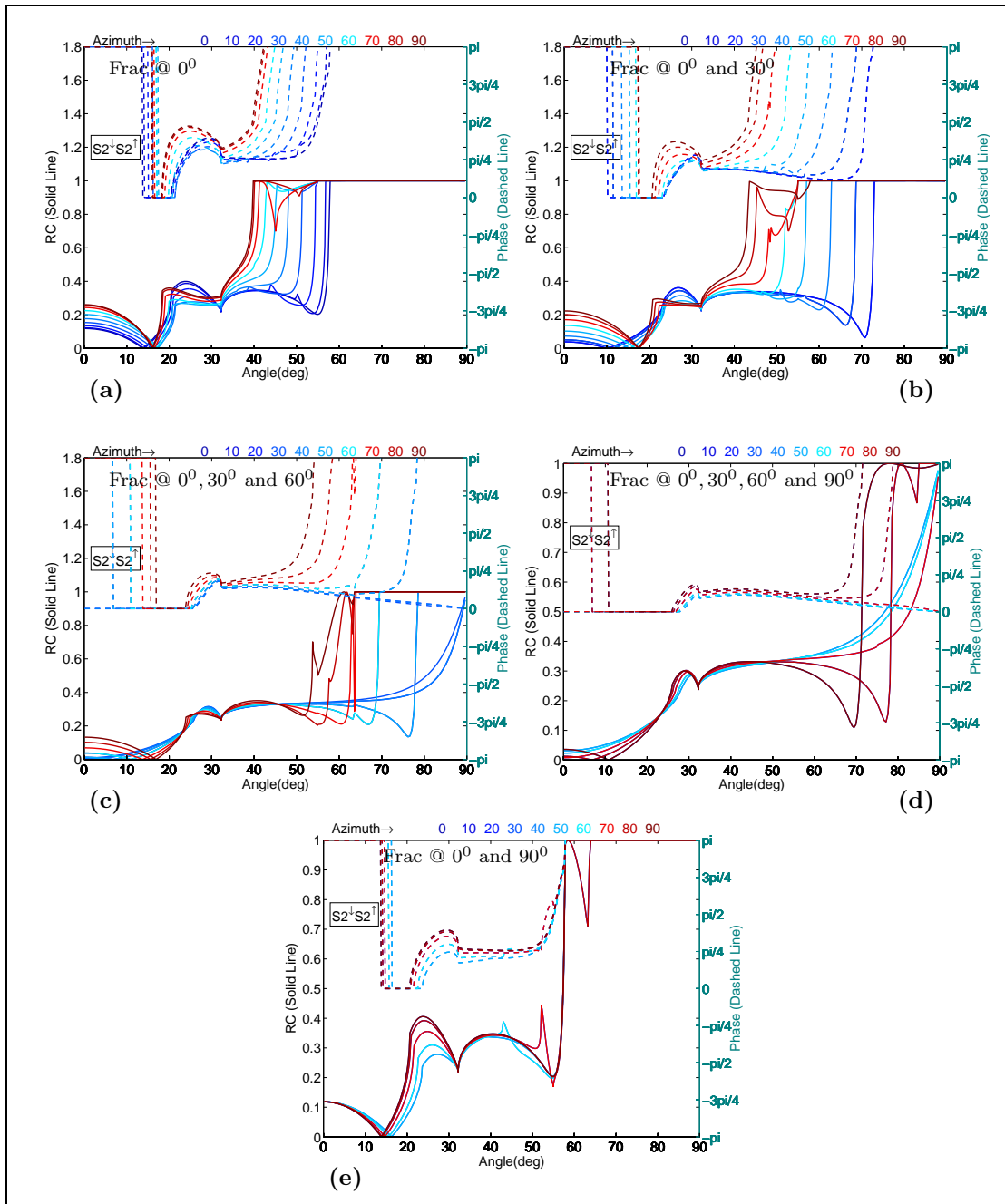
Figure D.6: S2S2 reflection coefficients and phase variation with angle and azimuth.

Appendix E

Bessel Series

$$e^{-ixcos\phi} = \sum_{m=-\infty}^{\infty} (-i)^m J_m(x) e^{-im\phi}$$

$$= J_0(x) + \sum_{m=1}^{\infty} (-i)^m J_m(x) e^{-im\phi} + \sum_{m=-1}^{-\infty} (-i)^m J_m(x) e^{-im\phi}$$

$$= J_0(x) + \sum_{m=1}^{\infty} (-i)^m J_m(x) e^{-im\phi} + \sum_{m=1}^{\infty} (-i)^{-m} J_{-m}(x) e^{im\phi}$$

$$= J_0(x) + \sum_{m=1}^{\infty} (-i)^m J_m(x) e^{-im\phi} + \sum_{m=1}^{\infty} (-i)^{-m}(-1)^{-m} J_m(x) e^{im\phi}$$

$$= J_0(x) + \sum_{m=1}^{\infty} (-i)^m J_m(x) e^{-im\phi} + \sum_{m=1}^{\infty} (i)^{-m} J_m(x) e^{im\phi}$$

$$= J_0(x) + \sum_{m=1}^{\infty} (-i)^m J_m(x) e^{-im\phi} + \sum_{m=1}^{\infty} (-i)^m J_m(x) e^{im\phi}$$

$$= J_0(x) + \sum_{m=1}^{\infty} (-i)^m J_m(x) \left[e^{-im\phi} + e^{im\phi} \right]$$

$$= J_0(x) + 2 \sum_{m=1}^{\infty} (-i)^m J_m(x) \cos(m\phi) \tag{E.1}$$